

# New Method for the Removal of Refraction Artifacts in Multibeam Echosounder Systems

by

Edouard Kammerer

Diplôme d'Études Approfondies en Géosciences Marines  
Université de Bretagne Occidentale, Brest, France, 1996

A Thesis Submitted in Partial Fulfilment of  
the Requirements for the Degree of

Doctor of Philosophy

in the Graduate Academic Unit of Geodesy and Geomatics Engineering

Supervisor:	J. E. Hughes Clarke, PhD, Geodesy & Geomatics Engineering
Examining Board:	B.G. Nickerson, Chair, PhD, Computer Science, D.E. Wells, PhD, Geodesy & Geomatics Engineering R.C. Courtney, PhD, Geological Survey of Canada
External Examiner:	L.C. Huff, PhD, Joint Hydrographic Center (NOAA-University of New Hampshire)

This Thesis is accepted.

-----  
Dean of Graduate Studies

THE UNIVERSITY OF NEW BRUNSWICK

June, 2000

© Edouard Kammerer, 2000

## **Abstract**

Refraction artifacts are often present in shallow water multibeam surveys and can degrade the quality of the final product if they are not adequately addressed. This thesis consists of the implementation of a systematic analysis and correction software package that addresses refraction artifacts in a post-processing context.

The methodology consists of the estimation of the variation in the water sound speed distribution, by using the information given by the multibeam dataset itself. This is done by the evaluation of the appropriately modeled Sound Speed Profiles (SSP), which is applied either in addition to an already existing SSP, or applied directly to the raw data. Refraction errors are most developed in the outer parts of the survey line coverage. The software developed takes advantage of this observation by utilising the nadir data because they are almost unaffected by refraction errors. Two methods of analysis are considered in this study. The first method uses two neighbouring parallel lines to generate corrections. The second uses the crossing check lines.

Both methods are used to evaluate the refraction coefficients of a two-layer SSP model, which, when applied, should bring the outer parts of the survey line as close as possible to the real seafloor (as observed at nadir).

The software developed is tested on an actual multibeam dataset. This data has been acquired off Saint John Harbor (NB) with a SIMRAD EM1000 sonar. The application of the new post-processing tool reduces refraction artifacts. The reduction of such artifacts improves

the extraction of useful information contained in the multibeam data. The method used allows as well the computation of correction SSPs that provide characteristics of an equivalent water mass.

## **Résumé**

Les artefacts de réfraction sont souvent présents dans les levés multifaisceaux en eaux peu profondes et peuvent dégrader la qualité du produit final si le problème n'est pas résolu de manière adéquate. Le projet présenté consiste à l'implémentation d'une analyse systématique et d'un logiciel de traitement qui réduit les artefacts de réfraction a posteriori.

La méthode consiste en l'estimation de la variation de la répartition de la vitesse du son dans l'eau en utilisant les informations fournies par les données multifaisceaux elles-mêmes. Ceci est réalisé par l'évaluation de modèles de profils de vitesse appropriés, qui seront ajoutés aux profils de vitesse déjà existant ou appliqués directement sur les données brutes. Les erreurs de réfraction se développent le plus sur les parties extérieures des fauchées. Le logiciel développé profite de cette observation en utilisant les données centrales qui ne sont presque pas touchées par les erreurs de réfraction. Deux méthodes d'analyse sont envisagées dans cette étude. La première méthode utilise les deux lignes parallèles voisines pour générer des corrections et la seconde méthode utilise les lignes orthogonales de vérification.

Les deux méthodes sont utilisées pour évaluer les coefficients de réfraction d'un modèle à deux couches de profils de vitesse qui devrait replacer les parties externes des fauchées aussi près que possible du fond sous-marin réel (comme observé en partie centrale de fauchée).

Le logiciel développé est testé sur un réel jeu de données multifaisceaux. Ces données ont été acquises au large du port de Saint John (NB) avec un SIMRAD EM1000. L'application de cet outil de traitement a posteriori réduit les artefacts de réfraction. La réduction de tels artefacts accroît l'information utile contenue dans les données multifaisceaux. La méthode utilisée permet également le calcul de corrections de profils de vitesse qui fournissent des caractéristiques d'une masse d'eau équivalente.

## **Acknowledgements**

I would like to express here my sincere appreciation to my supervisor Dr. John Hughes Clarke for his enthusiastic and helpful guidance and support for the realization of my thesis project. My gratitude is also going conjointly to Dr. Larry Mayer for his help and excellent advice.

Financial support for this thesis came from the University of New Brunswick and the Natural Science and Engineering Research Council of Canada.

Many thanks go to the students that I have met during these years, especially the graduate students of the department. They made this time very enjoyable by their friendship.

Je tiens à remercier du fond du cœur ma famille et amis en France qui, malgré l'éloignement, sont restés près de moi et m'ont aidé à soutenir mes efforts.

## Table of Contents

Abstract .....	iii
Résumé.....	iv
Acknowledgements .....	vi
Table of Contents .....	vii
List of Tables:.....	xi
List of Figures .....	xii
<b>CHAPTER 1 - INTRODUCTION.....</b>	<b>1</b>
<b>CHAPTER 2 - BACKGROUND.....</b>	<b>3</b>
2.1. NATURE OF A SOUND WAVE.....	3
2.1.1. <i>General description</i> .....	3
2.1.2. <i>Plane and spherical wave equations</i> .....	4
2.1.3. <i>Solution of the wave equations</i> .....	6
2.2. A SOUND WAVE IN THE OCEAN .....	6
2.2.1. <i>Structure of the ocean as a sound propagating medium</i> .....	7
2.2.2. <i>The sound speed equation</i> .....	8
2.2.3. <i>Refraction</i> .....	10
2.2.3.1. Vertical case: harmonic mean and nadir beam stability .....	11
2.2.3.2. Oblique incident wave crossing a sound speed boundary .....	12
2.2.3.3. Oblique incident wave crossing a linear sound speed gradient .....	15
2.2.3.4. Practical application of this theory to oblique propagation in the ocean .....	17
2.2.3.5. Vertical beams vs. oblique beams .....	18
2.3. DESCRIPTION OF MULTIBEAM ECHOSOUNDERS.....	20
2.3.1. <i>General description</i> .....	20
2.3.2. <i>Transducer</i> .....	21
2.3.2.1. Material.....	21
2.3.2.2. Configuration .....	21
2.3.2.3. Beamwidth.....	23
2.3.2.4. Element spacing .....	24
2.3.3. <i>Transceiver</i> .....	24
2.3.3.1. Transceiver function .....	24
2.3.3.2. Beamforming.....	25
2.3.3.3. Beam steering.....	26
2.3.4. <i>Bottom detection</i> .....	32
2.3.4.1. Extraction of the bottom detect window .....	33
2.3.4.2. Determination of the time of bore site strike .....	33
2.3.4.3. Amplitude detect methods.....	33
2.3.4.4. Phase detect methods.....	34
2.3.5. <i>Position and Orientation Integration</i> .....	35
2.3.5.1. Position .....	35
2.3.5.2. Orientation .....	37
2.4. CONCLUSION .....	39
<b>CHAPTER 3 - REFRACTION IN MULTIBEAM ECHOSOUNDING.....</b>	<b>40</b>

3.1. GENERAL.....	40
3.2. EFFECT THROUGH THE WATER COLUMN .....	41
3.3. EFFECT DURING THE BEAMFORMING .....	44
3.4. EXAMPLES OF ARRAY FACE REFRACTION EFFECT DURING BEAMFORMING .....	46
3.4.1. <i>Introduction</i> .....	46
3.4.2. <i>Curved Array Sonar</i> .....	47
3.4.2.1. Mode of operation .....	47
3.4.2.2. Refraction with a curved transducer .....	48
3.4.2.3. Refraction with a positive roll angle .....	50
3.4.2.4. Visualization of the refraction with a varying roll angle .....	51
3.4.3. <i>Flat Array Sonar (without roll stabilisation)</i> .....	53
3.4.3.1. Mode of operation .....	53
3.4.3.2. Refraction with a level transducer.....	55
3.4.3.3. Refraction with a positive roll angle .....	56
3.4.3.4. Visualization of the refraction with a varying roll angle .....	56
3.4.4. <i>Motion Stabilised Flat Array Sonar</i> .....	57
3.4.4.1. Mode of operation .....	58
3.4.4.2. Refraction with a level transducer.....	58
3.4.4.3. Refraction with a positive roll angle .....	59
3.4.4.4. Visualization of the refraction with a varying roll angle .....	60
3.4.5. <i>Dual Transducer Sonar</i> .....	61
3.4.5.1. Mode of operation .....	61
3.4.5.2. Refraction with a level dual transducer.....	62
3.4.5.3. Refraction with a positive roll angle .....	63
3.4.5.4. Visualization of the refraction with a varying roll angle .....	64
3.4.6. <i>Roll Stabilised Dual Transducer Sonar</i> .....	65
3.4.6.1. Mode of operation .....	65
3.4.6.2. Refraction with a level dual transducer.....	66
3.4.6.3. Refraction with a positive roll angle .....	66
3.4.6.4. Visualization of the refraction with a varying roll angle .....	67
3.5. CONCLUSION .....	68
<b>CHAPTER 4 REMOVAL OF THE SOUND SPEED REFRACTION ARTIFACT .....</b>	<b>70</b>
4.1. INTRODUCTION .....	70
4.2. ACQUISITION OF THE DATA WITH A VELOCIMETER .....	71
4.3. REDUCTION OF THE SOUNDINGS.....	72
4.3.1. <i>At the transducer array face</i> .....	72
4.3.2. <i>Within the water column</i> .....	72
4.3.2.1. Methodology .....	72
4.3.2.2. Use of SSPs in different situations .....	74
4.4. REDUCTION OF THE SOUNDINGS IN POST -PROCESSING.....	76
4.4.1. <i>Relative Area Difference Method</i> .....	76
4.4.2. <i>Equivalent Sound Speed Profile Method</i> .....	78
4.5. REFRACTION ARTIFACT REMOVAL METHODS.....	80
4.5.1. <i>OMG Refraction Tool</i> .....	80
4.5.2. <i>BatCor method</i> .....	82
4.5.3. <i>Method of the 45° beams</i> .....	84
4.6. CONCLUSION .....	86
<b>CHAPTER 5 - GENERAL OVERVIEW OF REF_CLEAN .....</b>	<b>87</b>



5.1. CASE OF THE SAGUENAY FJORD.....	87
5.2. OVERVIEW OF THE METHOD .....	89
5.2.1. <i>General</i> .....	89
5.2.2. <i>First approach: adjustment of the existing SSP</i> .....	90
5.2.3. <i>Second approach: reconstitution of a new SSP</i> .....	90
5.2.4. <i>Overview</i> .....	90
<b>CHAPTER 6 - PRELIMINARY STUDIES .....</b>	<b>93</b>
6.1. INVERSE THEORY.....	94
6.2. CHOICE OF A SYNTHETIC SSP.....	95
6.2.1. <i>Introduction</i> .....	95
6.2.2. <i>Methodology</i> .....	95
6.2.3. <i>Step SSP computation</i> .....	97
6.2.4. <i>Gradient SSP computation</i> .....	99
6.2.5. <i>Comparisons of the results and conclusion</i> .....	100
6.3. VARIABLE REDUCTION .....	105
6.3.1. <i>Introduction</i> .....	105
6.3.2. <i>Case of <math>c_0</math></i> .....	106
6.3.3. <i>Case of <math>z_s</math>, <math>c_1</math> and <math>c_2</math></i> .....	107
6.3.4. <i>Methodology</i> .....	108
6.3.5. <i>Conclusion</i> .....	113
6.4. VALIDITY OF THE ADDITION OF A SYNTHETIC ONE-LAYER SSP CORRECTION .....	113
6.4.1. <i>Introduction</i> .....	114
6.4.2. <i>Methodology</i> .....	114
6.4.3. <i>Results and Analysis</i> .....	115
6.5. CONCLUSIONS.....	119
<b>CHAPTER 7 - METHODOLOGY.....</b>	<b>121</b>
7.1. PRELIMINARY COMPUTATIONS: EXTRACTION_OMG.....	121
7.2. FIRST APPROACH: ADJUSTMENT OF THE EXISTING SSP .....	122
7.3. SECOND APPROACH: PRELIMINARY COMPUTATIONS.....	123
7.4. METHODOLOGY: CASE OF PARALLEL LINES .....	126
7.4.1. <i>Overview</i> .....	126
7.4.2. <i>First step: decomposition of the survey line in small datasets</i> .....	126
7.4.3. <i>Second step: adjustment of the average swath</i> .....	130
7.5. METHODOLOGY: CASE OF CROSSING CHECK-LINES.....	132
7.5.1. <i>Overview</i> .....	132
7.5.2. <i>First step: localization of the crossing point</i> .....	133
7.5.3. <i>Second step: selection of the data to compare</i> .....	134
7.5.3.1. <i>Selection of the data from the survey line</i> .....	134
7.5.3.2. <i>Selection from the check-line</i> .....	135
7.5.3.3. <i>Projection of the two selections on a common straight line</i> .....	137
7.5.4. <i>Third step: comparison of the two average profiles</i> .....	138
7.5.4.1. <i>Resampling of the survey line average profile</i> .....	138
7.5.4.2. <i>Computation of the trend of the crossing line profile</i> .....	139
7.5.4.3. <i>Computation of the refraction coefficients</i> .....	140
7.6. ROUGHNESS OF THE SEAFLOOR.....	141
7.6.1. <i>Across-track roughness</i> .....	142
7.6.2. <i>Along-track roughness</i> .....	144
7.6.3. <i>Weighting of the refraction coefficients</i> .....	145

7.7. OPTIMISATION OF REFRACTION COEFFICIENTS.....	147
7.7.1. <i>Parallel lines case</i> .....	148
7.7.2. <i>Crossing lines case</i> .....	149
7.8. FINAL COMPUTATIONS.....	153
7.9. EXTERNAL ERROR SOURCES.....	155
7.9.1. <i>Vertical Errors</i> .....	156
7.9.2. <i>Rotational Errors</i> .....	158
7.9.3. <i>Imperfect patch test results</i> .....	159
7.9.4. <i>Depth errors in the swath</i> .....	160
7.10. SOFTWARE DESCRIPTION.....	162
7.10.1. <i>General Description</i> .....	163
7.10.2. <i>Written Code</i> .....	163
7.10.3. <i>CPU time</i> .....	164
<b>CHAPTER 8 - RESULTS AND ANALYSIS .....</b>	<b>166</b>
8.1. PRESENTATION OF THE DATASET USED.....	166
8.2. OCEANOGRAPHIC CONSTRAINTS.....	168
8.3. APPLICATION OF THE METHOD.....	172
8.3.1. <i>Data format conversion</i> .....	173
8.3.2. <i>Parallel lines case</i> .....	173
8.3.3. <i>Crossing lines case</i> .....	174
8.3.4. <i>Computation of the Roughness</i> .....	176
8.3.5. <i>Refraction coefficients</i> .....	181
8.3.5.1. First approach: SSP correction.....	183
8.3.5.2. Second method: new SSP.....	185
8.3.5.3. Analysis of the distribution of the refraction coefficients.....	186
8.4. RESULTS.....	187
8.4.1. <i>DTM comparison</i> .....	187
8.4.2. <i>Profile comparisons</i> .....	195
8.5. ANALYSIS.....	202
8.5.1. <i>Cornering effects</i> .....	202
8.5.2. <i>Local roll artifacts</i> .....	204
8.5.3. <i>Correction of artificial errors</i> .....	205
8.6. QUANTITATIVE EVALUATION OF THE PERFORMANCE OF THE METHOD .....	207
8.6.1. <i>Parallel lines</i> .....	208
8.6.2. <i>Crossing lines</i> .....	211
8.7. RECOMMENDATIONS FOR FUTURE SURVEYS.....	214
8.7.1. <i>Parallel lines</i> .....	214
8.7.2. <i>Density of check-lines</i> .....	214
8.7.3. <i>Line spacing and data overlap</i> .....	215
8.7.4. <i>SSP distribution</i> .....	215
<b>CHAPTER 9 - CONCLUSION.....</b>	<b>217</b>
References and Bibliography .....	219
Vita.....	1

## List of Tables:

TABLE 1: STANDARD DEVIATIONS OF THE FOUR HISTOGRAMS PLOTTED ON FIGURE 83 ABOVE. THE HISTOGRAM OF THE HEAVE MEASURED ON JUNE 7 HAS A MUCH LARGER STANDARD DEVIATION THAN THE HISTOGRAMS OF THE THREE OTHER DAYS.....	179
TABLE 2: EXAMPLE OF A REFRACTION COEFFICIENT FILE FOR A SURVEY LINE. EACH ROW OF THIS TABLE DEFINES A SYNTHETIC TWO-LAYER SSP CORRECTION, WHICH WILL BE APPLIED TO THE DATA AT THE LOCATION OF THE PING NUMBER.....	183
TABLE 3: LIST OF MEANS AND STANDARD DEVIATIONS OF THE DIFFERENCE DTMS IN THE CASE OF PARALLEL LINES.....	210
TABLE 4: LIST OF MEANS AND STANDARD DEVIATIONS OF THE DIFFERENCE DTMS IN THE CASE OF PARALLEL LINES.....	213

## List of Figures

FIGURE 1: THE COMPLEXITY OF THE OCEANOGRAPHY OF COASTAL WATERMASSES. MANY EXTERNAL FORCE MECHANISMS INFLUENCE THE VELOCITY STRUCTURE [HUGHES CLARKE, 1999A].	8
FIGURE 2: SOUND SPEED DISCONTINUITY CROSSED BY AN INCIDENT PLANE WAVE [BURDIC, 1991].	12
FIGURE 3: CIRCULAR TRAJECTORY OF A SOUND WAVE IN A SOUND SPEED GRADIENT [BURDIC, 1991].	17
FIGURE 4: TWO APPROXIMATIONS OF A REAL SOUND SPEED PROFILE ON THE LEFT. THE GRADIENT SSP IN THE MIDDLE IS COMPOSED OF SIMPLE LINEARLY VARYING STEPS. THE STEP SSP ON THE RIGHT IS COMPOSED OF CONSTANT STEPS.	18
FIGURE 5: COMPARISON BETWEEN DEPTH ERRORS GENERATED VERTICALLY AT DIFFERENT ANGLES FROM VERTICAL AND AT A DEPTH OF 100M. THE WATER COLUMN WAS INITIALLY UNIFORM WITH A SOUND SPEED OF 1500M/S. THEN 10M/S HAVE BEEN ADDED TO THE SPEED IN THE FIRST 10 METRES.	19
FIGURE 6: NARROW BEAM CREATED BY A MILL'S CROSS TRANSDUCER OF A MULTIBEAM SONAR, IT IS THE RESULT OF THE PRODUCT OF THE BEAM PATTERNS OF THE TRANSMIT ARRAY AND THE RECEIVE ARRAY [HUGHES CLARKE, 1999A].	22
FIGURE 7: A VIRTUAL ARRAY CREATED BY PHASE DELAY ADDED TO EACH OF THE TRANSDUCER ELEMENT	27
FIGURE 8: FFT BEAMFORMING: THE ANGLE OF INCIDENCE $q$ IS DETERMINED BY THE FREQUENCY OF THE SIGNAL COMING FROM THE HYDROPHONES.	30
FIGURE 9: GRAPH SHOWING THE MATRIX (TIME, ANGLE-FREQUENCY AND AMPLITUDE). THE BEAM ANGLE IS COMPUTED FROM RUNNING A FFT ON THE INSTANTANEOUS SPATIAL SIGNAL ACROSS THE ARRAY.	31
FIGURE 10: BEAMSTEERING COMPENSATION OF THE ATTITUDE OF THE VESSEL. A1, B1 AND C1 SHOW THE EFFECT OF THE DIFFERENT ROTATIONS ON THE SWATH. A2, B2 AND C2 SHOW HOW THIS EFFECT IS CORRECTED: A2 AND B2 BY BEAM STEERING AND C2 BY MULTISECTOR STABILISATION.	39
FIGURE 11: THIS SKETCH SHOWS THE PROPAGATION OF THE SOUND RAY THROUGH THE WATER COLUMN. IF THE SOUND SPEED IS NOT PERFECTLY MONITORED, IT INDUCES BEAM ANGLE ERRORS AT THE FACE OF THE TRANSDUCER AND WITH EACH SOUND SPEED ERROR IN THE WATER COLUMN, DEVIATES THE RAY FROM THE CORRECT PATH.	41
FIGURE 12: EFFECT OF A STEP AND A GRADIENT SSP ON THE PATH OF A SINGLE BEAM.	42
FIGURE 13: 100 M. DEEP SYNTHETIC FLAT SEAFLOOR DEFORMED BY A STEP SOUND SPEED PROFILE.	43
FIGURE 14: VARIATION OF THE MAGNITUDE OF THE ANGLE ERROR WITH RESPECT TO THE BEAM-POINTING ANGLE FOR DIFFERENT SOUND SPEED DIFFERENCES.	45
FIGURE 15: BEAMFORMING IN A CURVED ARRAY TRANSDUCER CONFIGURATION. STEERING IS PERFORMED ONLY BEYOND A CERTAIN ANGLE.	48
FIGURE 16: IMPACT OF A SURFACE SOUND SPEED DISCONTINUITY ON THE SHAPE OF THE SWATH OF A HORIZONTAL CURVED ARRAY. NOTE THAT THE ERRORS INDUCED APPEAR ONLY BEYOND THE ANGLE AFTER WHICH BEAM STEERING IS PERFORMED. EQUIANGULAR BEAM SPACING ON THE LEFT AND EQUIDISTANT BEAM SPACING ON THE RIGHT.	49
FIGURE 17: IMPACT OF A SURFACE SOUND SPEED DISCONTINUITY ON THE SHAPE OF THE SWATH OF A TILTED (15° ROLL) CURVED ARRAY. NOTE THAT THE ERRORS INDUCED APPEAR ONLY ON ONE SIDE OF THE SWATH.	50
FIGURE 18: SHAPE OF THIRTY SUCCESSIVE SWATHS WHEN THE CURVED ARRAY IS ROLLING FROM +15° TO -15°. NOTE THAT THE ERRORS INDUCED ARE MOVING PROPORTIONALLY WITH THE ROLL ANGLE.	52

FIGURE 19: BEAM SPACING OF AN FFT BEAMFORMER (TOP GRAPH) COMPARED TO EQUIANGULAR BEAM SPACING (BOTTOM GRAPH).....	54
FIGURE 20: BEAMFORMING IN A LINE ARRAY TRANSDUCER CONFIGURATION. BEAM STEERING IS PERFORMED ALL OVER THE TRANSDUCER EXCEPT AT NADIR.....	54
FIGURE 21: IMPACT OF A SURFACE SOUND SPEED DISCONTINUITY ON THE SHAPE OF THE SWATH OF A LEVEL LINE ARRAY. NOTE THAT THE ERRORS INDUCED APPEAR ALL OVER THE SWATH EXCEPT AT NADIR.....	55
FIGURE 22: IMPACT OF A SURFACE SOUND SPEED DISCONTINUITY ON THE SHAPE OF THE SWATH OF A TILTED (15°-ROLL) NON ROLL-STABILISED LINE ARRAY.....	56
FIGURE 23: SHAPE OF THIRTY SUCCESSIVE SWATHS WHEN THE LINE ARRAY IS ROLLING FROM +15° TO -15°. IN THE RIGHT SKETCH THE OUTERMOST BEAMS HAVE BEEN TRIMMED OUT.....	57
FIGURE 24: IMPACT OF A SURFACE SOUND SPEED DISCONTINUITY ON THE SHAPE OF THE SWATH OF A LEVEL LINE ARRAY. NOTE THAT THE ERRORS INDUCED APPEAR ALL OVER THE SWATH EXCEPT AT NADIR. THE BEAM SPACING IS EQUIANGULAR ON THE LEFT FIGURE AND EQUIDISTANT ON THE RIGHT FIGURE.....	59
FIGURE 25: IMPACT OF A SURFACE SOUND SPEED DISCONTINUITY ON THE SHAPE OF THE SWATH OF A TILTED (15°-ROLL) ROLL-STABILISED LINE ARRAY. THE BEAM SPACING IS EQUIANGULAR ON THE LEFT FIGURE AND EQUIDISTANT ON THE RIGHT FIGURE.....	60
FIGURE 26: SHAPE OF THIRTY SUCCESSIVE SWATHS WHEN THE LINE ARRAY IS ROLLING FROM +15° TO -15°.....	61
FIGURE 27: TRANSDUCER CONFIGURATION WITH A DUAL LINE ARRAY. THE TWO MILLS CROSSES MAKE AN ANGLE OF 90° WITH RESPECT TO EACH OTHER.....	62
FIGURE 28: IMPACT OF A SURFACE SOUND SPEED DISCONTINUITY ON THE SHAPE OF THE SWATH OF A HORIZONTAL DUAL LINE ARRAY. NOTE THAT THE ERRORS INDUCED APPEAR ALL OVER THE SWATH.....	63
FIGURE 29: IMPACT OF A SURFACE SOUND SPEED DISCONTINUITY ON THE SHAPE OF THE SWATH OF A TILTED (15°-ROLL) NON ROLL-CORRECTED DUAL LINE ARRAY TRANSDUCER.....	64
FIGURE 30: SHAPE OF THIRTY SUCCESSIVE SWATHS WHEN THE LINE ARRAY IS ROLLING FROM +15° TO -15°. ON THE LEFT SKETCH THE OUTER BEAMS HAVE BEEN TRIMMED OUT.....	65
FIGURE 31: IMPACT OF A SURFACE SOUND SPEED DISCONTINUITY ON THE SHAPE OF THE SWATH OF A TILTED (15°-ROLL) ROLL-STABILISED DUAL LINE ARRAY TRANSDUCER (EQUIANGULAR BEAM SPACING CASE).....	67
FIGURE 32: SHAPE OF THIRTY SUCCESSIVE SWATHS WHEN THE LINE ARRAYS ROLL FROM +15° TO -15°. THE SYSTEM IS ROLL-STABILISED, NOTICE THE STRAIGHT TRACK.....	68
FIGURE 33: DEFINITION OF $\Delta S$ DIFFERENCE OF TWO SOUND SPEED PROFILES [GENG, 1998].....	77
FIGURE 34: SEARCH FOR AN EQUIVALENT LINEAR SOUND SPEED PROFILE.....	78
FIGURE 35: OMG REFRACTION TOOL MAIN WINDOW.....	81
FIGURE 36: METHODOLOGY USED BY THE SOFTWARE PACKAGE BATCOR [DIJKSTRA, 1999].....	83
FIGURE 37: SCHEMA OF AN INTERSECTION AREA SHOWING THE TRACKS OF THE $\pm 45^\circ$ BEAM AND THE NADIR BEAM.....	85
FIGURE 38: DIFFERENCE OF THE TWO DTMS. THE STRIPES PARALLEL TO THE SHIP TRACKS ARE ARTIFACTS, RESULTS OF THE APPLICATION OF AN INCORRECT SSP. RIGHT: REFRACTION NOT PROCESSED; LEFT: REFRACTION PROCESSED, THE ARTIFACTS ARE REDUCED BUT ARE STILL TOO HIGH. [KAMMERER ET AL., 1998].....	88
FIGURE 39: FLOWCHART SHOWING THE TWO PROCESSING METHODS PROPOSED. THE FIRST APPROACH IS DESCRIBED WITH THE PLAIN ARROWS AND THE SECOND APPROACH WITH THE DASHED ARROWS.....	91
FIGURE 40: TWO EQUIVALENT SYNTHETIC SSPS AND THEIR EFFECT ON THE PROPAGATION OF A SINGLE BEAM. ON THE RIGHT THE SSP HAS A STEP FUNCTION AT $Z_s$ , ON THE LEFT A GRADIENT	

FUNCTION. THE ANGLES AFTER THE TWO SPEED CHANGES ARE THE SAME. THE TWO SSPS BRING THE BEAM ALONG THE SAME PATH.....	96
FIGURE 41: EFFECT OF A STEP SSP ON A SINGLE RAY, DEVIATION OF THIS RAY FROM ITS ORIGINAL HEADING ( $C_1 > C_2$ ). .....	97
FIGURE 42: RAY PATH THROUGH A WATER COLUMN HAVING A GRADIENT IN THE VARIATION OF THE SOUND SPEED VERSUS DEPTH. ....	99
FIGURE 43: CLOSE-UP ON THE AREA WHERE THE RAY CHANGES DIRECTION. IT FOLLOWS A CURVE AB IN THE CASE OF A GRADIENT SSP AND FOLLOWS THE PATH ACB IN THE CASE OF A STEP SSP.....	101
FIGURE 44: VARIATION OF VERTICAL RANGE DIFFERENCE BETWEEN A STEP SSP AND A GRADIENT SSP FOR DIFFERENT VALUES OF GRADIENT. THE AMPLITUDE OF THESE DIFFERENCES IS $10^{-4}$ FOR A TOTAL DEPTH OF 100 M. ....	103
FIGURE 45: VARIATIONS OF OBLIQUE RANGE DIFFERENCES BETWEEN A STEP SSP AND A GRADIENT SSP FOR DIFFERENT PROPAGATION ANGLES ( $10^\circ$ , $30^\circ$ AND $50^\circ$ ) FOR DIFFERENT VALUES OF .....	105
FIGURE 46: EXAMPLE OF A SSP WITH TWO LAYERS. IT IS FULLY DESCRIBED BY THE FOUR VARIABLES $C_0$ , $C_1$ , $C_2$ , AND $Z_s$ . ....	106
FIGURE 47: THESE TWO SIMPLE GRAPHS SHOW HOW TWO COUPLES ( $C_1$ , $C_2$ ), ( $C_1'$ , $C_2'$ ) FOR A FIXED DEPTH $Z_s$ (ON THE LEFT) AND TWO COUPLES ( $Z_s$ , $C_2$ ), ( $Z_s'$ , $C_2'$ ) FOR A FIXED SPEED $C_1$ (ON THE .....	108
FIGURE 48: ABSOLUTE DIFFERENCE BY BEAM NUMBER BETWEEN THE SWATH RESULTING FROM THE APPLICATION OF A TWO-LAYER SSP ON A FLAT SEAFLOOR AND ITS BEST -FITTING PARABOLA FOR $C_1=1500$ M/S; $C_2=1505$ M/S; $Z_s=10$ M AND $C_1'=1510$ M/S; $C_2'=C_2$ ; $Z_s'=Z_s$ . ....	110
FIGURE 49: VARIATION OF THE TRAVELED DISTANCE AT NADIR FOR THE DIFFERENT CASES. CASE 0: APPLIANCE OF THE DATASET ( $C_1$ , $C_2$ AND $Z_s$ ) ONTO THE FLAT SEAFLOOR. CASE 1: ESTIMATION OF $C_2'$ FOR $Z_s$ CONSTANT AND THE NEW VALUE $C_1'$ . CASE 2: ESTIMATION OF $C_2''$ FOR $C_1$ CONSTANT AND THE NEW VALUE $Z_s'$ . ....	111
FIGURE 50: VERTICAL ADJUSTMENT OF THE TWO DEFORMED SWATHS AT NADIR (ON THE LEFT). ONCE ADJUSTED (ON THE RIGHT) THE TWO SWATHS MATCH PERFECTLY. ....	112
FIGURE 51: THIS SCHEMA COMPARES THE SUCCESSIVE APPLICATIONS OF A REAL SSP AND OF A SYNTHETIC ONE LAYER SSP TO THE APPLICATION OF THE SUM OF THESE TWO SSPS ON A 100 METRES DEEP SYNTHETIC FLAT SEAFLOOR. ....	117
FIGURE 52: ABSOLUTE VALUE OF THE DIFFERENCES BETWEEN THE GRAPHS RESULTING FROM THE TWO METHODS USED ABOVE. THE FILLED CIRCLES CORRESPOND TO THE DIFFERENCE IN DEPTH, THE EMPTY CIRCLES CORRESPOND TO THE ACROSS TRACK DIFFERENCE. ....	117
FIGURE 53: DIFFERENCES FOR THE 60 BEAMS IN DEPTH (ON THE LEFT) AND ACROSS TRACK (ON THE RIGHT) VALUES OF THE GRAPHS COMING FROM THE TWO METHODS COMPARED IN §6.4.2 FOR SEVEN REAL SSPs. ....	118
FIGURE 54: SCHEMA OF THE PROJECTION OF THE NAVIGATION DATA POINTS FROM THE THREE PARALLEL LINES ONTO A REFERENCE LINE ORIENTED ALONG THE AVERAGE OF THE THREE HEADINGS OF THE SURVEY LINES. ....	127
FIGURE 55: THE FIGURE ON THE LEFT IS THE GLOBAL VIEW OF THE THREE SURVEY LINES, THE COMMON SEGMENT AND ITS PARTITION IN SEGMENTS. THE RIGHT FIGURE IS A CLOSE-UP VIEW ON ONE OF THESE SUB SEGMENTS .....	129
FIGURE 56: RELATIVE POSITION OF THE DIFFERENT LINES IN A CROSS SECTION OF EACH SEGMENT. FIRST METHOD ABOVE: THE SWATH IS ADJUSTED TO THE NADIR DEPTH OF LINE #2. ....	131
FIGURE 57: SCHEMA OF AN INTERSECTION BETWEEN TWO SURVEY LINES. ....	134
FIGURE 58: SELECTION OF 200 PROFILES FROM THE SURVEY LINE ON BOTH SIDES OF THE INTERSECTION POINT WITH A CHECK-LINE. ....	135
FIGURE 59: SELECTION OF THE 10 BEAMS AROUND THE NADIR OF THE CHECK-LINE. ....	136
FIGURE 60: LEFT: VIEW OF THE TWO SELECTIONS MADE FROM THE TWO CROSSING LINES. RIGHT: AVERAGE PROFILES OF THE 200 SWATHS OF THE SURVEY LINE AND THE 10 CENTRAL BEAMS OF THE CHECK-LINE. ....	137

FIGURE 61: THE TWO AVERAGE PROFILES HAVE BEEN PROJECTED ON THE STRAIGHT LINE DEFINED BY THE AVERAGE HEADING OF THE CHECK-LINE AND PASSING BY THE INTERSECTION POINT .....	138
FIGURE 62: SUPERPOSITION OF THE PROFILE FROM THE SURVEY LINE (THE CURVED PROFILE) WITH THE GRIDDED PROFILE FROM THE CROSSING LINE. ....	139
FIGURE 63: COMPARISON BETWEEN THE TREND OF THE CROSSING LINE PROFILE AND THE SURVEY LINE AVERAGE SWATH. ....	140
FIGURE 64: PLOT OF THE SURVEY LINE AVERAGE SWATH DEFORMED BY THE TWO-LAYER SSP, WHICH BRINGS IT AS CLOSE AS POSSIBLE TO THE TREND OF THE CROSSING LINE.....	141
FIGURE 65: AVERAGE PROFILE OF A SEGMENT OF A SURVEY LINE WITH THE BEST FITTING PARABOLA FROM WHICH THE ROUGHNESS VALUE IS COMPUTED.....	143
FIGURE 66: PART OF THE DEPTH PROFILE OF A SURVEY LINE WITH THE BEST FITTING STRAIGHT LINES FOR EACH OF THE SEGMENTS FROM WHICH IS COMPUTED THE ROUGHNESS VALUE. ....	145
FIGURE 67: GRAPH SHOWING THE RELATION BETWEEN THE ROUGHNESS AND THE WEIGHTING TO BE APPLIED TO THE REFRACTION COEFFICIENT CORRECTION. THE HIGHER THE ROUGHNESS THE LOWER THE WEIGHT AND THEREFORE THE MORE THE CORRECTION IS REDUCED. NO ROUGHNESS IMPLIES NO WEIGHTING AND THUS FULL UNATTENUATED COEFFICIENTS .....	147
FIGURE 68: DIAGRAM SHOWING THE FIBONACCI SEARCH ALGORITHM. ....	149
FIGURE 69: DIAGRAM SHOWING HOW THE FIBONACCI ALGORITHM WORKS IN ORDER TO FIND THE MINIMUM OF A FUNCTION. ....	150
FIGURE 70: FLOWCHART DESCRIBING THE ITERATIVE METHOD USED TO MINIMISE $F(C_0, C_2)$ .....	152
FIGURE 71: GRAPH ILLUSTRATING THE ITERATIVE METHODOLOGY USED TO MINIMISE OF $F(C_0, C_2)$ .....	153
FIGURE 72: FLOWCHART OF THE REF_CLEAN METHOD. THE DASHED PATH IS THE APPROACH USING THE TRANSIT TIME AND BEAM ANGLE.....	155
FIGURE 73: EFFECT OF THE APPLICATION OF THE PROPOSED METHOD ONTO A LINE AFFECTED BY A VERTICAL OFFSET IN THE CONTEXT OF CROSSING LINES. THE METHOD SMOOTHS THE STEP BUT DOES NOT REMOVE IT.....	158
FIGURE 74: EFFECT OF THE APPLICATION OF THE PROPOSED METHOD ONTO A LINE AFFECTED BY A ROLL OFFSET. THE METHOD IS INEFFICIENT TO PERFORM CORRECTLY IN THIS CASE.....	159
FIGURE 75: LOCATION OF THE DATASET USED.....	167
FIGURE 76: MULTIBEAM SURVEY OFF SAINT JOHN (NB) HARBOUR (CHS - SIMRAD EM1000 - JUNE 1994). THIS PICTURE SHOWS THE DATA WITHOUT ANY REFRACTION POST-PROCESSING. NOTE THE REFRACTION ARTIFACT (STRIPES PARALLEL TO THE SURVEY LINES).....	168
FIGURE 77: LOCATION OF THE ACTUAL SSPS IN THE SURVEY AREA AND THE LINES ON WHICH THEY HAVE BEEN APPLIED.....	169
FIGURE 78: SHAPE OF THE SIX SSPS AND THEIR POSITION IN THE GRAPH OF THE TIDE VARIATIONS DURING THE SURVEY TIME .....	172
FIGURE 79: NAVIGATION OF SAINT JOHN DATASET. THE BLACK DOTS ARE THE CENTRE OF SEGMENTS OF THE SURVEY LINES WHERE THE ESTIMATION OF REFRACTION COEFFICIENTS IS CONDUCTED.....	174
FIGURE 80: NAVIGATION OF SAINT JOHN DATASET. THE BLACK DOTS ARE THE INTERSECTIONS BETWEEN PARALLEL SURVEY LINES AND CROSSING CHECK-LINES, REFRACTION COEFFICIENTS ARE ESTIMATED AT EACH OF THESE LOCATIONS. ....	175
FIGURE 81: 3D GRAPH OF THE GRIDDED GEOGRAPHIC DISTRIBUTION OF THE ACROSS-TRACK ROUGHNESS FOR EACH SEGMENT OF THE SURVEY LINES.....	177
FIGURE 82: 3D GRAPH OF THE GRIDDED GEOGRAPHIC DISTRIBUTION OF THE ALONG-TRACK ROUGHNESS FOR EACH SEGMENT OF THE SURVEY LINES.....	178
FIGURE 83: HISTOGRAMS OF THE HEAVE MEASUREMENTS FOR EACH OF THE FOUR DAYS OF THE SURVEY. NOTE THAT THE HISTOGRAM FOR JUNE 7 IS MORE SPREAD OUT THAN THE THREE OTHER DAYS. ....	179

FIGURE 84: HEAVE RESIDUALS BETWEEN JUNE 7 AND JUNE 8. THE UPPER PART OF THE IMAGE CORRESPONDS TO THE DATA COLLECTED ON JUNE 7 AND THE LOWER PART TO THE DATA FROM JUNE 8. THE HEAVE RESIDUALS ARE STRONGER ON THE PROFILE #1 THAN ON THE PROFILE #2.	180
FIGURE 85: HISTOGRAM OF THE ROUGHNESS COEFFICIENTS IN THE SAINT JOHN DATASET .....	181
FIGURE 86: CASE OF A PARALLEL LINE BROKEN IN TWO SURVEY LINES. ....	182
FIGURE 87: DISTRIBUTION OF THE SURFACE SOUND SPEED $C_0$ , CORRECTIONS TO THE ACTUAL SSPs. ....	184
FIGURE 88: DISTRIBUTION OF THE SOUND SPEED $C_2$ OF THE SECOND LAYER, CORRECTIONS TO THE ACTUAL SSPs. ....	184
FIGURE 89: GEO-DISTRIBUTION OF THE SURFACE SOUND SPEED $C_0$ , EQUIVALENT SSP. ....	185
FIGURE 90: GEO-DISTRIBUTION OF THE SOUND SPEED $C_2$ OF THE SECOND LAYER, EQUIVALENT SSP. ...	185
FIGURE 91: RESULTS FOR THE WESTERN PART OF THE SURVEY AREA. TOP IMAGE: INITIAL DATA WITH THE ACTUAL SSPs TAKEN DURING THE SURVEY. BOTTOM LEFT: RESULTS OF THE FIRST APPROACH (CORRECTED SSPs) BOTTOM RIGHT: RESULTS OF THE SECOND APPROACH (NEW SSPs). ....	189
FIGURE 92: RESULTS FOR THE CENTRAL PART OF THE SURVEY AREA. TOP IMAGE: INITIAL DATA WITH THE ACTUAL SSPs TAKEN DURING THE SURVEY. BOTTOM LEFT: RESULTS OF THE FIRST APPROACH (CORRECTED SSPs) BOTTOM RIGHT: RESULTS OF THE SECOND APPROACH (NEW SSPs). ....	191
FIGURE 93: RESULTS FOR THE EASTERN PART OF THE SURVEY AREA. TOP IMAGE: INITIAL DATA WITH THE ACTUAL SSPs TAKEN DURING THE SURVEY. BOTTOM LEFT: RESULTS OF THE FIRST APPROACH (CORRECTED SSPs) BOTTOM RIGHT: RESULTS OF THE SECOND APPROACH (NEW SSPs). ....	193
FIGURE 94: PROFILE A (SHALLOWEST AREA SEE ITS LOCATION IN THE MAP AT THE TOP OF THE PAGE). THE THREE PROFILES BELOW SHOW HOW THE REF_CLEAN TOOL CHANGES THE SHAPE OF THE SWATHS WITH THE TWO APPROACHES CONSIDERED. ....	196
FIGURE 95: PROFILE B (INTERMEDIATE AREA, SEE ITS LOCATION IN THE MAP AT THE TOP OF THE PAGE). THE THREE PROFILES BELOW SHOW HOW THE REF_CLEAN TOOL CHANGES THE SHAPE OF THE SWATHS WITH THE TWO APPROACHES CONSIDERED. ....	198
FIGURE 96: PROFILE C (DEEPEST AREA, SEE ITS LOCATION IN THE MAP AT THE TOP OF THE PAGE). THE THREE PROFILES BELOW SHOWS HOW THE REF_CLEAN TOOL CHANGES THE SHAPE OF THE SWATHS WITH THE TWO APPROACHES CONSIDERED. ....	200
FIGURE 97: ROLL AND HEAVE BIASES OCCURRING AT THE EXTREMITIES OF THE SURVEY LINES. TWO PROFILES TAKEN ON EACH SIDES OF THE SURVEYED AREA SHOW THESE ARTIFACTS. ....	203
FIGURE 98: GRAPH OF THE HEAVE VERSUS TIME AT THE BEGINNING ( $T=0$ ) OF TWO SURVEY LINES. THERE IS A POSITIVE BIAS FOLLOWED BY A NEGATIVE BIAS BEFORE A STABILISATION AROUND A ZERO MEAN. ....	204
FIGURE 99: ROLL BIAS IN A SURVEY LINE. THE VESSEL SLIDES AWAY FROM A STRAIGHT NAVIGATION.	205
FIGURE 100: SUN-ILLUMINATION OF THE ORIGINAL DTM (FIGURE 76) ON WHICH AN ADDITIONAL SOUND SPEED DISCONTINUITY OF 10M/S AT 5M HAS BEEN ADDED. ....	206
FIGURE 101: SUN-ILLUMINATION OF THE DTM GENERATED WITH THE REFRACTION COEFFICIENTS OUTPUT FROM THE APPLICATION OF REF_CLEAN ON THE DTM ON FIGURE 100 ABOVE. ....	206
FIGURE 102: HISTOGRAMS OF THE COEFFICIENT $C_2$ GENERATED BY THE APPLICATION OF REF_CLEAN ON THE ORIGINAL DATASET (IN BLACK) AND ON THE DATASET DEGRADED WITH A 10 M/S ADDITIONAL DISCONTINUITY (IN GRAY). ....	207
FIGURE 103: ILLUSTRATION OF THE METHODOLOGY TO QUANTIFY HOW WELL THE PARALLEL LINES FIT WITH THEIR NEIGHBOURS. THE LINES ARE GRIDDED EVERY SECOND PARALLEL LINES AND THE TWO DTMS OBTAINED SUBTRACTED FROM EACH OTHER. ....	209
FIGURE 104: NORMALIZED HISTOGRAMS OF THE DIFFERENCE DTMS COMPUTED TO QUANTIFY THE PERFORMANCE OF THE METHOD IN THE PARALLEL LINE CASE. ....	210
FIGURE 105: ILLUSTRATION OF THE METHODOLOGY TO QUANTIFY HOW WELL THE CROSSING LINES FIT WITH THE OTHER SURVEY LINES. THE DTM CONTAINING THE NADIR OF THE CROSS-LINES IS SUBTRACTED TO THE ORIGINAL DATA AND THE PROCESSED DATA. ....	212



FIGURE 106: NORMALIZED HISTOGRAMS OF THE DIFFERENCE DTMS COMPUTED TO QUANTIFY THE PERFORMANCE OF THE METHOD IN THE PARALLEL LINE CASE.....	213
---	-----

## **CHAPTER 1 - INTRODUCTION**

Hydrographic surveying uses sound as a remote sensing tool. One of the most advanced and effective hydrographic instruments is the multibeam sonar. These systems use sound to measure the depth in the ocean. The fundamental data received back by these sonars are, the two way travel time of the signal between the transducer and the seafloor and the direction from which the echo is reflected. The usefulness of the recovered data depends critically on the knowledge one has about the medium that the signal propagates through. The wide variety of highly variable physical characteristics of the ocean makes this task a challenge. Among these characteristics, the variation of temperature, pressure and salinity affects the speed and the direction of sound travelling through the water mass. These effects are called refraction. The goal of our research work is to design a new post-processing tool able to correct the soundings from the errors induced by refraction.

The purpose of this thesis is to propose a new technique to improve the data quality in regard to refraction artifacts in multibeam sonar surveys. Specifically, we describe the basic physics of sound propagation, the characteristics of its propagation in seawater, the way a multibeam sonar operates to transmit and receive sound waves, how refraction affects echo sounding and what is usually done to reduce the degradation of the sounding caused by

refraction. The final part of the thesis is devoted to the methodology, application and results of the new refraction tool developed.

The contributions to knowledge made in this work can be listed as follows:

A detailed study of the shape of refraction artifacts generated by a wrong monitoring of the sound speed at the face of the transducer is presented. Different examples of sonar configurations are considered. The dependence of these artifacts with a varying-roll is also investigated (Chapter 3).

The reader will find a review of the methods used to reduce the multibeam soundings with the water sound speed in real-time and in post-processing and of existing methods to correct refraction artifacts (Chapter 4).

The elaboration of a simple Sound Speed Profile correction model is presented. It shows how an actual SSP can be approximated by a two-layer SSP with a step function rather than a gradient function as a thermocline/halocline. The relation between the variables of the SSP model and the shape of the artifact is analyzed (Chapter 6).

The methodology (Chapter 5, Chapter 7) and the application (Chapter 8) of a new refraction processing tool are proposed to the reader. This tool allows fully automated adjustments of the refraction artifacts present in multibeam datasets. These adjustments are based on the assumption that the nadir depths of the survey lines are adequate to be used as references for the computation of corrections.

## **CHAPTER 2 - BACKGROUND**

Before introducing the new technique for the removal of refraction artifacts, we briefly review the theory of sound propagation in seawater. The phenomena that disturb sound propagation are investigated. They are the causes of the errors that we want to minimise. The mode of operation of multibeam sonar is then described before making a detailed examination of how the sound propagation disturbances appear in the multibeam measurements.

### **2.1. NATURE OF A SOUND WAVE**

#### *2.1.1. General description*

Sound is a phenomena created by a mechanical pressure disturbance in a medium. This disturbance propagates itself depending on the mechanical properties (inertial and elastic characteristics) of the medium. The propagation lasts as long as other forces have not progressively balanced out the pressure disturbance. The actual material that constitutes the

medium vibrates as the wave propagates through it. The sound energy is transmitted from one place to another by this phenomenon.

Sound waves propagate as spherical wave fronts, however as the waves become very distant from the source they can be approximated by a plane wave. This approximation allows us to easily describe the acoustical properties of the medium.

### *2.1.2. Plane and spherical wave equations*

Considering the variation in volume, strain and particle velocity of a small volume of the medium, during a short time interval, the differential acoustic plane wave equation is established as:

$$Eq. 1 \quad \frac{\partial^2 p}{\partial t^2} = \frac{B}{\rho} \frac{\partial^2 p}{\partial x^2}$$

Here  $p$  is the pressure,  $B$  the bulk modulus of elasticity and  $\rho$  the density.

The spherical case can be obtained if one takes into account the variation of pressure  $p$ , in the other two directions,  $y$  and  $z$ :

$$Eq. 2 \quad \nabla^2 p = \frac{1}{c^2} \frac{\partial^2 p}{\partial t^2}$$

This equation describes the relation between the spatial and temporal variations of pressure in the medium. The sound wave is completely described by the following relations and definitions,

- The velocity of the propagation of the waves :

Eq. 3 
$$c = \sqrt{\frac{B}{\rho}}$$

The bulk modulus  $B$  is a measure of the ratio between the stress and the strain. It is the capacity of the material to be deformed by an external force. The density  $\rho$  is controlled by the amount of material per unit of volume. The sound speed is directly proportional to the ability of the medium to be deformed and inversely proportional to the amount of material per unit of volume.

- The impedance of the medium to the waves:

Eq. 4 
$$Z_0 = \sqrt{\rho B} = \rho c$$

- The particle displacement  $\mathbf{x}$  versus pressure  $p$  and velocity  $u$  (plane wave case):

Eq. 5 
$$p(t, x) = -B \frac{\partial \mathbf{x}(t, x)}{\partial t} = -\rho c u(t, x)$$

### 2.1.3. Solution of the wave equations

The equations are solvable as long as the different variables of the system of coordinates chosen are separable. The pressure of a spherical wave radiated by an infinitesimally small pulsating sphere in an infinite, homogeneous and isotropic medium will have an equation of the type:

Eq. 6 
$$p(r, t) = \frac{A}{r} e^{j(\omega t - kr)}$$

$A$  is a constant determined by a boundary equation,  $r$  the distance from the source,  $\omega$  the period and  $k$  the wave number [Burdic, 1991], [Tolstoy, 1966].

The energy carried by a sound wave is proportional to  $p^2$ .  $p$  is proportional to  $\frac{1}{r}$ , so the energy is proportional to  $\frac{1}{r^2}$ . The energy decreases by the square of the distance to the source. This phenomenon is called spherical spreading.

## 2.2. A SOUND WAVE IN THE OCEAN

The particular case of sound propagation that concerns us is the propagation of sound through water in the ocean and more specifically in coastal waters. In this section, the particularities of the propagation of sound in seawater are investigated.

### *2.2.1. Structure of the ocean as a sound propagating medium*

Unlike in the open ocean where the sound speed profile has a predictable and stable shape, in coastal and shallow water areas, (continental shelf regions) the sound speed profiles are irregular and unpredictable. The velocity of sound (Eq. 3) in seawater depends on three characteristics of the seawater: its temperature, its pressure and its salinity. Figure 1 gives a schematic representation of the influence on sound speed in coastal waters.

The **temperature** varies with depth due to the penetration of solar energy into the water column; with time, on a daily and on a seasonal cycle; and with the weather conditions for example overcast versus sunny periods. Geothermal phenomena, currents and tides, also locally influence the temperature of the water.

The **pressure** of seawater is related to depth. Seawater is compressible and the density of seawater increases with depth (pressure).

The **salinity** is measured as the amount of chlorine ions (absolute salinity  $S_A$ ) or as the electrical conductivity (practical salinity  $S$ ). Salinity is highly variable in shallow areas. Freshwater river runoff, evaporation (related to the wind and solar heat) and precipitation have



a major role in salinity changes. A halocline, a zone of rapid increase of salinity, appears between the upper, low-salinity layer and deeper high-salinity layer [Pickard, 1990].

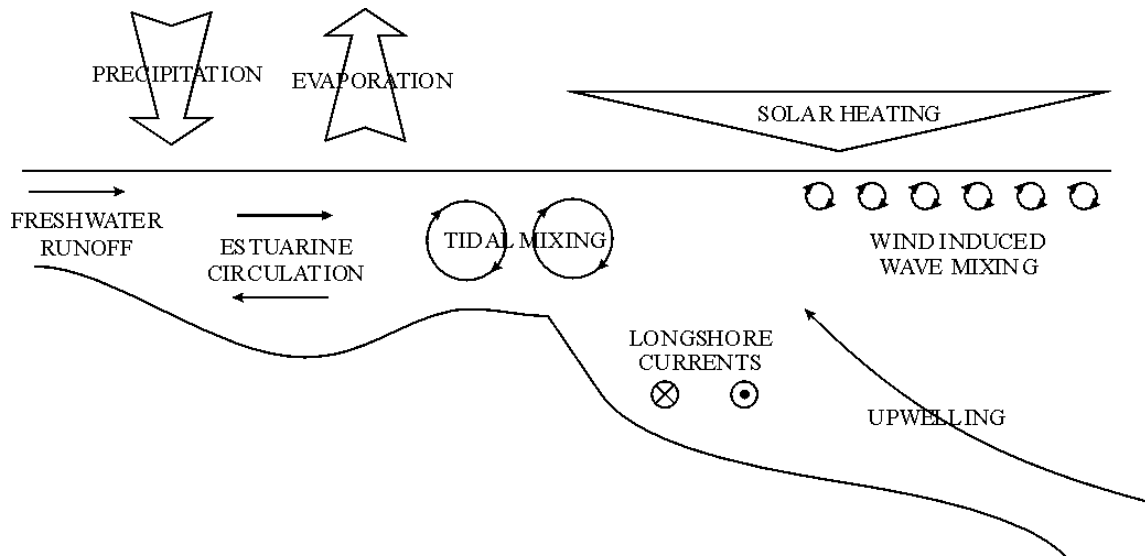


*Figure 1: The complexity of the oceanography of coastal watermasses. Many external force mechanisms influence the velocity structure [Hughes Clarke, 1999a].*

### 2.2.2. The sound speed equation

Empirical equations for the sound speed, as a function of the pressure, salinity and temperature have been established based on a compilation of many measurements [Kuwahara,

1939], [Del Grosso, 1952], [Wilson, 1960]. Three recent equations respectively from [Leroy, 1969], [Medwin, 1975] and [Mackenzie, 1981] are written as follows:

*Eq. 7* [Leroy, 1969]

$$c = 1492.9 + 3(T - 10) - 6 \times 10^{-3} (T - 10)^2 - 4 \times 10^{-2} (T - 18)^2 + 1.2(S - 35) + 1.6 \times 10^{-2} D$$

with  $2 \leq T \leq 24.5^\circ$ ,  $30 \leq S \leq 42$ ,  $0 \leq D \leq 1000$

*Eq. 8* [Medwin, 1975]

$$c = 1449.2 + 4.6T - 5.5 \times 10^{-2} T^2 + 2.9 \times 10^{-4} T^3 + (1.34 - 10^{-2} T)(S - 35) + 1.6 \times 10^{-2} D$$

with  $0 \leq T \leq 35^\circ$ ,  $0 \leq S \leq 45$ ,  $0 \leq D \leq 1000$

*Eq. 9* [Mackenzie, 1981]

$$c = 1448.96 + 4.591T - 5.304 \times 10^{-2} T^2 + 2.374 \times 10^{-4} T^3 + 1.340(S - 35) + 1.630 \times 10^{-2} D + 1.675 \times 10^{-7} D^2 - 1.025 \times 10^{-2} T(S - 35) - 7.139 \times 10^{-13} TD^3$$

with  $0 \leq T \leq 30^\circ$ ,  $30 \leq S \leq 40$ ,  $0 \leq D \leq 8000$

$S$  is defined as the weight in grams of dissolved solids contained in 1 kg of seawater, expressed in parts per thousand (‰).  $T$  is expressed on the Celsius scale and  $D$  in metres.

The typical sensitivities of sound speed  $c$ , with respect to temperature  $T$ , salinity  $S$  and depth  $D$  are [Pickard, 1990]:

At  $T=0^{\circ}\text{C}$  and  $S=35\text{‰}$        $c$  increases by 4.6 m/s for a change in  $T$  of  $+1^{\circ}\text{C}$ ;  
     $c$  increases by 1.4 m/s for a change in  $S$  of  $+1\text{‰}$ ;  
     $c$  increases by 1.7 m/s for a change in  $D$  of  $+1000\text{ m}$ .

### 2.2.3. Refraction

After the general description of sound propagation above, the focus is now brought on how a sound wave actually propagates through the water column. This is important for our study because it is the source of errors in the propagation of beams from the transducer of a multibeam echosounder to the bottom of the ocean and back.

In the simplest model, the ocean can be described as a layered medium. This means that a vertical beam is orthogonal to the layers and that all other angles are oblique with respect to the layers.

First we consider the simple case of vertical propagation i.e. the nadir beams. In order to explain how a sound wave is influenced by a sound speed constantly varying with depth, two situations are explained: that of an oblique ray crossing (1-) a single sound speed discontinuity and (2-) a constant sound speed gradient. In the two cases, we assume we are far enough from the emitting source to be able to justify a plane wave approximation.

#### 2.2.3.1. Vertical case: harmonic mean and nadir beam stability

When a sound wave is sent vertically through the water column, it travels through the medium at the local sound speed, which is variable. To get a representative value of the sound speed in the water column, the concept of harmonic mean sound speed is used. The harmonic mean sound speed is the ratio of the total distance traveled by the total time of travel. It is given by the following formula:

*Eq. 10*

$$m = \frac{z - z_0}{\sum_{i=1}^N \int_{z_i}^{z_{i+1}} \frac{dz}{c_i(z)}}$$

where  $z - z_0$  is the total distance traveled,  $[z_i, z_{i+1}]$  is the layer traveled at the sound speed  $c_i(z)$  and  $N$  is the number of layers, [de Moustier, 1999].

The nadir beams of a multibeam echosounder are emitted vertically from the transducer. A change of speed in the water column generates an error in the propagation of these beams. These range errors are fairly small; for example, a layer of 1510 m/s (equivalent to a 2° temperature rise) added to the first 10 m of a uniform 1500 m/s water column generates errors of 6.6 cm amplitude at a depth of 100 m (0.07% of the water depth).

The next two paragraphs deal with beams travelling through the water column in a direction other than vertical. These beams are deviated from their trajectory by variations of sound speed. The angular errors resulting are added to the range errors present and are non-linearly increasing with the angle from vertical.

### 2.2.3.2. Oblique incident wave crossing a sound speed boundary

This paragraph takes its information from the following references: [Brown, 1989], [Kinsler, 1982], [Urick, 1983], [Burdic, 1991]. The situation is illustrated in Figure 2.

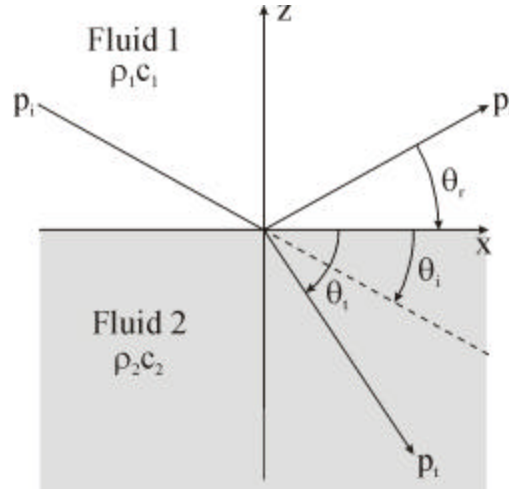


Figure 2: Sound speed discontinuity crossed by an incident plane wave [Burdic, 1991].

The ray directions in Figure 2 are perpendicular to the plane waves described below in Eq. 11 to Eq. 13. Considering the configuration of Figure 2, the incident wave equation  $p_i$  is expressed as follows: (see the solution of the sound wave equation in §2.1.3)

$$Eq. 11 \quad p_i(t, x, z) = A_1 e^{j\omega(t - \frac{x \cos \mathbf{q}_i + z \sin \mathbf{q}_i}{c_1})}$$

As well for the reflected wave  $p_r$  and refracted wave  $p_t$ :

$$Eq. 12 \quad p_r(t, x, z) = B_1 e^{j\mathbf{w}(t - \frac{x \cos \mathbf{q}_r + z \sin \mathbf{q}_r}{c_1})}$$

$$Eq. 13 \quad p_t(t, x, z) = A_2 e^{j\mathbf{w}(t - \frac{x \cos \mathbf{q}_t + z \sin \mathbf{q}_t}{c_2})}$$

Relations between the three different amplitudes ( $A_1$ ,  $B_1$ ,  $A_2$ ) may be found by expressing the conditions at the interface of the two layers through the conservation of pressure (Eq. 14), continuity of the velocity on the  $z$ -axis (Eq. 15), equality and opposition of the reflected and incident angle (Eq. 16), and finally Snell's law (Eq. 17):

$$Eq. 14 \quad p_i + p_r = p_t$$

$$Eq. 15 \quad u_i \sin \mathbf{q}_i + u_r \sin \mathbf{q}_r = u_t \sin \mathbf{q}_t, \text{ } u \text{ being the speed.}$$

$$Eq. 16 \quad \mathbf{q}_i = -\mathbf{q}_r$$

$$Eq. 17 \quad \frac{\cos \mathbf{q}_i}{c_1} = \frac{\cos \mathbf{q}_t}{c_2}$$

These conditions lead directly to the following relations between the amplitudes ( $Z_i = \mathbf{r}_i c_i$  is the impedance):

$$Eq. 18 \quad A_1 = B_1 + A_2$$

$$\text{Eq. 19} \quad \frac{B_1}{A_1} = \frac{Z_2 \sin \mathbf{q}_i - Z_1 \sin \mathbf{q}_t}{Z_2 \sin \mathbf{q}_i + Z_1 \sin \mathbf{q}_t}$$

$$\text{Eq. 20} \quad \frac{A_2}{A_1} = \frac{2Z_1 \sin \mathbf{q}_t}{Z_2 \sin \mathbf{q}_i + Z_1 \sin \mathbf{q}_t}$$

Eq. 18 indicates that the incident wave loses some energy at the transition between the two layers. Eq. 19 quantifies the amount of reflection observed. Eq. 20 compares the incident and refracted amplitude.

There will be no reflection if  $B_1=0$  or if  $Z_2 \sin \mathbf{q}_i = Z_1 \sin \mathbf{q}_t$ . This condition combined with Snell's law (Eq. 17) leads to:

$$\text{Eq. 21} \quad \sin^2 \mathbf{q}_i = \frac{(c_1/c_2)^2 - 1}{(\mathbf{r}_2/\mathbf{r}_1)^2 - 1}$$

This equation is positive because  $\sin^2 \mathbf{q}_i \in [0,1]$ . Eq. 21 is equivalent to one of the two conditions in Eq. 22:

$$\text{Eq. 22} \quad \frac{\mathbf{r}_2}{\mathbf{r}_1} \geq \frac{c_1}{c_2} \geq 1 \text{ and } \frac{\mathbf{r}_2}{\mathbf{r}_1} \leq \frac{c_1}{c_2} \leq 1$$

The wave goes through the boundary without being reflected and without losing energy. It only deviates from its original heading. This is of course the general case for propagation in the ocean volume, which is the focus of our thesis. However, a fixed step is a poor model for a

real ocean. A closer representation of the ocean may be provided by a linear gradient model that is examined next.

#### 2.2.3.3. Oblique incident wave crossing a linear sound speed gradient

[Brown, 1989], [Kinsler, 1982], [Urlick, 1983], [Burdic, 1991]

The discontinuity occurring at a certain depth  $z$  is an approximation used to model a strong variation of sound speed within a short (but not null) depth range. A better approximation would be to model the effect of the thermocline by a continuous sound speed gradient in a non-null depth interval. Such a gradient could be defined by the following equation

$$\text{Eq. 23} \quad c(z) = c_0 + gz$$

where  $c_0$  is the surface sound speed and  $g$  the gradient.

If we differentiate this equation we get:

$$\text{Eq. 24} \quad dc = g dz$$

Snell's law applied in this case gives at a certain depth  $z$ :

$$\text{Eq. 25} \quad \frac{\cos \mathbf{q}}{c} = \frac{\cos \mathbf{q}_0}{c_0}$$

This equation differentiated is written:



$$\text{Eq. 26} \quad \frac{dc}{c_0} = \frac{-\sin \mathbf{q} d\mathbf{q}}{\cos \mathbf{q}_0}$$

By substituting (Eq. 24) and (Eq. 26) we get the relation between the depth increment  $dz$ , and the local direction of propagation  $\theta$ , and its gradient  $d\theta$ .

$$\text{Eq. 27} \quad dz = -\frac{c_0}{g} \frac{\sin \mathbf{q}}{\cos \mathbf{q}_0} d\mathbf{q}$$

A last integration brings:

$$\text{Eq. 28} \quad z(\mathbf{q}) = -\frac{c_0}{g \cos \mathbf{q}_0} \cos \mathbf{q} + A$$

This equation defines a circle that has a radius  $R$ :

$$\text{Eq. 29} \quad R = \frac{c_0}{g \cos \mathbf{q}_0}$$

The wave crossing an area where the sound speed varies linearly with the depth has a circular trajectory, as shown in Figure 3.

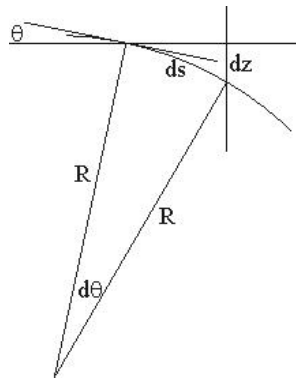


*Figure 3: Circular trajectory of a sound wave in a sound speed gradient [Burdic, 1991].*

This can then be applied to modeling propagation through a heterogeneous medium such as the ocean.

#### 2.2.3.4. Practical application of this theory to oblique propagation in the ocean

Usually a sound speed profile (SSP) has a complex structure. This makes a direct computation of the true deviation created by such profiles impossible. However, the usual method used to simplify a profile for analysis consists of its decomposition into a large number of small segments. Those segments can have a constant sound speed (see §2.2.3.2) or a velocity linearly dependent on the depth (see §2.2.3.3). See Figure 4.

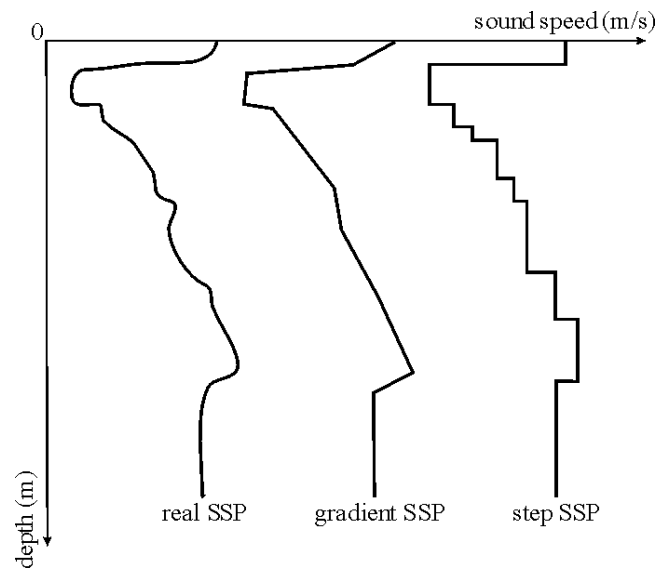


*Figure 4: Two approximations of a real sound speed profile on the left. The gradient SSP in the middle is composed of simple linearly varying steps. The step SSP on the right is composed of constant steps.*

#### 2.2.3.5. Vertical beams vs. oblique beams

Figure 5 compares the amplitude of vertical error (range error) to the amplitude of oblique error (range and angle error). This is realized for different angles of propagation using the same example as in §2.2.3.1. of a small range error produced by the addition of a 10 m/s faster layer to the first 10 m of a uniform water column with a sound speed of 1500 m/s. The nadir beams are almost unaffected compared to the most oblique beam. This is a very important point, because the vertical beams can then be used as references to estimate the corrections to apply on the outer beams.

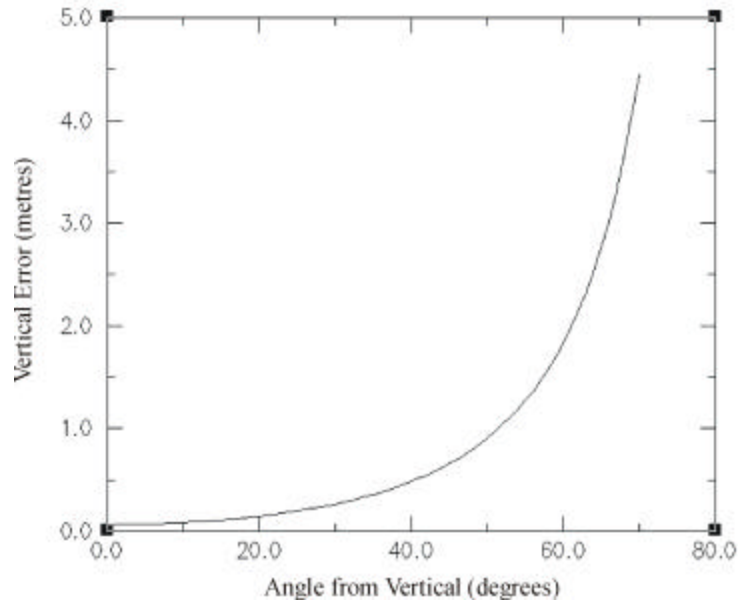


*Figure 5: Comparison between depth errors generated vertically at different angles from vertical and at a depth of 100m. The water column was initially uniform with a sound speed of 1500m/s. Then 10m/s have been added to the speed in the first 10 metres.*

In the following chapters, particular attention will be paid to refraction errors generated in the beams emitted obliquely. These errors are of primary interest here. Before proceeding, a brief description of the operation of multibeam echosounder is necessary.

### 2.3. DESCRIPTION OF MULTIBEAM ECHOSOUNDERS

Hydrographic surveying has evolved with the increasing capabilities in real-time computing and in data storage. Single beam echosounders have been replaced by high-resolution swath mapping systems. Multibeam sonars are one of these high-density mapping tools. These systems use sound waves propagating obliquely in the ocean and are thus very sensitive to refraction phenomena [Hughes Clarke, 1996a].

#### *2.3.1. General description*

Multibeam sonars are echosounder systems that measure simultaneously a series of depths in an athwartship direction. Multibeam sonars are composed of a transducer, a transceiver and a processing unit. The transducer generates a fan of beams that are sent towards the seafloor. The same transducer receives the reflected energy coming from the collision of these beams with the seafloor. The transceiver generates the signals sent to the transducer and gathers the signals received by the same transducer. The processing unit computes the depth and position of the sounding (bottom detection) from the transit time of the signal and the angle of the beam. It integrates this solution with external data such as position and orientation of the ship and the water column measurements.

### *2.3.2. Transducer*

#### 2.3.2.1. Material

The transducer of a multibeam sonar is usually made of ferroelectric polycrystalline ceramics. These materials (also called electro-acoustic transducers) have piezoelectric properties, which allows them to convert electric energy into elastic energy and then into acoustic energy and vice-versa, from acoustic energy into electric energy. In the multibeam case, transducer elements made of this kind of material are arranged in a array configuration.

#### 2.3.2.2. Configuration

A multibeam sonar transducer is usually composed of two orthogonal arrays of elements (constituting a Mill's cross placed under the keel of the vessel). One of these arrays is a receive array and the other is a transmit array. The transmit array is arranged in an alongship direction. It generates a beam pattern that is narrow in the alongship direction (a few degrees) and wide in the athwartship direction (up to 80° to either side of nadir). The receiving array is set up

orthogonally to the transmit array, athwartship. Therefore, it creates a beam pattern that is narrow in the athwartship direction and wide in the alongship direction. The result of the product of these two beam patterns is a narrow beam that ensonifies an area in the seafloor in a specific azimuth and depression angle. Receive beam patterns are steered simultaneously from port to starboard at a certain angle interval. This creates a series of narrow beams arranged as a fan in an athwartship plane under the vessel [de Moustier, 1988], [Pohner, 1991], [Wilson, 1988], [Bobber, 1988], as shown in Figure 6.

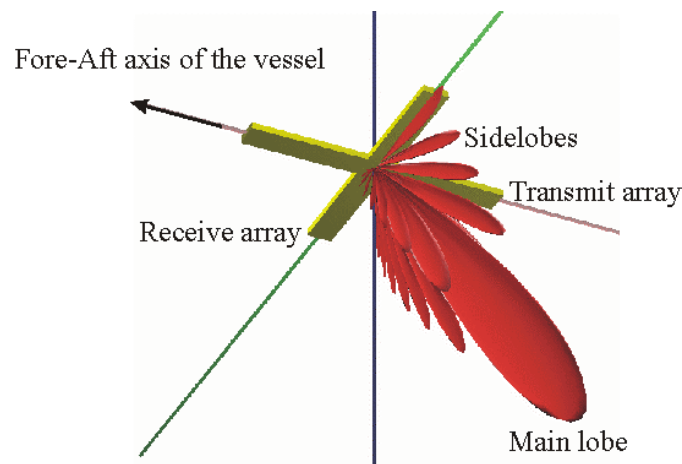


*Figure 6: Narrow beam created by a Mill's cross transducer of a multibeam sonar, it is the result of the product of the beam patterns of the transmit array and the receive array [Hughes Clarke, 1999a].*

### 2.3.2.3. Beamwidth

The sonar is used at a frequency near the mechanical resonance of the material constituting the transducer elements. The beamwidth of the beams generated is defined as twice the angular distance from nadir to the point where the expanding wave front has been reduced to half the power with respect to the axial power level. The beamwidth is inversely proportional to the aperture length of the array and of the wavelength used. The length of the array is therefore critical to the beamwidth generated by the sonar. The equation below defines the 3dB-down (half power) beamwidth for an unshaded unsteered array:

$$\text{Eq. 30} \quad \Delta q = 2 \arcsin \left( \frac{0.44 \lambda}{L} \right)$$

If  $L > 4\lambda$ , then Eq. 30 is simplified as:

$$\text{Eq. 31} \quad \Delta q = 0.88 \frac{\lambda}{L} \text{ (radians)}$$

$\Delta q$  is the beamwidth (angular sector),  $\lambda$  is the wavelength of the emitted signal and  $L$  the length of the array. As an exact rule, assuming a constant beamwidth, high frequencies correspond to small array lengths and vice versa.



#### 2.3.2.4. Element spacing

Another important variable for the design of transducer arrays is the distance between each element of the array. The beamwidth describes the size of the main lobe of the beam pattern. This main lobe is followed by sidelobes that can interfere with depth measurement. The spacing must be chosen in such a way that grating lobes are not present in the visible region. It can be shown that the element spacing that keeps the grating lobes outside of the visible region is lower than one half of the wavelength. The ideal transducer array would be one continuous transducer element. After this optimisation of the element spacing, weighting functions can be applied to reduce the sidelobes.

#### 2.3.3. *Transceiver*

##### 2.3.3.1. Transceiver function

The transceiver performs the beamforming and beam steering operations. Beamforming creates a fan of narrow beams. Beamsteering directs the beam in a specific direction. Some transceivers have the capability to actively compensate for the pitch and the roll of the vessel in order to keep the fan of beams as close as possible to an athwartship vertical plane (pitch

stabilisation) and symmetric with respect to an alongship vertical plane (roll stabilisation). These two major functions are described below.

#### 2.3.3.2. Beamforming

The beamformer allows for separate detection of multiple discrete beams arriving from different directions, at the same time.

The transmit array, parallel to the ship's fore-aft axis, produces a transmit beam orthogonal to it. The receive array forms multiple reception beams parallel to ship. The beam pattern for a single beam is the result of the product of the beam patterns of the transmit and the receive beam.

An unsteered beam pattern can be expressed by the following formula:

$$Eq. 32 \quad b(t, \mathbf{q}) = \sum_{n=1}^{N-1} A_n e^{jn\mathbf{y}} \text{ with } \mathbf{y} = \frac{2pd \sin \mathbf{q}}{l},$$

Here  $N$  is the total number of elements;  $A$  is the amplitude shading of each signal,  $d$  the distance between two elements of the array,  $\mathbf{y}$  the phase of the signal.

A weighting window function (sometimes called "shading") applied to the array reduces the amplitude of the side lobes (functions such as a Dolph-Chebyshev, Hamming or Hanning

[Davids, 1951]). Such a function applies lower weights onto the outer elements of the array and higher weights in the centre of the array. It adjusts the amplitude weights  $A_n$  of each element. This method called "shading" has some drawbacks. It increases the width of the main lobe, decreasing the angular resolution of the sonar and it decreases the array gain, which reduces the main lobe amplitude of the returned echoes [Hughes Clarke, 1996b].

#### 2.3.3.3. Beam steering

Without steering, the narrow beam created by the product of the transmit and receive beam patterns is always directed in the broadside direction (orthogonally to the array). In order to create a fan of narrow beams in the across track direction we need to direct this narrow beam in any of the directions from broadside within the plane of ensonification. This approach, termed beamsteering is usually achieved electronically. Three different methods can be used: time delay, phase delay method and a fast Fourier transform (FFT) method. All these methods rely on using a series of elements spaced in a line at a known distance apart, this distance is equal to some fixed multiple of  $\lambda$ . If we imperfectly know  $k\lambda$  (wrong surface sound speed), the angle estimates will be slightly in error.

- Phase delay beam steering method

The phase delay method consists of adding specific linearly distance varying phase shifts to the output of each of the elements before adding them together. The phase shift  $\Delta y_s$  for the  $n$ th element is:

$$Eq. 33 \quad \Delta y_s = \frac{2\pi d \sin \theta_s}{\lambda}$$

In this equation,  $\theta_s$  is the direction in which we want to steer the beam,  $\lambda$  the wavelength of the signal and  $d$  the element spacing.

This creates a virtual array, defined by the line where all the elements are in phase and the sum of the signals maxima, whose face is directed at a certain angle from broadside of the receive array, see Figure 7.

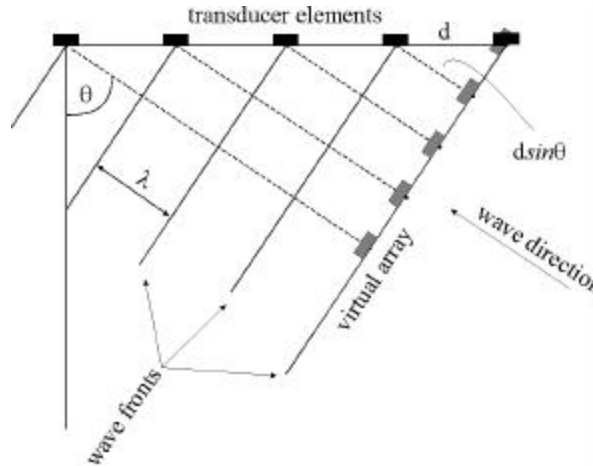


Figure 7: A virtual array created by phase delay added to each of the transducer element.

The steered beam pattern  $b(t, \mathbf{q})$  can then be written:

$$Eq. 34 \quad b(t, \mathbf{q}) = \sum_{n=0}^{N-1} A_n e^{jn(\mathbf{y} - \Delta \mathbf{y}_s)}$$

For a single frequency system, creating this phase shift is equivalent to adding a time delay to each of the hydrophones:

$$Eq. 35 \quad \Delta \mathbf{y}_s = kx = 2pf\Delta t_s = \frac{2pc}{l} \Delta t_s, \quad \Delta t_s = \frac{d \sin \mathbf{q}_s}{c}$$

In this equation  $k$  is the wave number,  $x$  the added distance.

These time delays correspond to the geometric time delays at each hydrophone of a plane wave coming from the direction  $\mathbf{y}_0$  [de Moustier, 1998].

- Fast Fourier Transform (FFT) method

Unlike the phase and time delay methods in which the angle is assumed and the time to bottom detection is sought, this beam forming technique consists of the determination of the angle of arrival of the echoes, the time of arrival is assumed to be known. This is realized in a few steps. The acoustic pressure created by an incident echo on the  $n$ th element is expressed by:

$$Eq. 36 \quad p(n) = Ae^{j(\omega_0 t + k \cdot n \cdot d \sin \mathbf{q} + \mathbf{j}_0)}$$

Here,  $A$  is the amplitude of the wave,  $\omega_0$  the transmitting frequency,  $k$  the wave number,  $d$  the distance between two elements,  $j_0$  the phase integration constant and  $\mathbf{q}$  is the incident angle.

Then we gather all these signals arriving on each hydrophone at a certain time,  $t_0$  and we run a Discrete Fourier Transform on it:

$$Eq. 37 \quad S(m) = \sum_{n=0}^{N-1} p(n)_{t=t_0} e^{-j \frac{2\mathbf{p}mn}{N}} = A e^{-j(\omega_0 t_0 + \mathbf{f}_0)} \frac{\sin(KN/2)}{\sin(K/2)} e^{-j(N-1)K/2}$$

$$\text{with } K = k.d.\sin \mathbf{q} - \frac{2\mathbf{p}}{N}m \text{ and } m \in \left\{ -\frac{N}{2}, \dots, -2, -1, 0, 1, 2, \dots, \frac{N}{2} \right\}$$

We know now the expression of the beam pattern at  $t_0$ . The power of this beam pattern can then be written:

$$Eq. 38 \quad P(m) = \frac{S(m)S^*(m)}{A^2} = \left| \frac{\sin(KN/2)}{\sin(K/2)} \right|^2$$

The power reaches a maximum when the angle  $\mathbf{q}$  has the following value:

$$Eq. 39 \quad \mathbf{q} = \sin^{-1} \left( \frac{2\mathbf{p}m}{Nkd} \right)$$

By the Fourier transform the power spectrum distribution of the signal is obtained. This is equivalent to the angular distribution of energy at an instant in time. Then we are able to determine and separate the different angles from which the waves in the signal arrive. This is

possible because a spatial frequency corresponds to a particular incidence of the arrival wave (see Figure 8).

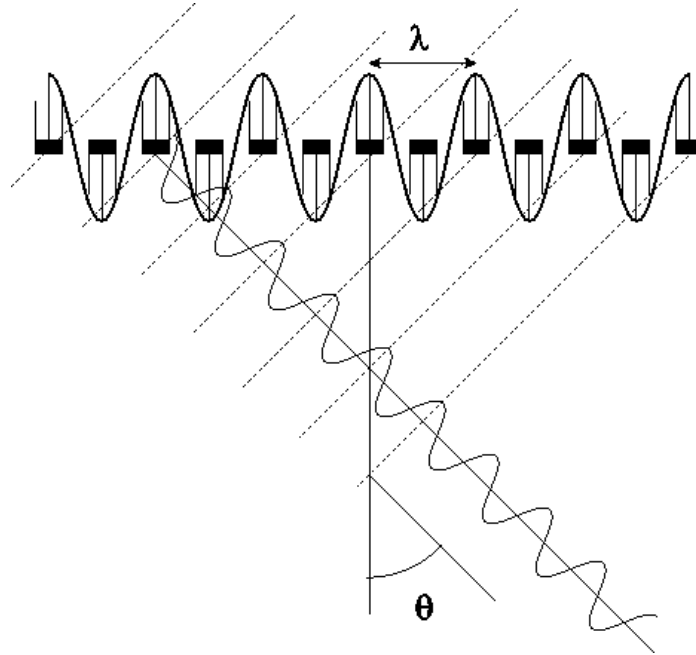


*Figure 8: FFT beamforming: the angle of incidence  $\mathbf{q}$  is determined by the frequency of the signal coming from the hydrophones.*

A Fast Fourier Transform is used rather than a simple Discrete Fourier Transform in order to increase the processing speed. A FFT requires a number of elements be equal to a power of 2. If it is not the case a series of 0 are added to the existing array of elements in order to reach the nearest power of 2. The FFT is run at specific times that determine a series of arbitrary frequencies, which are converted into angles (see Figure 9). An additional interesting facet about this form of processing, is the examination of the time versus angle response within the

ping of the returned signal. This provides a backscatter amplitude sequence of the bottom [Okino, 1986], [Follet, 1994].

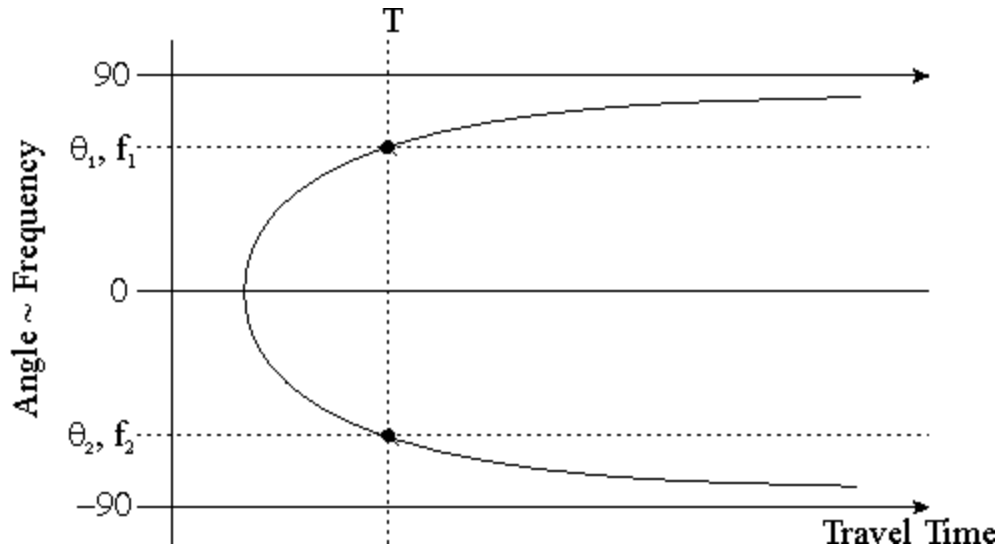


Figure 9: Graph showing the matrix (time, angle-frequency and amplitude). The beam angle is computed from running a FFT on the instantaneous spatial signal across the array.

- A number of caveats need to be borne in mind with regard to beam steering
  - A beam steered from broadside, has a beamwidth that grows in inverse proportion to the cosine of the steering angle.
  - The sound speed at the face of the transducer must be known to determine the phase/time delays to apply to the different elements. An uncompensated change in the sound speed



velocity will introduce errors in the steered angle. The angular error for a given change in sound speed  $\Delta c$  grows with steering angle. This is of particular concern for us as part of this thesis.

- The 3D receive beam pattern geometry changes with the steered angle, from a plane when unsteered, it becomes more curved as the steering angle grows, ending with the geometry of a cone. This effect applied to the transmit beam pattern partially distorts the outer parts of the swath which degrades the uniformity of the coverage. However it maintains the consistency of the swath when beam steering is used to compensate for the pitch affecting the vessel (see §2.3.5.2 for more details).

#### *2.3.4. Bottom detection*

We have formed a narrow beam (except when using the FFT approach), we have steered it in a specific direction, and we now have to detect the instant at which the beam hits the bottom within the returned signal. This is realized in two steps: extraction of the main lobe contribution from the returned echo and then determination from within the main lobe contribution of the time when the beam boresite has reached the seafloor.

#### 2.3.4.1. Extraction of the bottom detect window

From the whole returned time series we must remove the background noise level and the angular response effect to obtain the bottom detect window. As the steered angle increases, the contribution of the main lobe is more and more elongated with decreasing amplitude.

#### 2.3.4.2. Determination of the time of bore site strike

Two methods are used to estimate the instant at which the beam hits the bottom; the amplitude detect method and the phase detect method.

The first is used for the beams with high grazing angles. These beams create narrow footprints on the bottom and send back sharp echoes. The seabed backscatter response can adequately be assumed invariant across the width of the footprint.

This assumption is no longer valid for beams with low grazing angles. The main lobe response becomes longer and the spatial variation in the backscatter response thus has an important impact on the bottom detection amplitude technique.

#### 2.3.4.3. Amplitude detect methods

There are three ways of performing amplitude detection:

- the peak extraction method; looks for the time of maximum intensity within the time series.

- the center of mass method; goes through the intensity time series and stops when half the energy within the main lobe response is already reached.
- the matched filters method; tries to match a model of the likely shape of the bottom echo time series with the real bottom return.

#### 2.3.4.4. Phase detect methods

Amplitude detection methods tend to be less effective as the beam angle with the vertical increases (a flat seabed is assumed here). Another detection method is applied for the outer beams. This technique separates the steered array into two subsections. This is achieved by selecting two sets of elements constituting sub-arrays, whose acoustic axes are separated by the distance of several wavelengths. Each of these two sub-arrays generates an equivalent beam pattern. By finding the zero phase crossing of the complex cross product of the outputs of the two sub-arrays we determine the time of the maximum response axis of the beam. This occurs where the outputs of the two sub-arrays of the steered beam are in phase.

The bottom detection estimation tends to produce uncorrelated errors. They are, therefore, distinct from the kind of systematic errors that this thesis examines. The exceptions are nadir deeps and errors at the phase to amplitude transition (discussed in section 7.9.4) [Hughes Clarke, 1996b].

### *2.3.5. Position and Orientation Integration*

A very critical issue in echosounding is the accuracy of the position associated with the depth measured. The transducer is mounted on the hull of the ship, so one has to determine the position of the ship and make the proper corrections to get the position of the transducer. This position is constituted in horizontal and vertical measurements.

The attitude of the vessel is also required to ensure good quality measurements. The transducer follows the rotation of the ship around the three axes (pitch, roll and yaw). Different techniques are used to keep the ensonification zone stable over time, in order to have a full coverage of the bottom.

#### *2.3.5.1. Position*

- Horizontal: The horizontal position is composed of two coordinates (longitude and latitude) within a reference system (WGS84). The Global Positioning System in C/A-code (GPS), when operated in isolation (no differential) was providing a position with an uncertainty of approximately 100 metres before May 1, 2000. Since this date, the uncertainty has been reduced to 8-9 metres. A more accurate position can be obtained when GPS receivers are used in a differential mode. A receiver is set up at a known fixed location and sends the corrections computed at this known location to the roving receiver on the ship. The system

provides positions at approximately one metre accuracy level usually at a frequency of 1 Hz [Wells, 1998a].

Positional errors due to refraction (the across-track distance) are generally small compared to the scale of targets and ignored.

- Vertical: Vertical positioning accuracy requirements are more stringent than for the horizontal case. The International Hydrographic Organisation (IHO) requires 30 cm accuracy in less than 30 m of water and 1% of the depth in deeper areas [IHO, 1987]. All sources of vertical motion have to be monitored in order to fulfill the requirements.

These sources have a variety of frequencies and origins.

There are long period water level variations (minutes to months) such as river and lake levels (precipitation, snowmelt, dam flooding, seiches), coastal waters weather effects (wind pileup, inverse barometer) and tidal cycles (semidiurnal to diurnal, up to 10 metres amplitude).

There are short period water level variations (several seconds) such as swell-induced heave (amplitude of a few metres, periods of 5-10 seconds).

There are vertical water level variations induced by the motion of the vessel; by the speed (squat, lift of the vessel), by the attitude (roll and pitch), by manoeuvres (turns) and by the variation of the ship's load (fuel depletion).

These different sources of vertical variations of the water level have to be measured. Different sensors are used. Some variations can be predicted, others cannot. Tides are usually

monitored on shore close to the survey area. Heave is measured for each ping of the transducer.

If these vertical positioning issues are imperfectly compensated for they tend to produce two types of anomalies: static shifts and all beams oscillating together. These two anomalies look very different from the refraction artifacts [Wells, 1998b].

#### 2.3.5.2. Orientation

In order to maintain the alignment of the swath with the survey azimuth and the local level, a real time integration must be implemented, by either mechanically rotating the transducer array with respect to the vessel or by electronically steering the receive beam (see §2.3.3.3). The latter technique is considered here.

- Roll: The effect of roll on an uncompensated system causes the swath to move from side to side. In order to prevent this, one can steer the received beams onto a fixed bearing with respect to the local vertical. This maintains a straight swath allowing the hydrographer to get 100% coverage of the bottom (see Figure 10).

- Pitch: The pitch effect on an uncompensated system causes the swath to swing forward and back from the vertical. To keep the swath vertical, the transmit array must be steered with the opposing angle. The drawback of this technique is that the beam pattern is no longer a

plane, it becomes a cone and thus creates an unequally spaced coverage. The outer beams are overcompensated and the inner beams are unchanged. To reduce this effect for sonars with a wide swath, one steers the beams, which under-compensates the inner beams and overcompensates the outer beams. The total divergence from the vertical is less with beam steering than without (see Figure 10).

- Yaw: The yaw effect on an uncompensated system causes the swath to rotate about the vertical. To compensate for this effect, port and starboard sides of the swath need to be steered separately in opposite directions. Unfortunately, this is impossible for a single transducer or at least can only be done one side at a time. The latest generation of multibeam sonars is delivered with multisector yaw/roll/pitch stabilisation. This technique consists in the transmission of a few swaths at different pitch angles. Only parts of the different swaths generated are used in order to recreate one full swath. The swaths are steered at different angles so the different parts are approximately aligned in the athwartship vertical plane (see Figure 10).

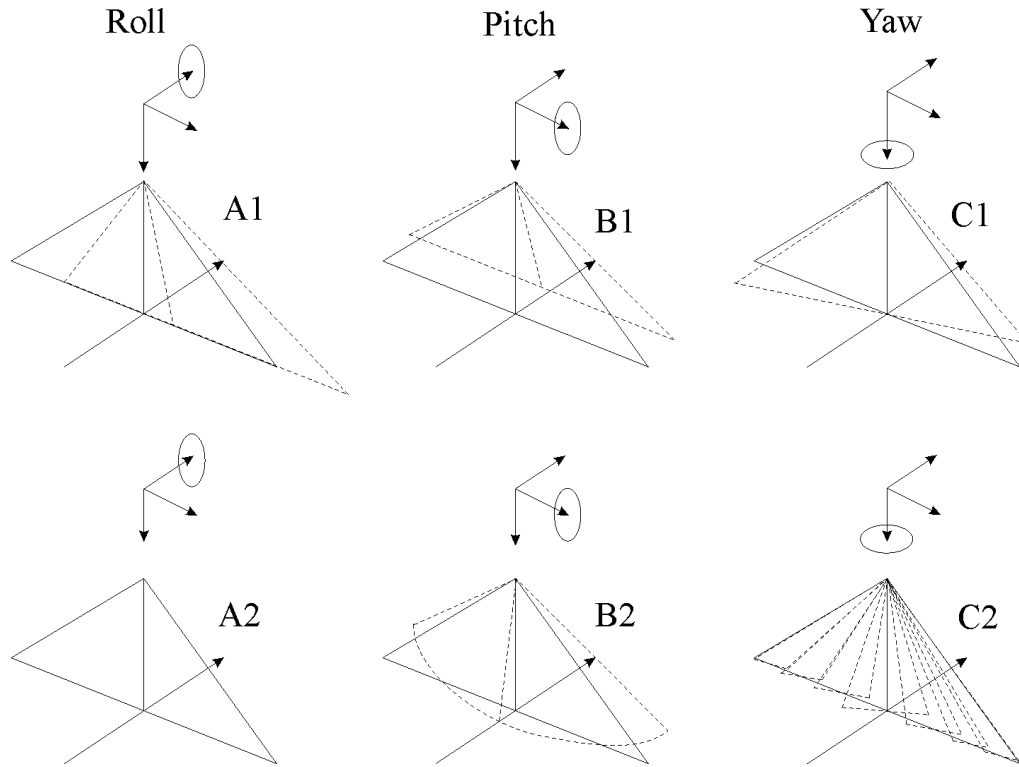


*Figure 10: Beamsteering compensation of the attitude of the vessel. A1, B1 and C1 show the effect of the different rotations on the swath. A2, B2 and C2 show how this effect is corrected: A2 and B2 by beam steering and C2 by multisector stabilisation.*

## 2.4. CONCLUSION

We have concentrated on the refraction phenomena on the one hand and on the other how depth measurements are realized by multibeam. We will now proceed to examine the impact of refraction on these measurements.



## **CHAPTER 3 - REFRACTION IN MULTIBEAM ECHOSOUNDING**

### **3.1. GENERAL**

As we saw in Chapter 2, the sound speed is not constant within the water column. It is influenced by three characteristics of the medium (temperature, salinity and pressure). These characteristics are themselves highly variable. Fluctuations in these characteristics are difficult to monitor in both space and time and degrade the quality of the multibeam soundings. For a small area, a reasonable assumption would be that sound speed varies only vertically with depth. This assumption is made because the sound speed varies much faster vertically than horizontally. As seen in Figure 11, refraction affects the depth measurements at two places: (a) at the transducer face during the beam forming and beam steering operations and (b) during the progression of the sound wave through the water column. Both these effects interest us because they are at the source of the errors that we intend to correct in this thesis.

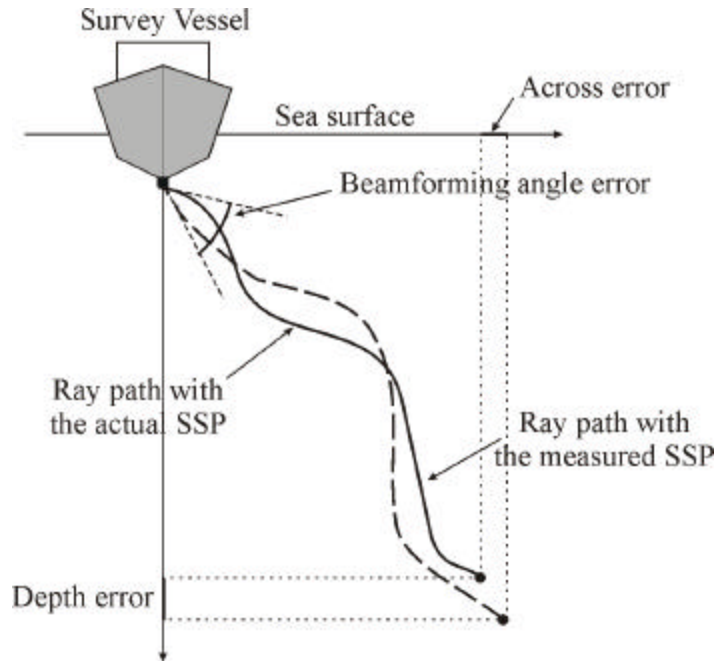


*Figure 11: This sketch shows the propagation of the sound ray through the water column. If the sound speed is not perfectly monitored, it induces beam angle errors at the face of the transducer and with each sound speed error in the water column, deviates the ray from the correct path.*

### 3.2. EFFECT THROUGH THE WATER COLUMN

The ray created by the sonar head has its path direction modified every time the sound speed varies with the depth. The ray path, when computed at the transducer face, should ideally be straight. With the wrong surface sound speed, the ray path will be curved. A

consequence of the assumption that locally the sound speed varies only vertically with depth, is that the deformed swath stays in the plane of emission. The deformation is done within this plane. The trajectory is concave for a positive sound speed gradient and convex for a negative gradient, as shown See Figure 12.

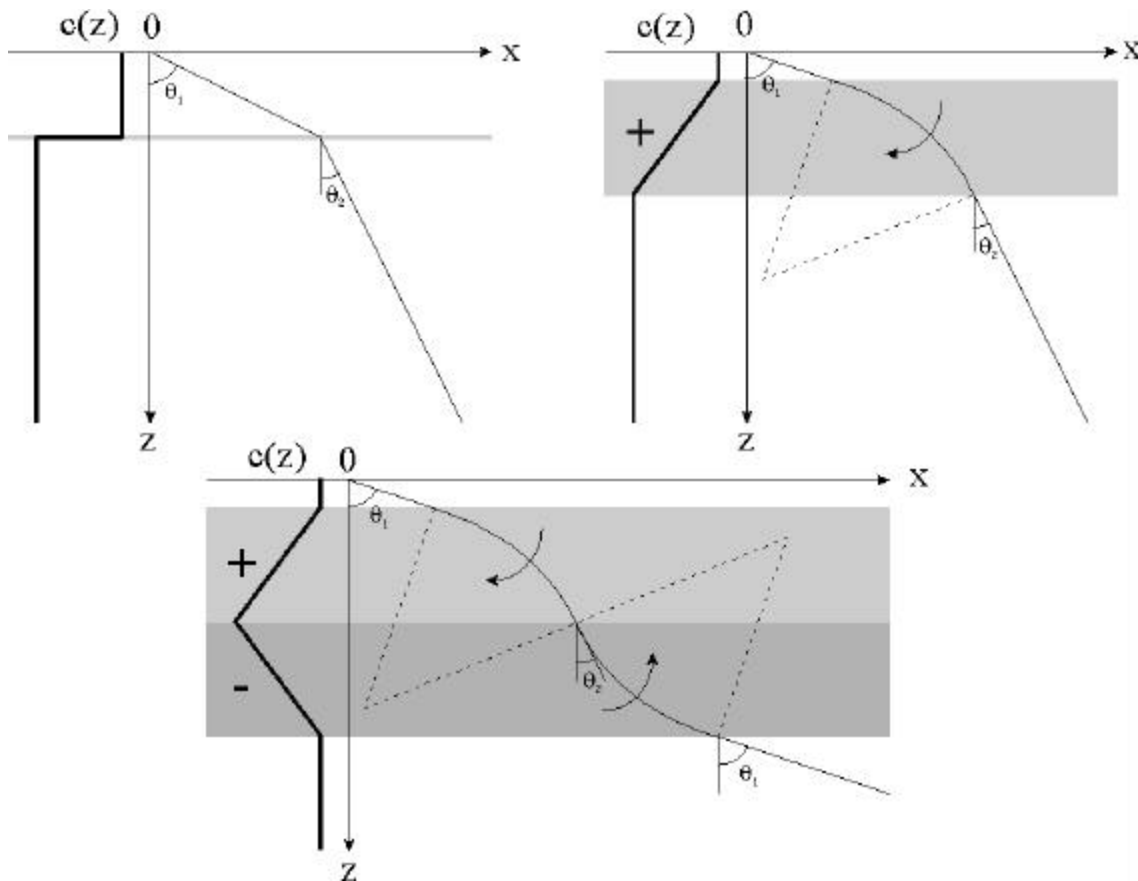


Figure 12: Effect of a step and a gradient SSP on the path of a single beam.

The propagation distance covered is different to the distance that would have been traveled with the initial SSP. There is then a bias in the bottom detection computation. A swath is composed of a fan of beams created at different angles from the vertical. The refraction artifact

- 1- grows non-linearly with the angle from the vertical (Snell's law),
- 2- is symmetric with respect to the vertical and
- 3- is curved upward or downward (see the “smile” and the “frown” in the Figure 13),

The error is very small at nadir because there is no error in beam angles but only range errors due to the variations of speed (see §2.2.3.1), see Figure 13.

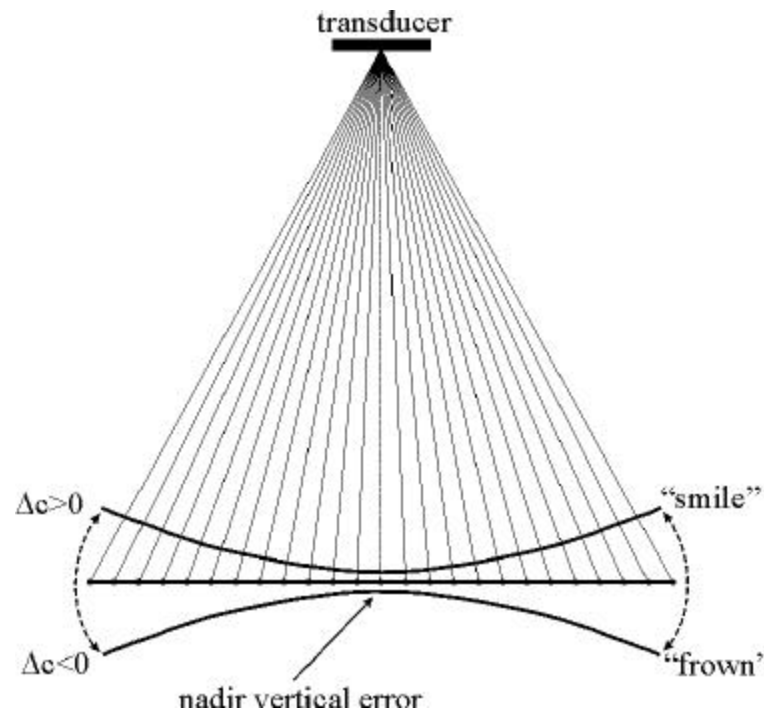


Figure 13: 100 m. deep synthetic flat seafloor deformed by a step sound speed profile.

### 3.3. EFFECT DURING THE BEAMFORMING

The variation of the sound speed at the face of the transducer has an effect on the steering direction of the beam formed. A sonar array is composed by a series of transducer elements usually equally spaced. The acoustic frequency of the transducer and the length of the array in wavelengths determine the beam width of the narrow beams created. As we have seen above, when one steers a beam, the phase delay between two elements is a function of the wavelength:

$$Eq. 40 \quad y_s = \frac{2pd \sin q_s}{l}$$

In this equation,  $d$  is the element spacing,  $l$  the wavelength and  $q_s$  the steering angle. The wavelength itself depends of the sound speed.

$$Eq. 41 \quad l = \frac{c}{f}$$

A variation of sound speed therefore produces a variation of the steered angle. Snell's law computes this angle as follows:

$$Eq. 42 \quad q_1 = \text{Arc sin}\left(\frac{c_1}{c_0} \sin q_0\right)$$

Here  $q_0$  is the intended angle of the beam with respect to normal at the transducer,  $q_1$  is the actual angle,  $c_1$  the assumed sound speed and  $c_0$  the actual sound speed.

The sonars are calibrated with a specific sound speed (usually 1500 m/s the average sound speed throughout the ocean). In the ocean the sound speed close to the surface varies, thus the wavelength  $\lambda$  varies. The beamwidth (see §2.3.2.3) and, more importantly, the direction of the narrow beam depend on the sound speed at the face of the transducer.

A change in the sound speed at the water surface with respect to the one assumed at the face of the transducer will cause the beams to deviate from the direction in which the sonar is supposed to steer (with the single exception of the broadside beam). The magnitude of the angle error  $q_1 - q_0$  depends on the beam pointing angle  $q_0$  (see Figure 14).

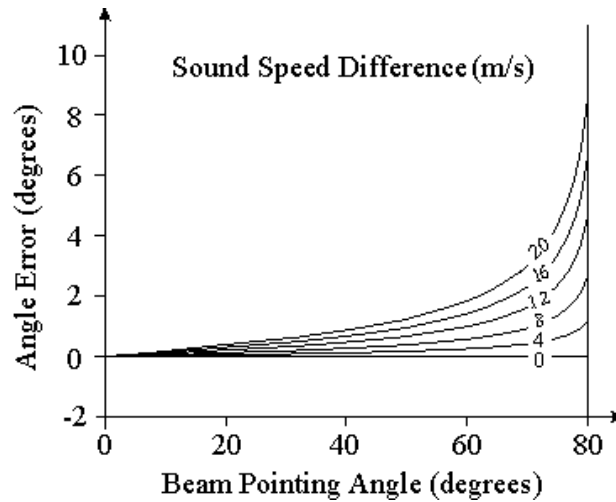


Figure 14: Variation of the magnitude of the angle error with respect to the beam-pointing angle for different sound speed differences.

Figure 14 depicts the way in which angular errors are dependent on the particular array geometry.

We will now proceed to examine the different ways in which refraction affects the swath during beamforming as a function of the actual sonar system. A representative selection of swath systems is considered.

### 3.4. EXAMPLES OF ARRAY FACE REFRACTION EFFECT DURING BEAMFORMING

#### *3.4.1. Introduction*

The objective of this section is to describe the refraction artifact generated by a surface sound speed discontinuity. Numerical models have been developed for a variety of system configurations: a curved array, a flat array, a roll-stabilised flat array, a dual flat array and a dual roll-stabilised flat array. Each individual system will be considered when it is in a level position, then in a fixed tilted position ( $15^\circ$ ) and finally in a linearly varying tilted position (from  $-15^\circ$  to  $15^\circ$ ). The refraction tool developed is applied to data that was acquired using a curved array sonar system.

### 3.4.2. *Curved Array Sonar*

Examples of such a system configuration are the Simrad EM100/950/1000/1002 and the Reson Seabat series 8100 and 9000

#### 3.4.2.1. Mode of operation

A line of transducers combined without any phasing generates a beam orthogonal to itself. A swath system creates a fan of beams arranged at discrete angles from the vertical. Beam steering with a line array accomplishes this. Another way to generate such a fan is to use a circular configuration of elements and transducers, each beam being emitted orthogonally to the tangent of the curved array with no beamsteering required.

Each beam uses a portion of the elements that constitutes the whole array. A weighting function is used to shade the influence of each element, to create a beam pattern with controlled sidelobes.

At the extremities of the circular arc, beamforming is no longer possible because no more elements are available on one side to complete the desired beam. The last set of elements is used again to generate the last beams, these beams are steered electronically to their correct angles.

The example of the Simrad EM1000 system is used in the following sections, see Figure 15. This sonar creates 60 beams in a 150° sector. Two beamforming methods are available; equidistant, the same distance between the beams on a flat seafloor or equiangular, the beams



are generated at equally spaced angles. While the array is level, beam steering is performed in the sectors:  $[-75^\circ; -60^\circ]$  and  $[60^\circ; 75^\circ]$ . When the array is tilted by the roll of the vessel the beamsteering sectors follow the rotation.

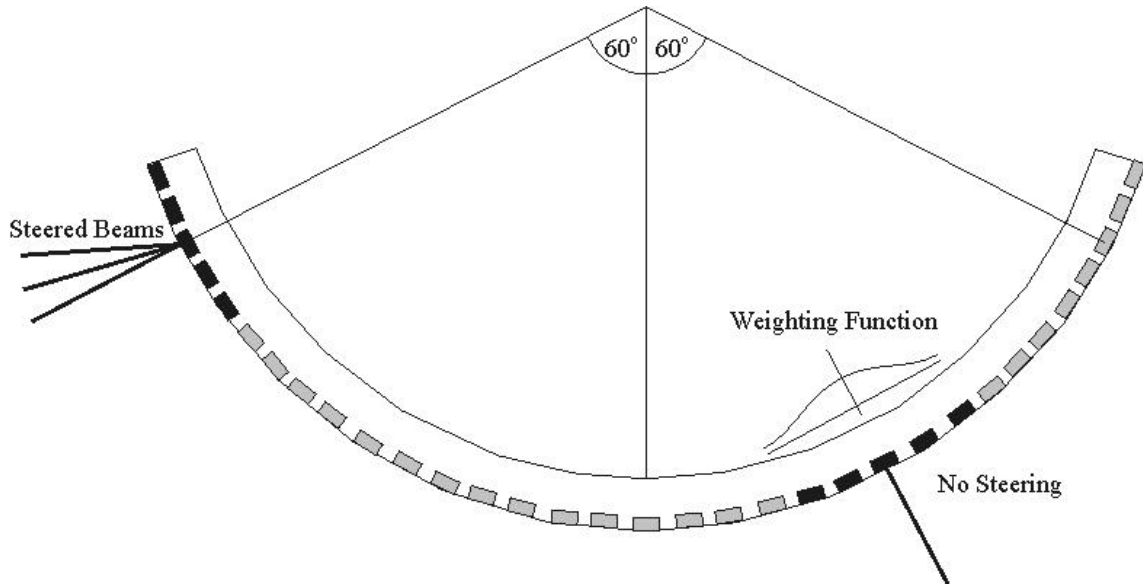


*Figure 15: Beamforming in a curved array transducer configuration. Steering is performed only beyond a certain angle.*

#### 3.4.2.2. Refraction with a curved transducer

The surface discontinuity of the sound speed at the face of the transducer introduces errors only in the angle for the beams that are steered. In the case of a curved array, the beams belonging to the sectors beyond  $\pm 60^\circ$  are those affected as in the case of a Simrad

EM950/1000. If we consider a flat seafloor and then introduce a discontinuity in the sound speed at the surface of the transducer, the flat seafloor is distorted as is shown in Figure 16.

The originally flat seafloor now appears to be composed of three longitudinal segments: 1- the main segment centered at nadir which stays flat, 2- two secondary segments on both sides of the swath which make a certain angle with the main segment.

This angle may be positive or negative depending on the sign of the discontinuity.

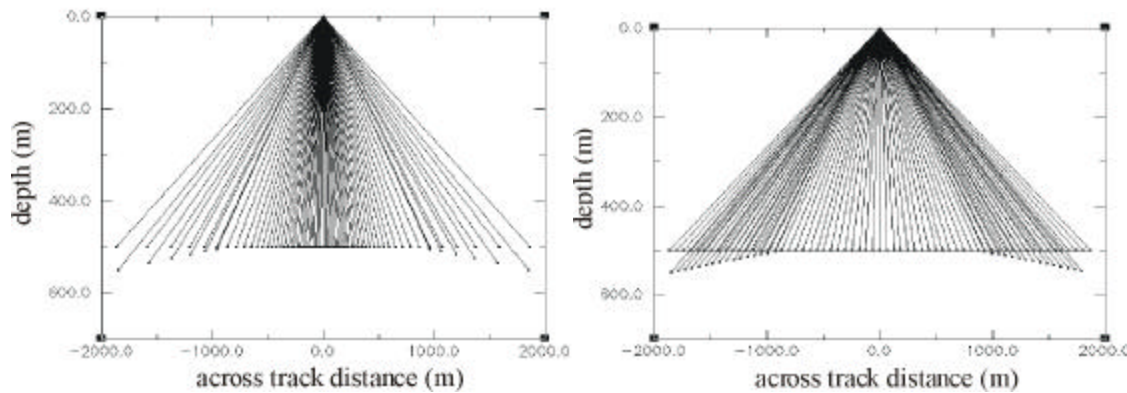


*Figure 16: Impact of a surface sound speed discontinuity on the shape of the swath of a horizontal curved array. Note that the errors induced appear only beyond the angle after which beam steering is performed. Equiangular beam spacing on the left and equidistant beam spacing on the right.*

### 3.4.2.3. Refraction with a positive roll angle

Let us consider now the case of the same curved array but with an angle of  $15^\circ$  from the horizontal. The different angular sectors on the transducer roll identically. The sonar is roll-stabilised, therefore the swath does not move with respect to the vertical. There is a roll value threshold of  $15^\circ$ , after which only two segments appear. The main segment is shifted on one side, increasing one of the secondary segments and reducing or removing the other one, refer Figure 17.

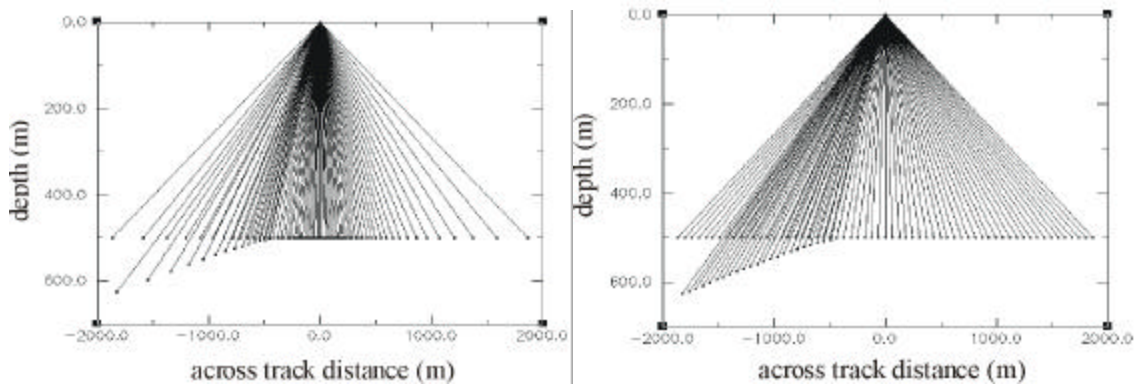


*Figure 17: Impact of a surface sound speed discontinuity on the shape of the swath of a tilted ( $15^\circ$  roll) curved array. Note that the errors induced appear only on one side of the swath.*

#### 3.4.2.4. Visualization of the refraction with a varying roll angle

To visualize the nature of the refraction artifact with the additional variable of a roll angle, we apply the numerical model developed to a survey line, whose characteristics are constrained to:

- 1- a straight survey line,
- 2- an absolutely flat seafloor,
- 3- a sound speed profile presenting a discontinuity at the sea surface and
- 4- a vessel attitude composed strictly by a roll going from  $+15^\circ$  to  $-15^\circ$ .

Figure 18 shows the results of applying the numerical model to this line. As seen in the previous section, with an angle of  $+15^\circ$  the swath consists of two segments, one main flat segment and another secondary disposed at a certain angle from the main segment. As the roll is varying, the main segment is moving across nadir reducing this secondary segment and increasing another secondary segment on the other side of the swath. At the end, with a roll angle of  $-15^\circ$  we are in the symmetrical opposite configuration.

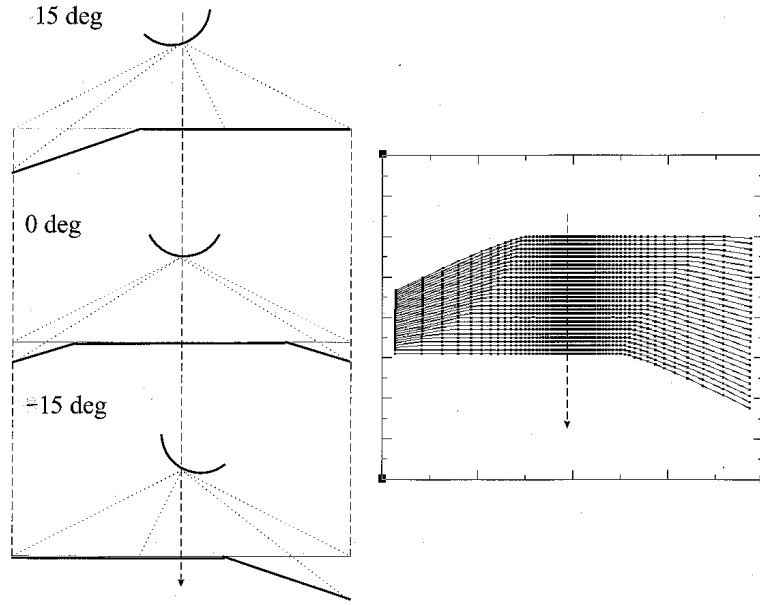


*Figure 18: Shape of thirty successive swaths when the curved array is rolling from  $+15^\circ$  to  $-15^\circ$ . Note that the errors induced are moving proportionally with the roll angle. On the right a 3D plot of the shape of a flat seafloor deformed by such an artifact.*

The artifact due to a surface sound speed discontinuity on a curved array transducer appears then as a dynamic bending of the swath only over a certain fixed outer sector moving back and forth with the roll of the vessel.

An important point to mention is that in the case of curved arrays the time varying component of the surface refraction artifact is averaged out. By averaging the data over a long-enough period of time (this is realized in the algorithms of the processing tool developed), one reduces the surface sound speed artifact to the artifact using zero roll.

### 3.4.3. Flat Array Sonar (without roll stabilisation)

An example of such a system configuration is the Simrad EM3000S.

#### 3.4.3.1. Mode of operation

This sonar is composed of two straight lines of transducers, orthogonal to each other, in the shape of a Mills cross. This sonar performs a Fast Fourier beamforming method [Follet, 1994]. This method consists of the application of a Fourier transform on the instantaneous signal across all the elements of the receive array, in the search for the characteristic spatial frequency which corresponds to a specific angle. The relation between the angle and the beam number is given by [Okino, 1986] (see §2.3.3.3):

$$Eq. 43 \quad \mathbf{q} = \sin^{-1} \left( \frac{2\mathbf{p}m}{N.\mathbf{k}.d} \right)$$

where  $m$  is the element bin number,  $N$  the total number of elements,  $\mathbf{k}$  the wave number ( $\mathbf{k} = \frac{\mathbf{w}}{c}$ ) and  $d$  the distance between adjacent elements. The FFT beam former creates a beam spacing that increases as we move towards the outermost beams. In Figure 19, the beam spacing produced by a FFT method is compared to an equiangular beam spacing. The resolution of the outermost beams is poor for an FFT beamformer.



*Figure 19: Beam spacing of an FFT beamformer (top graph) compared to equiangular beam spacing (bottom graph).*

The Simrad EM3000S (single transducer) system is used in the examples in the following sections, see Figure 20. This sonar creates 127 beams in a  $130^\circ$  sector. A Fast Fourier Transform performs beam steering for all beams simultaneously. It operates at a frequency of 300 kHz in shallow water (0-100 m). The choice of a FFT beamforming has been made because of the high processing speed needed to cope with the high frequency of the sonar, due to the fact that the EM3000S is a shallow water system. There is no roll compensation because beamsteering would slow down the beamformer.

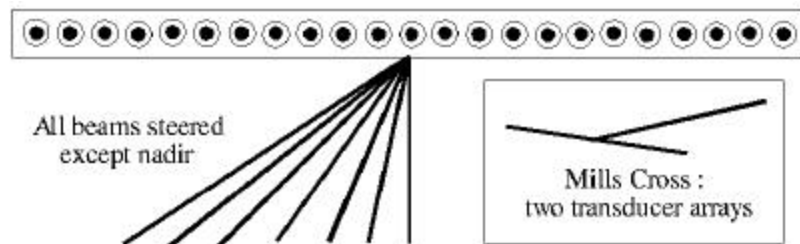


*Figure 20: Beamforming in a line array transducer configuration. Beam steering is performed all over the transducer except at nadir.*

### 3.4.3.2. Refraction with a level transducer

As the beam steering uses the whole length of the line array, all the beam pointing angles (excluding the array normal) are affected by a discontinuity in the surface sound speed. This implies an error over the whole swath; see Figure 21.

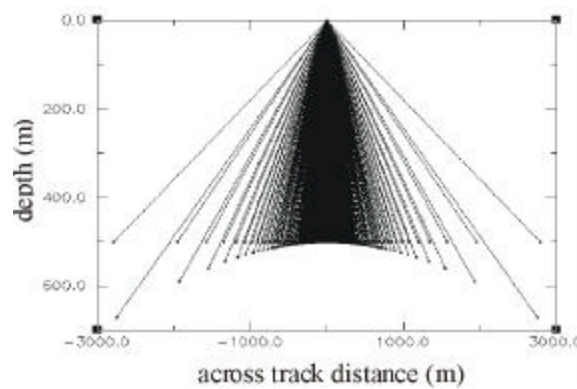


*Figure 21: Impact of a surface sound speed discontinuity on the shape of the swath of a level line array. Note that the errors induced appear all over the swath except at nadir.*

If there is an uncorrected sound speed gradient at the transducer face, the error increases with the grazing angle. It appears as a parabola directed downward or upward depending on the sign of the discontinuity.



#### 3.4.3.3. Refraction with a positive roll angle

The EM3000S does not perform roll-stabilisation, therefore when the ship rolls the swath of this sonar moves to the side. The swath follows the roll of the vessel. The errors seen in the last section move as well; they stay with the same angular error amplitude for a given array-relative steering angle. However, they are no longer symmetrical (see Figure 22).

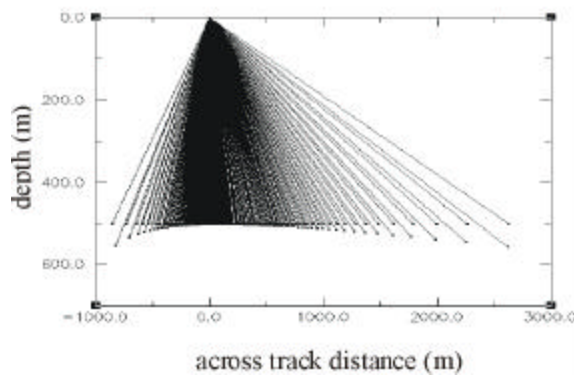


*Figure 22: Impact of a surface sound speed discontinuity on the shape of the swath of a tilted (15°-roll) non roll-stabilised line array*

#### 3.4.3.4. Visualization of the refraction with a varying roll angle

We repeat the same experiment (see §3.4.2.4 for more details) with a variable roll. The sonar does not make any roll adjustment of the swath. If the roll varies from  $+15^\circ$  to  $-15^\circ$  the coverage of the seafloor will move across the straight navigation as shown in Figure 23 .

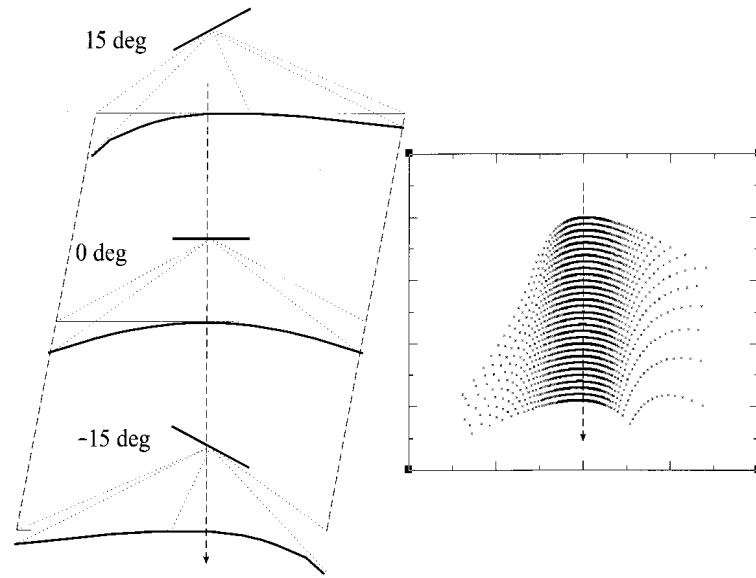


*Figure 23: Shape of thirty successive swaths when the line array is rolling from  $+15^\circ$  to  $-15^\circ$ . In the right sketch the outermost beams have been trimmed out. On the right a 3D plot of the shape of a flat seafloor deformed by such an artifact.*

#### *3.4.4. Motion Stabilised Flat Array Sonar*

An example of such a system configuration is the Simrad EM300.

#### 3.4.4.1. Mode of operation

The Simrad EM300 sonar is a Mill's cross array, as is the EM3000S system. However this sonar is roll stabilised. This means that the swath coverage is a straight strip independent of the roll that affects the vessel.

The Simrad EM300 sonar system creates 135 beams in a  $150^\circ$  sector. Two beamforming methods are available: equidistant (same distance between the beams on a flat seafloor) or equiangular (beams generated at equally spaced angles). Receive beam steering is performed using the whole array. More information about the sonar can be found in [Hammerstad, 1998].

#### 3.4.4.2. Refraction with a level transducer

The same circumstances apply here as with the EM3000S system (see §3.4.3.2). This sonar performs beam steering for all beams, the error due to a surface sound speed discontinuity appears along the entire swath, and the error varies in amplitude with the grazing angle (see Figure 24).

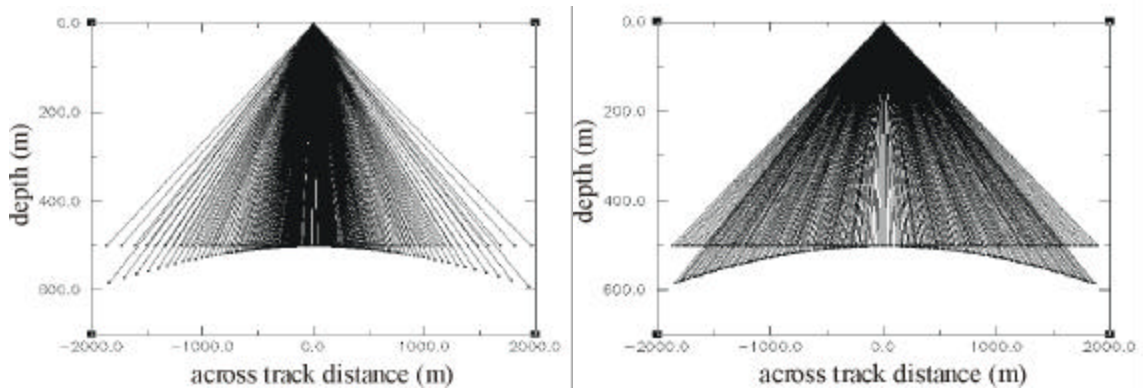


*Figure 24: Impact of a surface sound speed discontinuity on the shape of the swath of a level line array. Note that the errors induced appear all over the swath except at nadir. The beam spacing is equiangular on the left figure and equidistant on the right figure.*

#### 3.4.4.3. Refraction with a positive roll angle

The peculiarity of this sonar is that it stabilises the swath with respect to the roll. To achieve this, the sonar adds the roll angle to the usual steering angle. This implies a larger steering angle on the side rolled down (where the two angles have the same signs), and a smaller steering angle on the side rolled up (where the two angles have opposite signs). The error is proportional to the steering angle. The error is much larger on one side of the swath than on the other (see Figure 25).

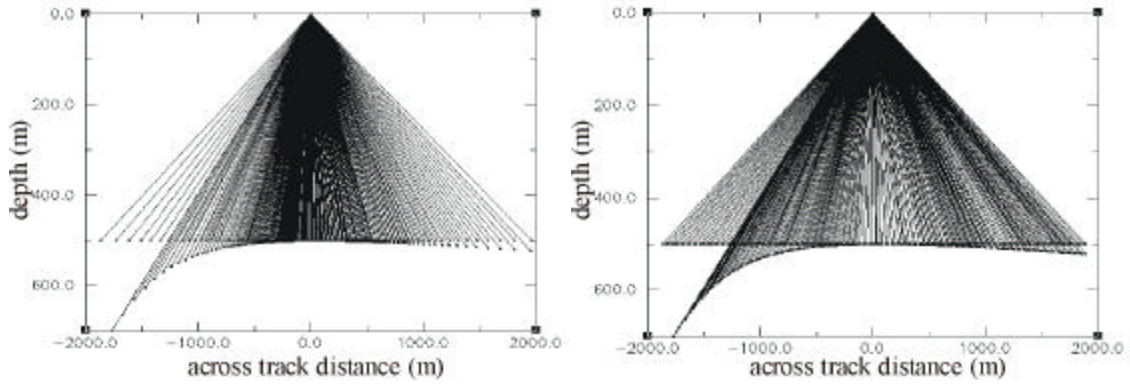


*Figure 25: Impact of a surface sound speed discontinuity on the shape of the swath of a tilted ( $15^\circ$ -roll) roll-stabilised line array. The beam spacing is equiangular on the left figure and equidistant on the right figure.*

#### 3.4.4.4. Visualization of the refraction with a varying roll angle

A similar swath shape to the previous instances described in §3.4.2.4 and §3.4.3.4 occurs here, as shown Figure 26. This time the swath stays parallel to the track of the vessel. The refraction artifact increases and decreases on each side of the swath as the roll varies.

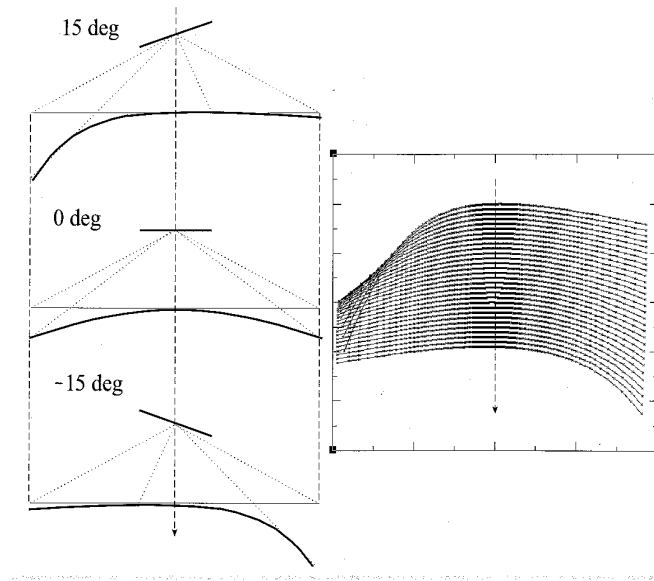


*Figure 26: Shape of thirty successive swaths when the line array is rolling from  $+15^\circ$  to  $-15^\circ$ . On the right a 3D plot of the shape of a flat seafloor deformed by such an artifact.*

#### 3.4.5. Dual Transducer Sonar

An example of such a system configuration is the Simrad EM3000D.

##### 3.4.5.1. Mode of operation

The example of the Simrad EM3000D (dual transducer) system is used in the following sections, see Figure 27. Each Mills cross creates 127 beams in a  $130^\circ$  sector. The two systems are tilted by  $45^\circ$  and mounted on each side of the hull. This configuration allows a

larger coverage. A better spatial resolution in the inner part of the swath is insured by the overlapping coverage between the two transducers. Beam steering is performed simultaneously for all beams for each array by a Fast Fourier Transform method. In the numerical method used, we just look at the beams in the sector  $[-75^\circ, +75^\circ]$  from vertical.

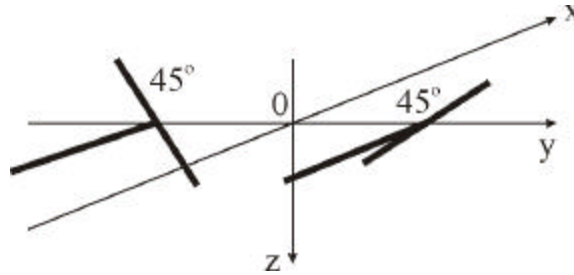


*Figure 27: Transducer configuration with a dual line array. The two Mills crosses make an angle of  $90^\circ$  with respect to each other.*

#### 3.4.5.2. Refraction with a level dual transducer

The refraction error in this situation is a combination of the errors of one line array transducer tilted by  $+45^\circ$  and another one tilted by  $-45^\circ$ . The result of this combination is depicted in the Figure 28. The whole system is symmetric, as are the errors. The errors are null at the location of the two broadside beams. The errors increase towards the nadir area until we reach the outer beams of the transducer pointing in the other direction where they decrease

suddenly. The error starts to increase as we go towards the last beams of the transducer pointing in this direction.

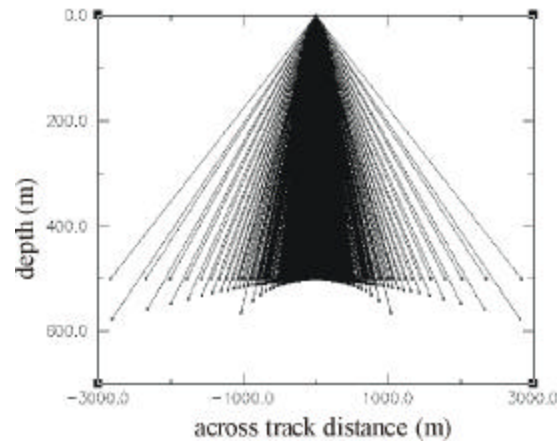


*Figure 28: Impact of a surface sound speed discontinuity on the shape of the swath of a horizontal dual line array. Note that the errors induced appear all over the swath.*

### 3.4.5.3. Refraction with a positive roll angle

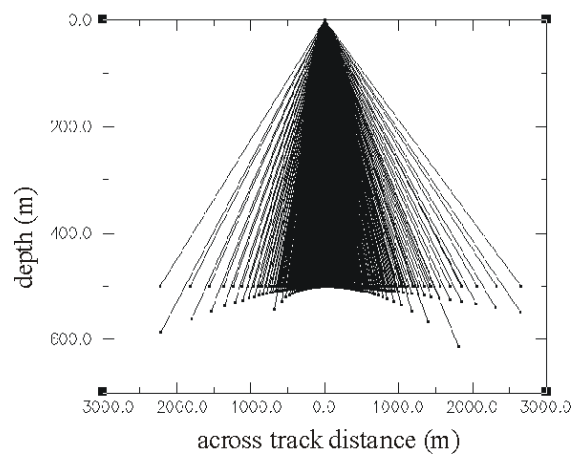




*Figure 29: Impact of a surface sound speed discontinuity on the shape of the swath of a tilted (15°-roll) non roll-corrected dual line array transducer.*

The EM3000D dual system does not have any roll compensation. The shape of refraction errors appears as the superposition of two unequally tilted line array transducers, one by  $45 + 15 = 60^\circ$ , the other by  $-45 + 15 = 30^\circ$ , see Figure 29.

#### 3.4.5.4. Visualization of the refraction with a varying roll angle

The shape of thirty successive beams with a roll going from  $+15^\circ$  to  $-15^\circ$ , can be seen in Figure 30. A narrow stripe of high amplitude errors appears in the middle section of the coverage.

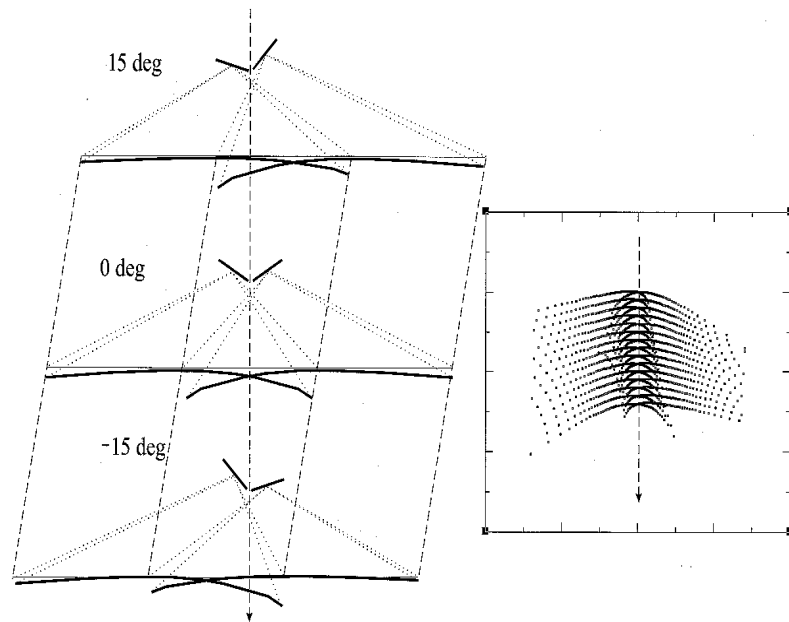


*Figure 30: Shape of thirty successive swaths when the line array is rolling from +15° to -15°. On the left sketch the outer beams have been trimmed out. On the right a 3D plot of the shape of a flat seafloor deformed by such an artifact.*

#### *3.4.6. Roll Stabilised Dual Transducer Sonar*

Examples of such a system configuration are the Simrad EM12D, the ELAC BottomChart, the ATLAS Fansweep and the Hydrosweep MD.

##### *3.4.6.1. Mode of operation*

The configuration of these sonar systems is the same as the EM3000 (see §3.4.5), that of a dual Mill's cross array. However, these systems are roll stabilised. There is also no redundant overlap due to the time/phase delay beamforming method. This permits a control of the beam angles created. Equiangular and equidistant beam spacing are available on these systems. As an example, we have chosen the Simrad EM12D (dual transducer) system, which is a deep water system. The deep-water operation of this system makes the roll stabilisation essential.

### 3.4.6.2. Refraction with a level dual transducer

The refraction with a level dual transducer mirrors the EM3000S case (see §3.4.5.2). There is however, no overlap and the system has the option of both equidistant and equiangular beam spacing.

### 3.4.6.3. Refraction with a positive roll angle

When a positive roll of  $15^\circ$  affects the ship, the roll stabilisation maintains the coverage unchanged. In order to adjust the beams, the two transducers steer more of the beams towards the opposite side to that which the ship is rolling (left in this case). The beams on the right of both transducers then need smaller steering angles than in the level case (see §3.4.6.2.). The effects can be seen in Figure 31. The transducer on the right is already tilted by  $45^\circ$ , additional roll affects its left beams much more than in the level case. It does not have such a bad effect on the transducer on the left (tilted by  $-45^\circ$ ), it is now tilted by only  $30^\circ$ .

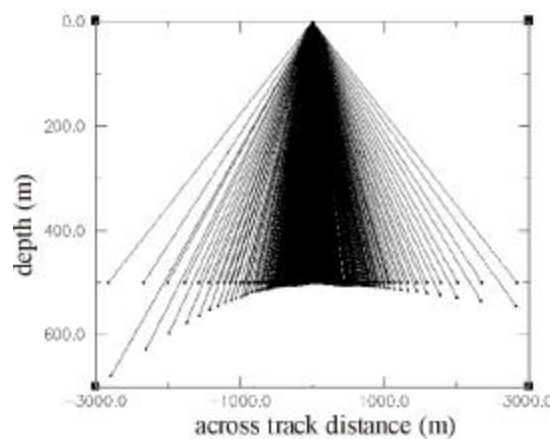


*Figure 31: Impact of a surface sound speed discontinuity on the shape of the swath of a tilted ( $15^\circ$ -roll) roll-stabilised dual line array transducer (equiangular beam spacing case).*

#### 3.4.6.4. Visualization of the refraction with a varying roll angle

Figure 32 shows how refraction artifacts change with varying roll. A constant coverage is maintained; the errors in the inner extremities of the two-transducer swath are strongly dependent on the roll. The errors have less amplitude on the outer extremities of the whole system.

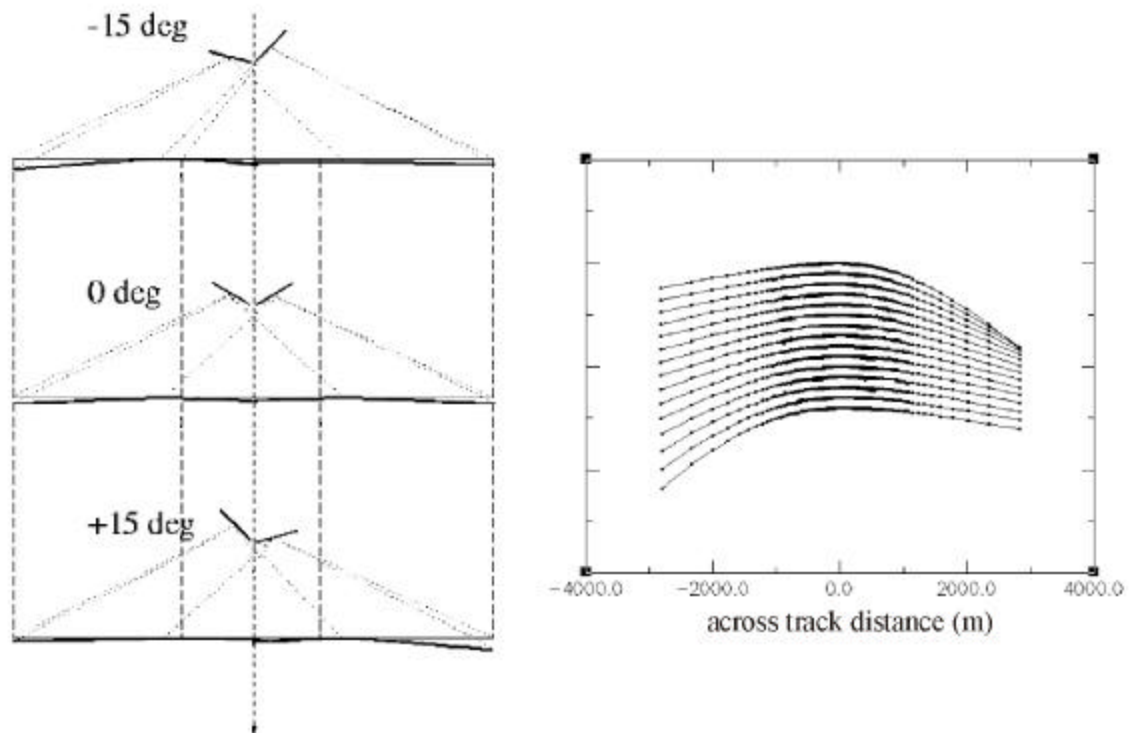


*Figure 32: Shape of thirty successive swaths when the line arrays roll from  $+15^\circ$  to  $-15^\circ$ . The system is roll-stabilised, notice the straight track.*

### 3.5. CONCLUSION

In the proceeding chapter, we have endeavoured to provide an idea of the spectrum and nature of the refraction artifacts that occur due to inadequate monitoring of the sound speed at the face of the transducer and in the water column.

Special attention has been given to the impact of errors in the surface sound speed on a flat seafloor for different sonars and under different roll conditions. These errors are often not evident in a rough and rapidly varying topography. With a knowledge of

- (a) the echosounder configuration used,
- (b) the temporal and spatial variation of the surface sound speed at the face of the transducer, and
- (c) the time series of the roll during the survey,

one is able to model the surface sound speed artifact and to subtract it from the original soundings. An important fact, that needs to be reinforced, is that these artifacts are distinct from the ray-trace artifacts, in that they are motion-correlated. These motion-correlated

artifacts described in this chapter are not used in the final implementation of the refraction tool developed in this thesis.

The next chapter is devoted to the removal of sound speed refraction artifacts from data acquired using a multibeam echosounder.

## **CHAPTER 4 REMOVAL OF THE SOUND SPEED REFRACTION ARTIFACT**

### **4.1. INTRODUCTION**

This chapter is divided into two distinct parts.

The first part is devoted to the methods used to compensate for a known water mass. The acquisition of the sound speed is discussed. Then, we describe the reduction of the soundings with the sound speed in real-time and in a post-processing context. Finally, we explain how the application of the sound speed is realized, both at the transducer face and in the water column.

The second part describes the methods used to compensate for an unknown water mass. A brief review is provided of existing methods for removal of refraction artifacts that remain in the data after the sound speed reduction is achieved. These tools use different techniques to produce corrections to add to the sound speed profile acquired during the survey. The purpose of this review is to provide an awareness of the characteristics of the existing methods before introducing a new refraction processing tool using a different approach (Chapter 5).

#### 4.2. ACQUISITION OF THE DATA WITH A VELOCIMETER

The acquisition of a sound speed profile is accomplished by means of a velocimeter. Such a device is composed of two electro-acoustic transducers spaced a short known distance apart and a reflector; all three define a sound path of fixed length in the water. A pulse is transmitted by one of the transducers, reflected and received by the other transducer. The delay between transmission and reception is then calculated. The sound speed is determined by dividing the known distance by the time measured.

Another, more frequently used method, for obtaining the sound speed is to collect the conductivity, temperature and pressure to compute the actual sound speed. This method provides a better understanding of the medium than an isolated sound speed reading. During a cast, values are logged either at a fixed time interval (1 per second) or a fixed depth interval (1 per metre). A series of sound speed measurements versus depth is recorded as the device descends towards the bottom. This data is sent to a processing unit, which both stores the observations and applies them to the time/angle data acquired afterwards [Tolstoy, 1966], [Albers, 1972], [Mackenzie, 1971].



#### 4.3. REDUCTION OF THE SOUNDINGS

Once the sound speed profile has been acquired, it is used to calculate the arrival depth and radial distance and hence remove the refraction artifact, which degrades the quality of the soundings.

##### *4.3.1. At the transducer array face*

Precise monitoring of the sound speed at the face of the transducer is necessary to ensure that the direction of the steered beam is correctly computed. Refraction artifacts generated by an imperfect monitoring have been described in Chapter 3.

##### *4.3.2. Within the water column*

###### 4.3.2.1. Methodology

As seen in §3.2, the variation of sound speed with depth deflects the sound wave on its way towards the bottom. The methods used nowadays to compensate for this are:

- 1- to apply a SSP to each time/angle combination or

2- to use Look-Up Tables as a computationally more efficient approximation.

Certain assumptions are made; we assume that:

- the sound speed profile that we have is representative of the water column which is being surveyed (i.e. invariant with time and space within the area and the duration of the survey),

- the structure of the ocean is absolutely stratified, with no horizontal variation of any kind.

We consider only vertical variations in the sound speed,

- the ray-trace can be performed using the transducer mean depth and the heave deviations at transmit and receive are applied afterwards.

The profile is composed of a number of layers, for which the sound speed is supposed constant or linearly varying. Snell's law is applied between each constant sound speed layer or in a continuous way in the gradient layers.

A Look-Up Table (LUT) is a large floating-point number table whose axis are the beam orientation with respect to the local level and the transit time. There are two values in the LUT precalculated for a discrete series of angles and times. From the two axis values of beam orientation and transit time, (which are the fundamental outputs from the sonar) the depth and across track values are calculated using the appropriate sound speed profile. An inverse LUT, with the depth and across track values on the axis, provides the beam orientation and travel

time. As the LUT is only precalculated for discrete steps in angle (e.g.  $0.2^\circ$ ) and time ( $\sim 10$  ms) a 2D interpolation is performed [Hughes Clarke, 1999a].

#### 4.3.2.2. Use of SSPs in different situations

A few situations can be encountered during a hydrographic survey:

- **Use of an incorrect SSP:**

One has reduced the soundings with an incorrect SSP and has obtained later the “correct” SSP. In this case, if the transit time and angle have not been saved, two LUTs need to be built: one inverse (computed with the original SSP) and one direct (computed with the new SSP). The first one is used to get back to the beam orientation and transit time from the already reduced depth and across track. Then the new direct LUT is applied to get the correct depth and across track solutions. If the surface sound speed has changed, a new series of steered angles must be computed as well, before applying the new LUT.

- **Use of two SSPs before and after the survey:**

This is the most usual case in which one takes two SSPs, one before and one after the data acquisition of the day. It can be done at the same location or in different places. There are

three ways of utilising these SSPs: 1- one can use a temporal linear interpolation of the water column changes, 2- a spatial interpolation or 3- both temporal and spatial interpolations.

1- If a temporal interpolation is made, one is assuming that the water column structure is varying linearly with time. The supposition is that no front of temperature or salinity has been crossed. One way of proceed to such an interpolation is to apply the two refraction solutions for all the beams and to weight the depth/across track solution depending on the time of the selected ping.

2- For a spatial linear interpolation, one proceeds in the same manner but with the weighting of the pings according to the distance from the two SSPs locations. If more than two SSPs are used, the ping weighting will be more complicated: all the SSP stations must be taken into account.

3- in the third case, idealistic, both temporal and spatial interpolations are applied.

There are, however, drawbacks to methods based on interpolation schemes. In reality the different characteristics do not vary linearly in time or space and are far from the linear approximation. These methods do not give an accurate enough solution to refraction problem. The artifacts in the resulting solution can be more or less apparent, depending on the unknown errors inherent in the assumption. They are also very computationally demanding and the results are still wrong [Hughes Clarke, 1999a].

#### 4.4. REDUCTION OF THE SOUNDINGS IN POST-PROCESSING

There is a variety of methods that can be applied to the data in post processing.

##### 4.4.1. Relative Area Difference Method.

This method uses an approach different to the usual ray tracing computations; it uses the relative area difference ( $\epsilon_s$ ) between two SSPs (see Figure 33). This area difference is defined as follows:

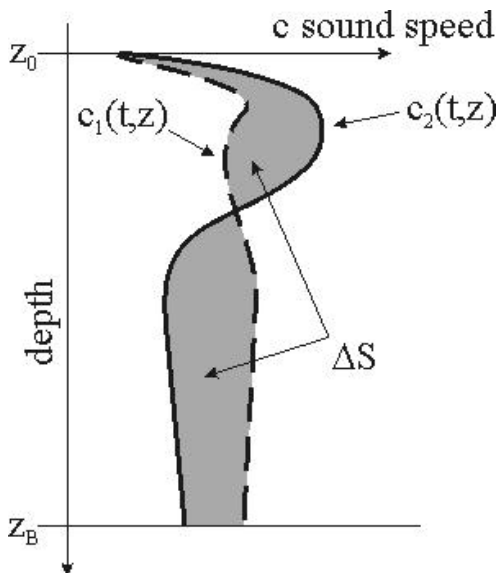


Figure 33: Definition of  $\Delta S$  difference of two sound speed profiles [Geng, 1998].

$$\text{Eq. 44} \quad \Delta S = \int_{z_0}^{z_b} dS = \int_{z_0}^{z_b} [c_1(t, z) - c_2(t, z)] dz$$

$$\text{Eq. 45} \quad \mathbf{e}_S = \frac{\Delta S}{\int_{z_0}^{z_b} c(t, z) dz} = \frac{\Delta S}{S}$$

In these formulas,  $c_1$  and  $c_2$  are the two SSPs considered,  $z_0$  is the depth of the transducer and  $z_b$  is the depth at which the beam hits the seafloor.

The method is based on the fact (shown in a different way in §6.3) that a family of sound speed profiles having the same initial sound speed  $c_0$  and the same area under their profiles ( $\mathbf{e}_S=0$ ) leads a ray to almost the same depth and across track values.

If one knows the actual SSP and chooses a very simple SSP model (e.g. a zero gradient function), one can compute the relative area difference  $\mathbf{e}_S$  between these two profiles.

One can establish two correcting functions (Eq. 46 and Eq. 47) which link the position given by the actual SSP (the unknown depth  $z$  and across track  $x$ ) to the position given by the SSP model chosen ( $z'$  and  $x'$ ). The values  $z'$  and  $x'$  are easily computed by triangulation methods. It can be shown that the functions  $f_z$  and  $f_x$  are almost entirely dependant on the relative area difference  $\mathbf{e}_S$  and the beam angle  $\mathbf{a}$ .

$$\text{Eq. 46} \quad \mathbf{e}_z = f_z(\mathbf{e}_s, \mathbf{a}) = \frac{z' - z_0}{z - z_0}$$

$$\text{Eq. 47} \quad \mathbf{e}_x = f_x(\mathbf{e}_s, \mathbf{a}) = \frac{x' - x_0}{x' - x}$$

Therefore by computing the relative area difference  $\varepsilon_s$ , between the actual SSP and a very simple constant SSP, one is able to compute much faster and with a similar accuracy to the ray tracing method, the depth and across track estimates [Geng, 1998].

#### 4.4.2. Equivalent Sound Speed Profile Method

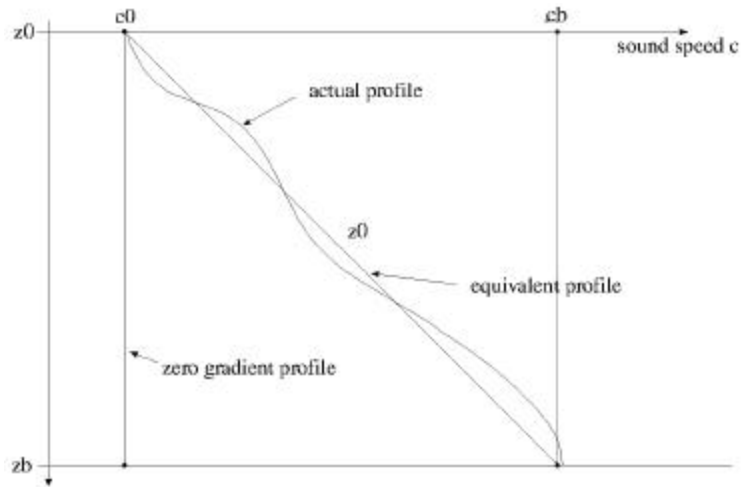


Figure 34: Search for an equivalent linear sound speed profile.

The equivalent sound speed profile method uses the same concept of relative area difference that has previously been described. An actual SSP can be a very complex curve and the aim of this method is to find the equivalent linear SSP giving the same depth and across track positions (see Figure 34).

Given a reference depth  $z_{b0}$  (e.g. depth coming from a single beam laser in the vertical direction in shallow water) and given a zero gradient profile (see Figure 34) that provides a depth estimate  $z'_b$ , the reference depth error is:

$$Eq. 48 \quad \mathbf{e}_z = \frac{z'_b - z_{b0}}{z_{b0}}$$

Knowing  $\mathbf{e}_z$ , the relative area difference  $\mathbf{e}_s$  between the equivalent profile and the zero gradient profile can be obtained by solving Eq. 46 for  $\mathbf{e}_s$ . It can also be expressed directly from Figure 34 by simple geometry (using the definition of  $\mathbf{e}_s$ , Eq. 44 and Eq. 45) as follows:

$$Eq. 49 \quad \mathbf{e}_s = \frac{c_b - c_0}{2c_0}$$

Eq. 49 can be solved for  $c_b$ . We use the expression obtained to compute the gradient  $g$  of the equivalent sound speed profile as follows:



Eq. 50

$$g_{eq} = \frac{c_b - c_0}{z_{b0} - z_0} = \frac{2\mathbf{e}_s c_0}{z_{b0} - z_0}$$

Once one knows the gradient of the equivalent SSP it is straightforward to compute the depth and across track and these values are almost the same as those from the actual SSP.

Having described the techniques of the application of the sound speed data to the multibeam soundings, we now focus on the methods used when the sound speed information is incorrect [Geng, 1998].

#### 4.5. REFRACTION ARTIFACT REMOVAL METHODS

##### 4.5.1. *OMG Refraction Tool*

A refraction-processing tool has been developed by the Ocean Mapping Group in order to minimize the refraction artifacts. This tool (described in Figure 35) allows the user to see the impact of a chosen one-layer SSP on the multibeam data. This model SSP is determined by

four different variables (transducer depth, surface sound speed, depth of the discontinuity layer and range of the discontinuity). This software allows the user to arbitrarily flatten the swath.

The user works along every survey line in steps of 80 profiles at a time. When he considers a set of profiles presents refraction artifacts, he sets up a series of four coefficients that brings these 80 profiles in the horizontal. These four coefficients are written down in a coefficient file with the corresponding ping number (referencing the location of the correction within the line). Then, when the line is gridded, a SSP correction is dynamically applied to each profile. This SSP correction is an interpolation of the two closest sets of refraction coefficients to either side of the profile, that were selected by the user.

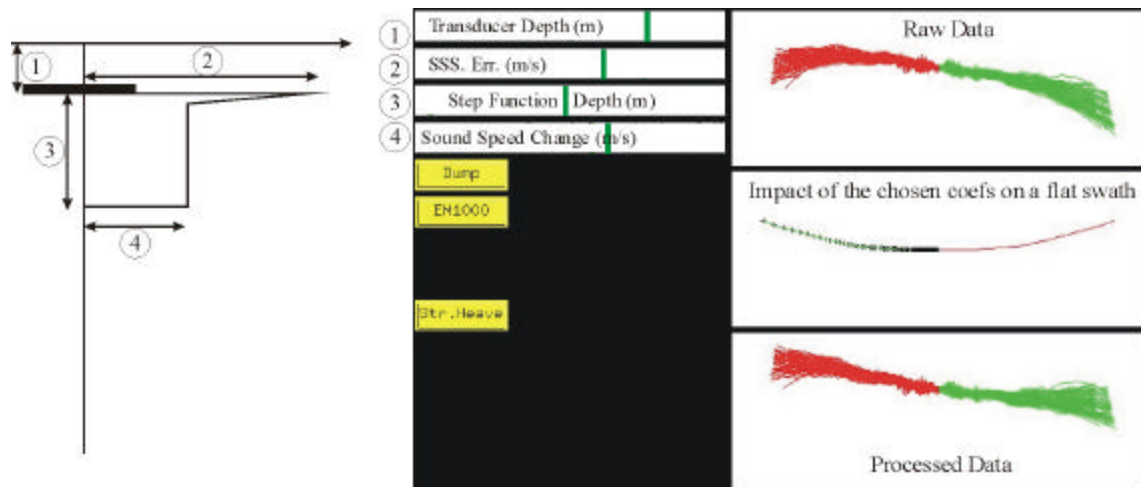


Figure 35: OMG Refraction tool main window.

This method does not take into account any other information, it is based solely on the shape of the 80 swaths considered at each time along the line. The shape of the swaths may include natural second order slopes that sometimes cannot be distinguished from refraction artifacts. It is then a “guess” that the individual user makes each time that he/she sets up a series of coefficients. However, this method gives good results in very flat terrain where the refraction artifact appears clearly in the data. An experienced operator can pass through large amounts of data looking for regions that are smooth and low backscatter. These types of seafloor are the most appropriate for empirical estimation [Hughes Clarke, 1999a].

#### *4.5.2. BatCor method*

The BatCor method is another tool for removing refraction artifacts in multibeam data that has been developed by the Ocean Mapping Group. This method uses a statistical approach; it determines corrections for each beam for a number of depth bins. It is composed in two parts; the first computes the needed corrections and the second actually applies them to the data. It goes through a series of steps that are described below (see Figure 36):

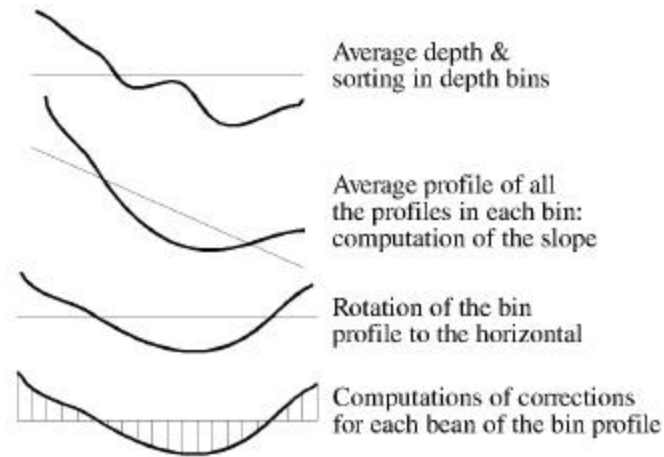


Figure 36: Methodology used by the software package BatCor [Dijkstra, 1999].

1- Determination of the average depth for each profile of the data set in order to allocate the profile to its corresponding depth bin.

2- Determination of the slopes of the average profiles from all the depth bins. These slopes are computed as the averages of the slopes between nadir and a number of points on each side of nadir.

3- Each profile is rotated in order to be horizontal. The natural slope of the seafloor is then removed.

4- Computation for each beam (of the average profile in each depth bin) of the differences between the average depth of the tilted profile and the tilted profile itself. Then all these corrections are translated in order to have a null difference at nadir (taken as a reference

almost unaffected by refraction). Finally, the differences are averaged between the same beam on both sides of nadir in order to make the correction of one profile symmetrical.

#### 5- Application of these corrections to the dataset.

This method gives good results when the number of profiles in each bin is large and when the refraction artifact is not varying within the stacking/averaging window. The average profile is then free of any natural morphology. An insufficient number of profiles introduces noise in the data. It needs also a small depth interval between the different bins because the corrections are not linear with depth. The corrections provided by this method induce a global depth error between the corrected and the original dataset. This trade-off and this depth error are the limitations of this method [Dijkstra, 1999].

#### 4.5.3. Method of the 45° beams

This method uses the beams emitted at  $\pm 45^\circ$  from the vertical to estimate the SSP errors. The main term of the proportional depth error  $dz$  versus beam angle  $q$  for errors  $dc$ , in the mean sound speed  $c$ , is given by the equation below:

Eq. 51 
$$\frac{dz}{z} = \left(1 - \tan^2(q)\right) \frac{dc}{c}$$

This equation is valid under the assumption that the surface sound speed is correctly known. From it, we learn that the beam angles  $\pm 45^\circ$  do not present any refraction errors. The quality of these beams is independent of any errors induced by the imprecision of the SSP used. This information can be used when survey lines cross each other. The tracks of the two beams at  $\pm 45^\circ$  and the vertical beam can be compared, (see Figure 37).

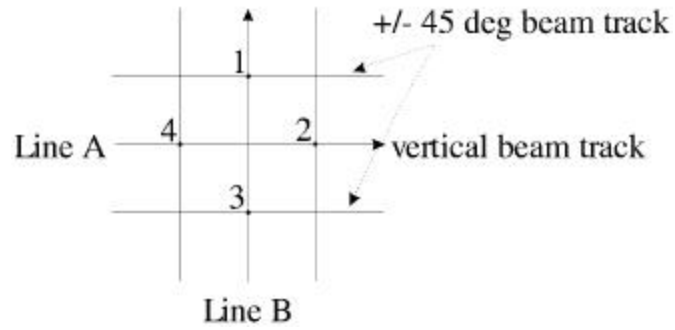


Figure 37: Schema of an intersection area showing the tracks of the  $\pm 45^\circ$  beam and the nadir beam.

From Eq. 51 we can write at intersections 1 and 2, the following relations:

$$\text{Eq. 52} \quad Z_{A1} = z_1 \quad \text{Eq. 53} \quad Z_{A2} = z_2 \left( 1 + \frac{dc_{A2}}{c_{A2}} \right)$$

$$\text{Eq. 54} \quad Z_{B1} = z_1 \left( 1 + \frac{dc_{B1}}{c_{B1}} \right) \quad \text{Eq. 55} \quad Z_{B2} = z_2$$

$Z_{A1}$  is the measured depth of the track A at the point 1,  $z_1$  is the true depth at the point 1,  $c_{A1}$  is the average sound speed in the water column of track A at point 1,  $dc_{A1}$  is the error in the average sound speed  $c_{A1}$ . Joining the equations above together we obtain the SSP corrections to be applied:

$$Eq. 56 \quad \frac{dc_{A2}}{c_{A2}} = Z_{A2} - Z_{B2}$$

$$Eq. 57 \quad \frac{dc_{B1}}{c_{B1}} = Z_{B1} - Z_{A1}$$

The same equations written for nodes 3 and 4 give an additional value for each sound speed correction. These values at nodes 1 and 3 and nodes 2 and 4 can be averaged. This method provides corrections of the averaged SSP, which are easy to compute at each intersection of two survey lines. However this method has the serious drawback of being based on the assumption that the surface sound speed is correctly known [Capell, 1999].

#### 4.6. CONCLUSION

All these methods have their specific drawbacks. With an insufficient knowledge of the water mass, the operator is faced with two choices: 1- to apply one of these approximations or 2- to reduce the swath width used. The next chapter presents a new method for removal of refraction artifacts.

## **CHAPTER 5 - GENERAL OVERVIEW OF REF\_CLEAN**

### **5.1. CASE OF THE SAGUENAY FJORD**

Information about the project on the Saguenay can be found in the following references: [Coté et al., 1999], [Kammerer et al., 1998], [Locat et al., 1999], [Locat et al., 1998].

The need for improved removal of refraction artifacts came up during the processing of two successive surveys (1993 and 1997) in the Saguenay River, (PQ, Canada). Between the two surveys, a catastrophic flood occurred and a huge quantity of material was eroded and brought into the fjord by several rivers in the area. The two data sets were processed and two Digital Terrain Models (DTMs) were created. In order to achieve a good description of the location and the amount of the deposits, the difference between these two DTMs has been calculated. This new DTM shows two main phenomena: 1- the real changes between the two years and 2- the artifacts from both surveys. Among all the different artifacts revealed the refraction was a dominant one. The artifact was pronounced due to the large time intervals between each sampling of the water column. Even after the application of the methods described in Chapter 4, fairly strong artifacts remain (see Figure 38). A new approach to the data processing was needed.



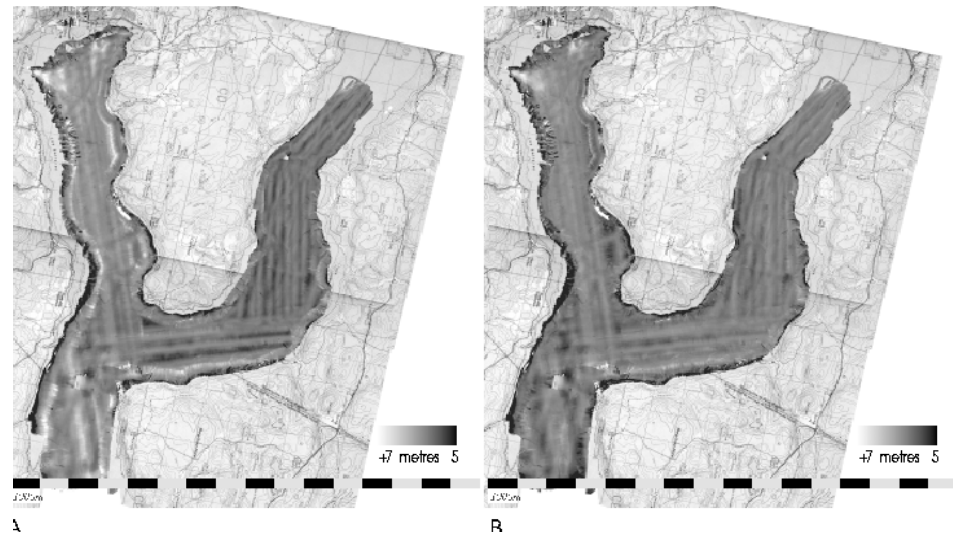


*Figure 38: Difference of the two DTMs. The stripes parallel to the ship tracks are artifacts, results of the application of an incorrect SSP. Right: refraction not processed; left: refraction processed, the artifacts are reduced but are still too high. [Kammerer et al., 1998].*

The new method described in this thesis provides better control over the refraction artifact in multibeam soundings. It is still an approximation, as the true water column remains unknown. It is based either on the adjustment of the SSPs already applied to the data, or alternatively, to the creation of a new SSP. An overview of the method is presented in the next section.

## 5.2. OVERVIEW OF THE METHOD

### 5.2.1. *General*

The characteristics of a water mass vary greatly in time and space; this makes it necessary for us to estimate local corrections within the survey area. As seen in the last chapters, refraction affects primarily the outer beams of the swath. The central beams (beams around nadir) are much less degraded. They can potentially be used as a reference for the true depth. The method described in this thesis uses the nadir part of every survey line to constrain the computation of SSP corrections. Survey lines can be compared to each other in two different ways: when three lines are parallel to each other (and overlap) and when two lines cross each other.

In the parallel case, an appropriate SSP correction would effectively merge the outer extremities of the middle line swath with the outer parts of the swaths of the neighbouring lines. The nadir depths of these lines on both sides can be used as an indication of the direction that the outer parts of the swaths should take after application of the SSP correction.

In the crossing case, the nadir part of the crossing line can be used as a reference. An appropriate SSP correction deforms the swath of the line crossed in such a way that it fits with the nadir of the crossing line.

### *5.2.2. First approach: adjustment of the existing SSP*

The first approach consists in computing SSP corrections to be added to the actual SSPs measured during the survey and already applied on the data. The depth and position data, provided by the sonar processing-unit, are used. Corrections are generated by using the nadir depths as reference and are then applied on this data.

### *5.2.3. Second approach: reconstitution of a new SSP*

In the second approach, things are considered in a different way. Instead of using the soundings on which a SSP has already been applied, the two way transit time and the beam angle are used to compute the synthetic SSP that best removes refraction artifacts. No prior ray tracing has been done on this data. A flat neutral SSP (with a sound speed of 1500m/s) is applied to the range and angle data. The heave of the vessel needs to be added to the depth obtained with the water column of 1500 m/s. This data is processed the same way as in the first approach.

### *5.2.4. Overview*

The proposed method is summarized in the flowchart of the Figure 39. The first approach (upper path in the flowchart) produces a SSP correction to be added and the second (lower path) produces a full SSP solution. This second approach is computationally heavier. However, it can provide some useful information about the equivalent water masses. The key part of the method is the SSP optimisation algorithm.

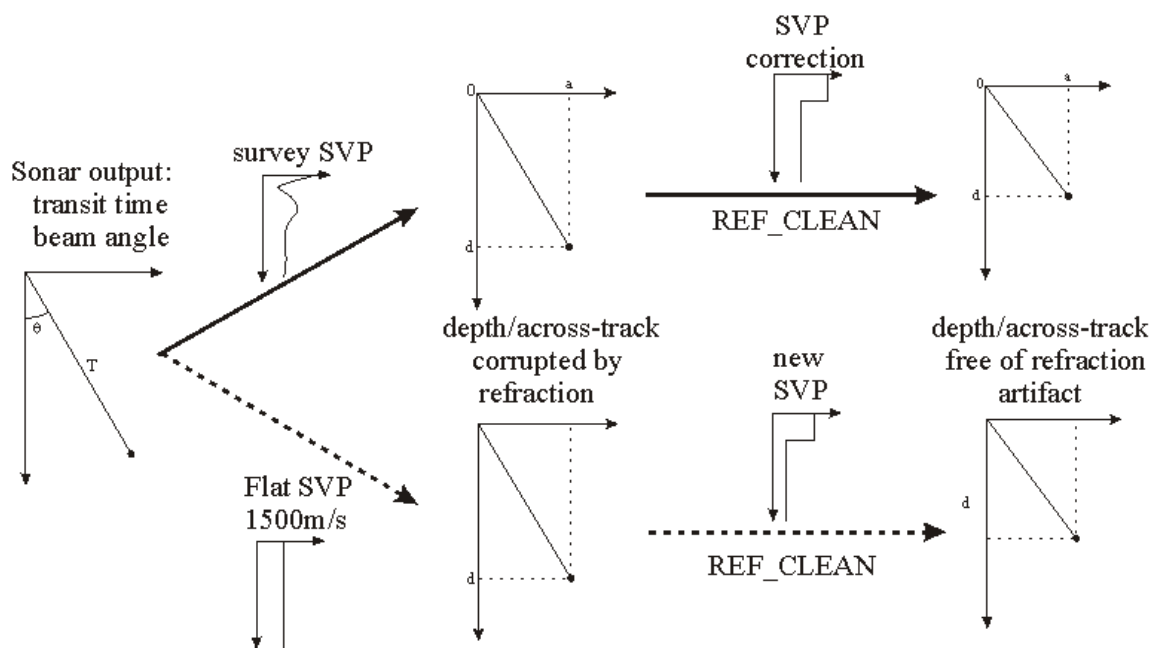


Figure 39: Flowchart showing the two processing methods proposed. The first approach is described with the plain arrows and the second approach with the dashed arrows.

Before the detailed description of the methodology proposed (Chapter 7) and its application to an actual dataset (Chapter 8), a few preliminary studies have to be considered in order to justify assumptions and choices used in the methodology. This is the matter of the following chapter.

## CHAPTER 6 - PRELIMINARY STUDIES

In this chapter, a series of studies are presented in order to justify assumptions and choices taken in method described and applied in the last chapters.

First, we look for the shape of a sound speed correction that will be added to the actual survey SSP, or that will replace the survey SSP. As seen earlier (see §2.2.1) the structure of a sound speed profile is usually very complex and changing in coastal water masses.

One stable feature common to all of these profiles is the presence of a highly variable seasonal thermocline below the surface layer. This thermocline is a negative gradient in temperature (so in sound speed) versus depth. The heat during the summer months strengthens the thermocline. The stormy weather of the winter tends to mix the water masses and reduce the importance of the thermocline.

As well as for the temperature, a halocline between the upper layers (low salinity) and the deeper layers (high salinity) takes place in the coastal water where there is much water runoff. The halocline is a strong positive gradient in salinity (i.e. a negative gradient in sound speed).

The shape of our SSP model will present this structure. In the first part of this chapter we compare a SSP model with a thermocline/halocline linearly varying with depth to a SSP model with a step thermocline/halocline. The second part examines which variables are sufficient and necessary so one and only one shape of refraction artifact corresponds to one SSP model that

has created it. The third and last part investigates how our SSP model can be applied on top of an already existing SSP.

### 6.1. INVERSE THEORY

Our approach takes place in the context of inverse theory [Menke, 1984]. An inverse problem consists of the extraction of physical characteristics of a natural medium from data that have been measured in this medium. The data available here are the multibeam soundings; the model parameters that are sought are the sound speed values of the water column. The model relates the parameters to the data. Here, the model is characterized by the fact that a correct SSP generates multibeam data free of refraction artifacts and by inference adjacent swaths should match within the overlap. The inverse problem leads from the estimation of the refraction errors in the multibeam data to the estimation of the corresponding errors in the sound speed distribution in the water column. A real SSP is a continuous function of the sound speed versus depth. A discrete approach is used here. The discrete model parameters will be represented by a finite number of numerical values. The SSP profile sought is represented by a finite number of sound speeds and depths.

## 6.2. CHOICE OF A SYNTHETIC SSP

### 6.2.1. Introduction

A SSP acquired in the field is a complex function of sound speed versus depth. We look for a correction that approximates the shape of a real SSP. The main stable characteristic of an actual SSP is the presence of a thermocline/halocline. Two local functions can be used to approximate the strong speed gradient corresponding to the thermocline in our SSP model: we have the choice between 1- a linear function (a gradient) and 2- a constant step function. The gradient function is a more realistic approximation of the SSP than the constant function. The aim of this section is to compare these two approximations and to select the most appropriate one.

### 6.2.2. Methodology

Being given a step SSP that brings a ray from an angle  $\mathbf{q}_1$  to an angle  $\mathbf{q}_2$  through a sound speed discontinuity at a certain depth  $z_s$ ; we look for a gradient SSP which brings the ray from  $\mathbf{q}_1$  to the same angle  $\mathbf{q}_2$  through a layer  $[z_1, z_2]$  of linearly varying sound speed. If there is one



we should be able to determine  $z_1$  and  $z_2$  from  $z_s$ , the gradient  $g$  and the two sound speeds  $c_1$  before and  $c_2$  after the change. Figure 40 shows how a step SSP and a gradient SSP can lead a ray in a similar way.

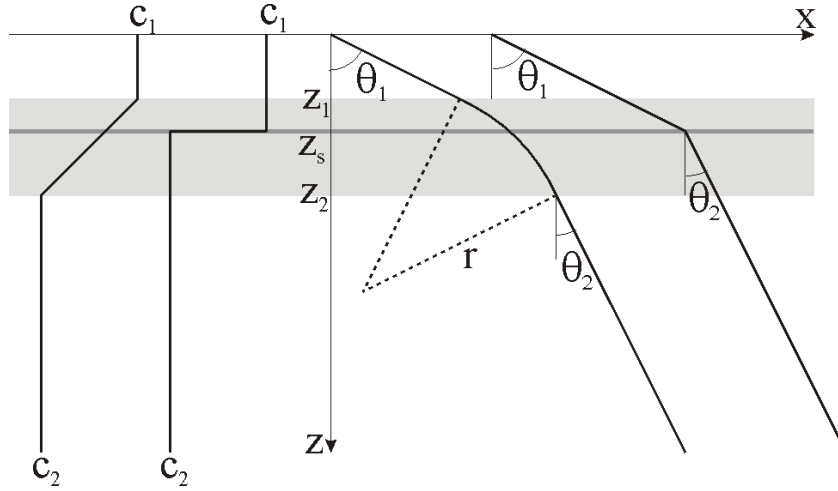


*Figure 40: Two equivalent synthetic SSPs and their effect on the propagation of a single beam. On the right the SSP has a step function at  $z_s$ , on the left a gradient function. The angles after the two speed changes are the same. The two SSPs bring the beam along the same path.*

After having found the gradient SSP, which brings a ray along the same path as the step SSP, we will consider the actual difference range between the two SSPs for the same depth. First, the methods used to apply these two SSPs on the flat seafloor are described.

### 6.2.3. Step SSP computation

The direct application of a step SSP on the data is as follows. As inputs, we have  $q_l$  and  $T$  the beam angle and travel time. The original across-track distance and depth of the beam are computed from these inputs. This is achieved with the assumption that the sound speed is  $1500 \text{ m.s}^{-1}$  ( $r = 1500 \times T$ ). The step SSP is composed by a first layer that goes from the surface to the depth  $z_s$  with a sound speed  $c_1$ , and the rest of the water column has a sound speed  $c_2$  (see Figure 41).

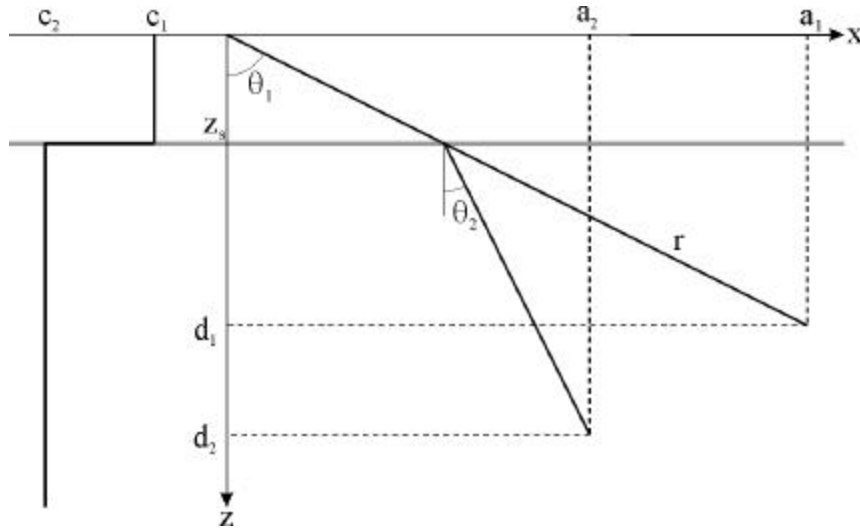


Figure 41: effect of a step SSP on a single ray, deviation of this ray from its original heading ( $c_1 > c_2$ ).

At the layer boundary ( $z=z_s$ ) Snell's law is written:

$$Eq. 58 \quad \mathbf{q}_2 = \text{Arcsin}\left(\frac{c_2}{c_1} \sin \mathbf{q}_1\right)$$

The corresponding range is equal to:

$$Eq. 59 \quad r = \sqrt{a_1^2 + d_1^2}$$

From the boundary  $z_s$  to the bottom with an orientation of  $\mathbf{q}_2$  at the surface, the signal has to travel the distance  $r_2$ :

$$Eq. 60 \quad r_2 = \left(\frac{r}{1500} - \frac{z_s}{c_1 \cos \mathbf{q}_1}\right)c_2$$

In this equation, it is assumed that the initial range  $r$  has been covered at the average sound speed of 1500 m/s. Finally the new depth and across-track distance are computed as follow:

$$Eq. 61 \quad d_2 = z_s + r_2 \cos \mathbf{q}_2$$

$$Eq. 62 \quad a_2 = z_s \tan \mathbf{q}_1 + r_2 \sin \mathbf{q}_2$$

#### 6.2.4. Gradient SSP computation

In this case, there is a sound speed gradient  $s$  between the depths  $z_1$  and  $z_2$  (see Figure 42).

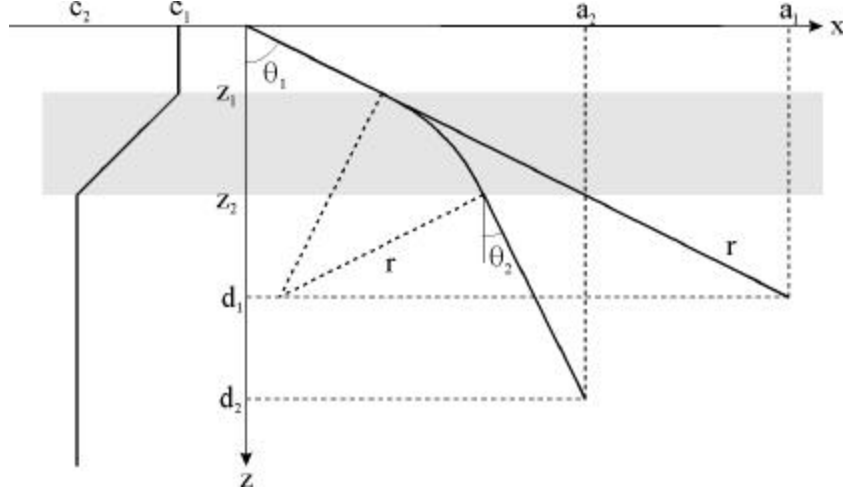


Figure 42: Ray path through a water column having a gradient in the variation of the sound speed versus depth.

Above  $z_1$  and below  $z_2$  the situation is the same as in the previous paragraph. In order to compute the depth and across-track changes through  $[z_1, z_2]$ , this layer is decomposed in  $N$  layers (the alternative method would be to use Eq. 23 to Eq. 29. For each layer, the calculations are done as follows:  $q_p$  and  $c_p$  are the angle and the sound speed at the entrance of the layer;  $q$  and  $c$  the angle and sound speed after the beam within the layer.  $j$  is the number of layers already crossed.

$$\text{Eq. 63} \quad \mathbf{q} = \arcsin\left(\frac{c_p}{c} \sin \mathbf{q}_p\right) \text{ and } c = c_1 - \frac{c_1 - c_2}{N} j$$

At the exit of a layer, the across-track range added is:

$$\text{Eq. 64} \quad \frac{z_2 - z_1}{N} \tan \mathbf{q}$$

The total time used to cross the layer is:

$$\text{Eq. 65} \quad \frac{z_2 - z_1}{N} \frac{1}{c \cos \mathbf{q}}$$

These computations are realized for each layer. The total across-track range and the distance traveled by the ray between depths  $z_1$  and  $z_2$  are computed. At the exit of the last layer, we compute the final depth and across-track by the same way as in §6.2.3 above. A large number of layers insures the validity of the approximation.

#### 6.2.5. Comparisons of the results and conclusion

If we have a closer look at the area where the ray is curved by the speed gradient and deflected by the sound speed discontinuity, we can see what is illustrated in Figure 43. The point C has the following property: the segments [AC] and [BC] are tangent to the circle of radius R so C (intersection of the two segments) is located at the bisecting line of the angle

AOB (O being the centre of the circle invisible on this figure). The distances from A to C and from C to B are then equal:  $d(A,C)=d(C,B)$ .

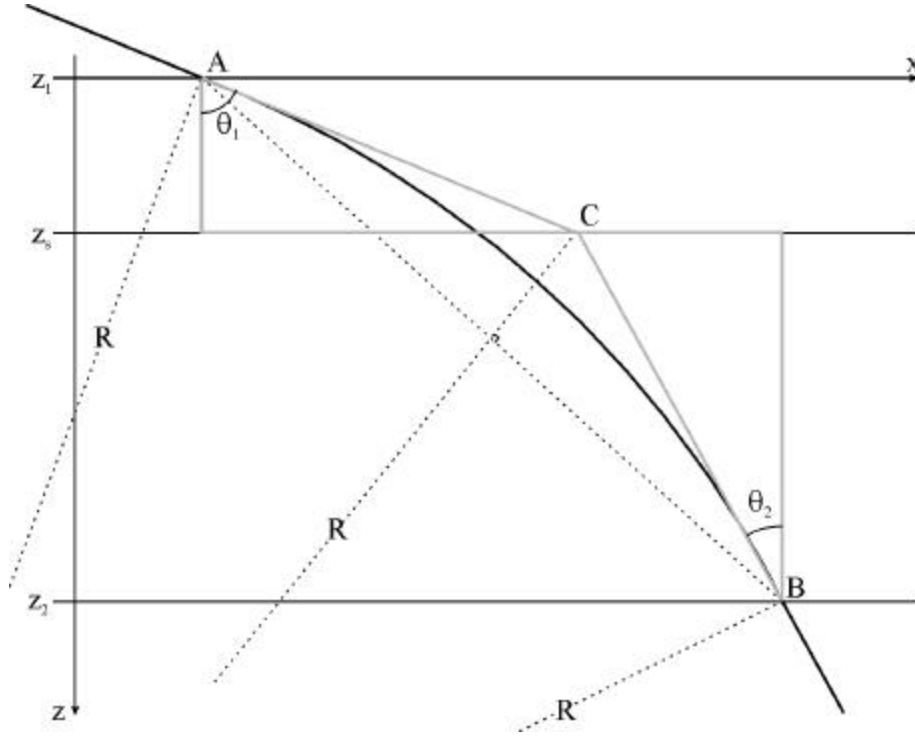


*Figure 43: Close-up on the area where the ray changes direction. It follows a curve AB in the case of a gradient SSP and follows the path ACB in the case of a step SSP.*

If we consider the two triangles (delimited by the gray lines on Figure 43) we can express the common relation:

$$Eq. 66 \quad d(A,C) = \frac{z_s - z_1}{\cos \mathbf{q}_1} = \frac{z_2 - z_s}{\cos \mathbf{q}_2} = d(C,B)$$

The known sound speed gradient is expressed by the following equation:

$$\text{Eq. 67} \quad c(z) = g(z - z_1) + c_1 \text{ with } g = \frac{c_2 - c_1}{z_2 - z_1}$$

Snell's law is applied between A and B and is written:

$$\text{Eq. 68} \quad \frac{c_1}{\cos \mathbf{q}_1} = \frac{c_2}{\cos \mathbf{q}_2}$$

From the expression of  $g$ , from the expression of Snell's law and from Eq. 66 we can express

$z_1$  and  $z_2$ :

$$\text{Eq. 69} \quad z_1 = z_s - \frac{c_1}{g} \left( \frac{c_2 - c_1}{c_2 + c_1} \right)$$

$$\text{Eq. 70} \quad z_2 = z_s + \frac{c_2}{g} \left( \frac{c_2 - c_1}{c_2 + c_1} \right)$$

We have then found  $z_1$  and  $z_2$  that define a gradient SSP. This gradient SSP brings a ray along an exact same path than a step SSP. We have to investigate now which range error is generated by the difference in speed from the two approaches.

Let us consider for a depth  $z_t$ , the transit times for the two SSPs to get **vertically** to  $z_t$ :

Step SSP:

$$\text{Eq. 71} \quad t_1 = \frac{z_s}{c_1} + \frac{z_t - z_s}{c_2}$$

Gradient SSP:

$$Eq. 72 \quad t_2 = \frac{z_1}{c_1} + \int_{z_1}^{z_2} \frac{dz}{c(z)} + \frac{z_t - z_2}{c_2} = \frac{z_1}{c_1} + \frac{1}{g} \ln \frac{c_1}{c_2} + \frac{z_t - z_2}{c_2}$$

The difference between  $t_1$  and  $t_2$  multiplied by  $c_2$  ( $|t_2 - t_1|c_2$ ) gives the range error between the two SSPs. This range error projected on the two axes gives the errors in depth and across track. This difference has been computed for different gradient values for a depth of  $z_t=100$  m, and is plotted in Figure 44. The amplitudes of the differences are proportional to  $10^{-4}$  m.

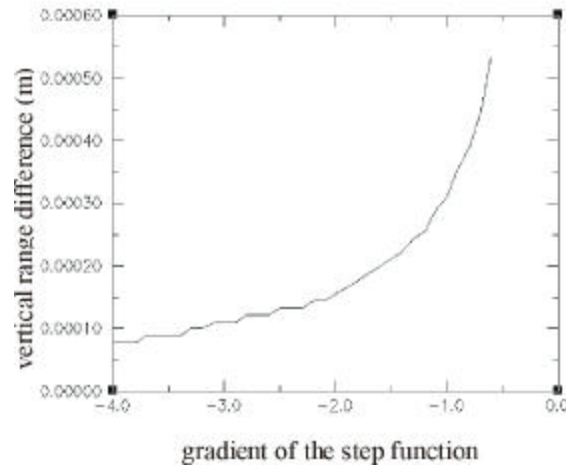


*Figure 44: Variation of vertical range difference between a step SSP and a gradient SSP for different values of gradient. The amplitude of these differences is  $10^{-4}$  for a total depth of 100 m.*

Consider now the transit times to get **obliquely** to  $z_t$ :



Step SSP:

$$Eq. 73 \quad t_1 = \frac{z_s}{c_1 \cos \mathbf{q}_1} + \frac{z_t - z_s}{c_2 \cos \mathbf{q}_2}$$

Gradient SSP:

$$Eq. 74 \quad t_2 = \frac{z_1}{c_1 \cos \mathbf{q}_1} + \sum_{z_i=z_1}^{z_2} \frac{dz}{c(z_i) \cos \mathbf{q}_i} + \frac{z_t - z_2}{c_2 \cos \mathbf{q}_2}$$

The reader can notice in Eq. 72 above that the layer of gradient speed has been decomposed in layers of thickness  $dz$ . The differences in oblique range between the two SSPs have been computed for a few discrete beam angles. These values are plotted on the graph in Figure 45. In the oblique case, the amplitudes of the differences are proportional to  $10^{-3}$ m.

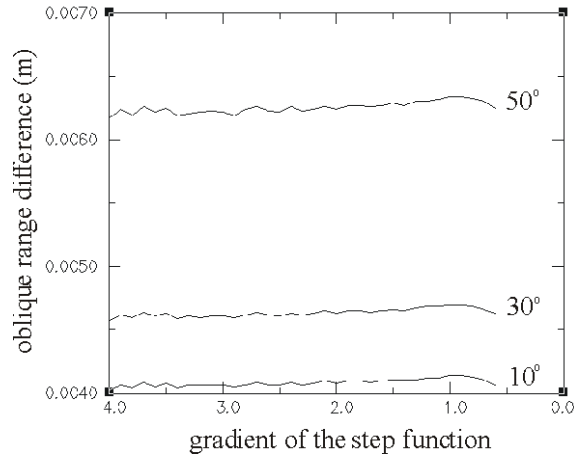


*Figure 45: Variations of oblique range differences between a step SSP and a gradient SSP for different propagation angles ( $10^\circ$ ,  $30^\circ$  and  $50^\circ$ ) for different values of gradient. The amplitude of these differences is in millimetres for a total depth of 100m.*

The conclusion is that the step SSP approximation and the gradient SSP approximation are roughly equivalent. Therefore, being much simpler to compute, the approximation of the thermocline/halocline as a step function was used henceforth.

### 6.3. VARIABLE REDUCTION

#### *6.3.1. Introduction*

The shape of the correction chosen in the previous paragraph is a two-layer step SSP as shown in Figure 46.

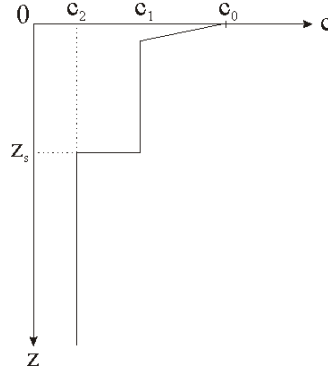


Figure 46: Example of a SSP with two layers. It is fully described by the four variables

$c_0$ ,  $c_1$ ,  $c_2$ , and  $z_s$ .

Such a profile is defined by the following four variables: the surface sound speed  $c_0$ ; the first layer sound speed  $c_1$ ; the second layer sound speed  $c_2$ ; and at last the depth of the sound speed discontinuity  $z_s$ .

This is the model used in the OMG Refraction Tool (see §4.5.1).

### 6.3.2. Case of $c_0$

The variable  $c_0$  corresponds to the sound speed error at the face of the transducer. We have studied the shape of the artifacts generated by this error (see §3.4). We have seen that the amplitude of these artifacts is periodic (because of a roll dependency).

It has been shown [Dinn, 1995] that for flat array transducers a sound speed discontinuity at the face of the transducer and at a certain depth in the water column generates the same kind of refraction artifact. In the case of flat array transducers, the variable  $c_0$  is useless and does not need to be considered. For other system configurations,  $c_0$  stays among the variables to be computed.

### 6.3.3. Case of $z_s$ , $c_1$ and $c_2$

We are looking for interdependence within the set of these three variables in order to simplify the search for the SSP correction. Figure 47 shows how two couples  $(c_1, c_2)$  for a fixed depth  $z_s$  and two couples  $(z_s, c_2)$  for a fixed speed  $c_1$  can bring a ray through two different paths to similar depth and across-track positions. These positions are not exactly equal because the SSP changes from one case to the other. We evaluate the amplitude of the position differences to estimate the validity of the interdependence between the variables.

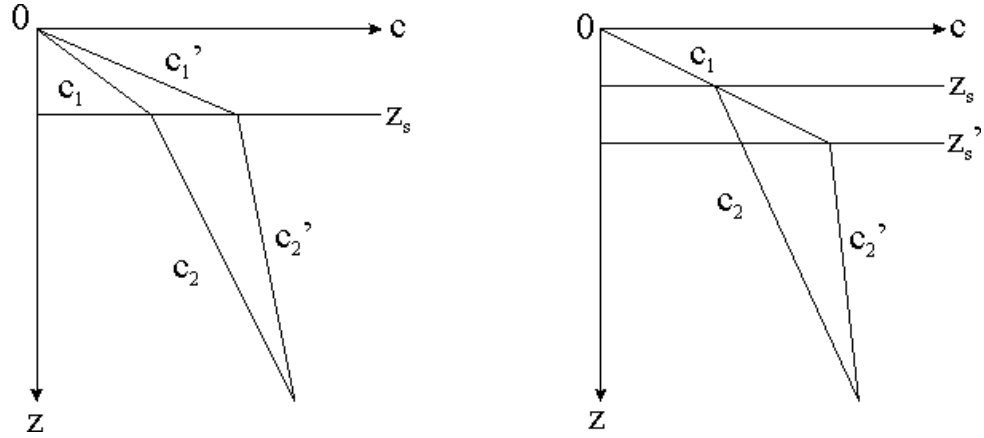


Figure 47: These two simple graphs show how two couples  $(c_1, c_2), (c_1', c_2')$  for a fixed depth  $z_s$  (on the left) and two couples  $(z_s, c_2), (z_s', c_2')$  for a fixed speed  $c_1$  (on the right) bring a ray through two different path at similar depth and across-track positions. This graph illustrates “non-uniqueness” of the inverse problem.

It is then justified to look for interdependence within these two couples of variables. In this paragraph, first the couple made by  $c_2$  and  $z_s$  is considered; then the couple  $c_1$  and  $c_2$  is analyzed.

#### 6.3.4. Methodology

##### Step #1:

We have three variables:  $z_s$ ,  $c_1$ , and  $c_2$  defining a sound speed profile. This dataset is applied on a synthetic flat seafloor and this generates a deformed swath. A parabola is fit to this deformed swath. The equation of the parabola can be written:

$$\text{Eq. 75} \quad y = a_0 x^2 + b_0$$

In this equation  $y$  is the depth and  $x$  the across-track position. The two coefficients  $a_0$  and  $b_0$  define a unique parabola. There is no term in  $x$  in Eq. 75 because the flat seafloor generates a symmetric refraction artifact and the parabola fitting this symmetric curve should have its minimum centred on the  $y$ -axis.

### **Step #2:**

Either  $c_1$  or  $z_s$  is kept constant; the other is changed to a different arbitrary value  $c_1'$  or  $z_s'$ . A minimisation algorithm (see Fibonacci algorithm §7.7) looks for the value of  $c_2$  that minimizes the difference between the two parabolas generated. This difference is the difference between  $a_0$  and  $a_1$  ( $a_1$  is the coefficient of the parabola fitting the new deformed swath). The equation of this second parabola is then:

$$\text{Eq. 76} \quad y = a_1 x^2 + b_1$$

The two parabolas fit very well to the deformed swath that they approximate. As can be seen in Figure 48, the absolute differences between the deformed swaths and their corresponding parabolas do not exceed 1 cm (for a 100 metres depth) for the outermost

beams. It is therefore justified to use these parabolas to compare the deformed swaths with each other.

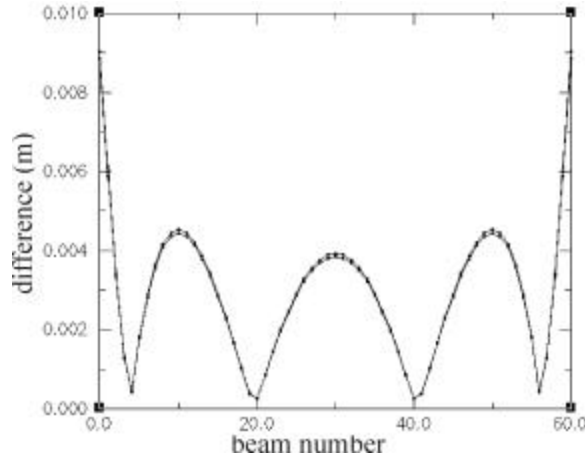


*Figure 48: Absolute difference by beam number between the swath resulting from the application of a two-layer SSP on a flat seafloor and its best-fitting parabola for  $c_1=1500$  m/s;  $c_2=1505$  m/s;  $z_s=10$  m and  $c_1'=1510$  m/s;  $c_2'=c_2$ ;  $z_s'=z_s$ .*

### **Step #3:**

The only difference between the two parabola equations is now a vertical offset (difference between  $b_0$  and  $b_1$ ). This offset can be visualized at nadir ( $x=0$ ). It represents the difference of the traveled distance due to the change of harmonic mean sound speed (see §2.2.3.1) in the water column. The travel time stays the same. In each case, its value can be computed in the three different cases (see Figure 49) as follows:

Eq. 77

$$\frac{r}{c} = \frac{z_s}{c_1} + \frac{x - z_s}{c_2} = \frac{z_s}{c_1'} + \frac{x' - z_s}{c_2'} = \frac{z_s'}{c_1} + \frac{x'' - z_s'}{c_2''}$$

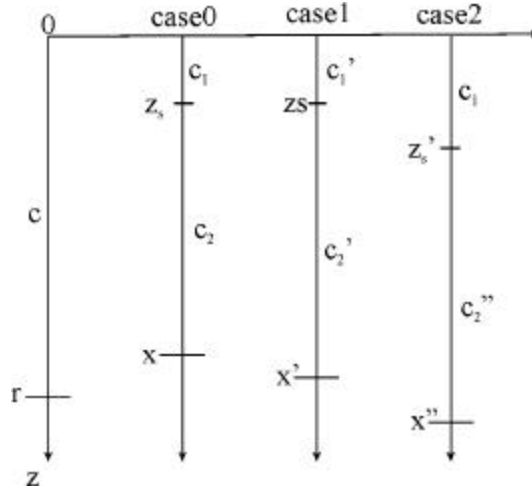


Figure 49: Variation of the traveled distance at nadir for the different cases. Case 0: appliance of the dataset ( $c_1$ ,  $c_2$  and  $z_s$ ) onto the flat seafloor. Case 1: estimation of  $c_2'$  for  $z_s$  constant and the new value  $c_1'$ . Case 2: estimation of  $c_2''$  for  $c_1$  constant and the new value  $z_s'$ .

The two swaths of case 1 and case 2 can be adjusted to the swath of case 0 (see Figure 50). The distances between the nadir of the two swaths and the nadir of the swath of case 0 can be written as follows:

Eq. 78

$$\Delta_1 = x' - x = \left( \frac{r}{c} - \frac{z_s}{c_1'} \right) c_2' + z_s - x$$



Eq. 79 
$$\Delta_2 = x'' - x = \left( \frac{r}{c} - \frac{z_s'}{c_1} \right) c_2' + z_s' - x$$

The distance  $x$  has the following value:

Eq. 80 
$$x = \left( \frac{r}{c} - \frac{z_s}{c_1} \right) c_2 + z_s$$

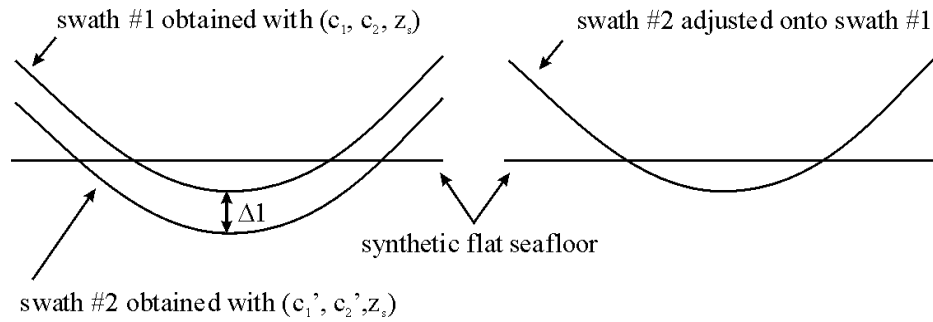


Figure 50: vertical adjustment of the two deformed swaths at nadir (on the left). Once adjusted (on the right) the two swaths match perfectly.

These corrections adjust exactly the two swaths #1 and #2 onto the original swath, in a way where the best-fitting parabolas are now the same (same  $x^2$  coefficient coming from the minimisation and same constant coefficient from the sound speed adjustment). Even if the two curves are perfectly overlaid, the positions of the soundings can be located differently on the same curve. It is not distinguishable unless we have a target in the area.

It has then been shown that with this correction added it is possible to generate the same best-fitting parabolas to the same deformed swath with two different couples of  $(c_1, c_2)$  or two different couples of  $(z_s, c_2)$ .

#### *6.3.5. Conclusion*

In the section 6.3 above, it has been proven that interdependence relationships exist within three of the four variables that define a two-layer SSP. The sound speed of the first layer  $c_1$  and the sound speed of the second layer  $c_2$  as well as the depth of the discontinuity  $z_s$  and the sound speed of the second layer  $c_2$  are interdependent. From the four variables only two ( $c_0$  and  $c_2$ ) are needed to have a unique SSP model that creates a unique refraction artifact.

#### 6.4. VALIDITY OF THE ADDITION OF A SYNTHETIC ONE-LAYER SSP CORRECTION

#### 6.4.1. Introduction

In this fourth section we compare the results of the successive applications of SSPs with the results of the application of a single SSP that is the sum of the SSPs applied previously. This is the method used in the OMG Refraction Tool (see §4.5.1). The purpose of this study is to see if one has to go back to the multibeam raw data free of any SSP application in order to modify a SSP already applied. If this can be justified to a reasonable degree of accuracy, a saving in computational time can be gained.

#### 6.4.2. Methodology

To achieve this, we consider again a synthetic flat seafloor (100 metres deep) and a real SSP taken during a multibeam survey. We want to add a correction to the SSP. This correction is a synthetic two-layer SSP. In this case, we use a 20 metres deep layer in which the sound speed is 1500 m/s; below this layer, the sound speed is 1520 m/s.

A numerical model has been developed in order to apply a real (multi-layer) SSP to multibeam data. This algorithm is included in the program file ***apply\_SSP***.

The methodology (see Figure 51) consists of the comparison of the results of the two following methods:

**1<sup>st</sup> method:** successive applications of the real SSP and of the synthetic two-layer SSP on the flat swath.

**2<sup>nd</sup> method:** application of the sum of the real SSP and the synthetic SSP on the flat swath.

#### *6.4.3. Results and Analysis*

The two graphs in Figure 51 look very similar. In this paragraph, we are going to compare them in more detail in order to estimate the validity of the equivalence of the two methods. The two graphs from Figure 51 above are subtracted from each other. The absolute values of the differences for each beam in depth and across-track are plotted in Figure 52.

Notice that for this extreme correction ( $20\text{ms}^{-1}$  added to the sound speed of the first 20 metres of the SSP), all the beams at a depth of 100 metres have an error amplitude below 10 centimetres (0.1% of the water depth). Only the last outer beams present differences over 5 centimetres. The average error in depth is 1.93 centimetres and in across track 2.76 centimetres.

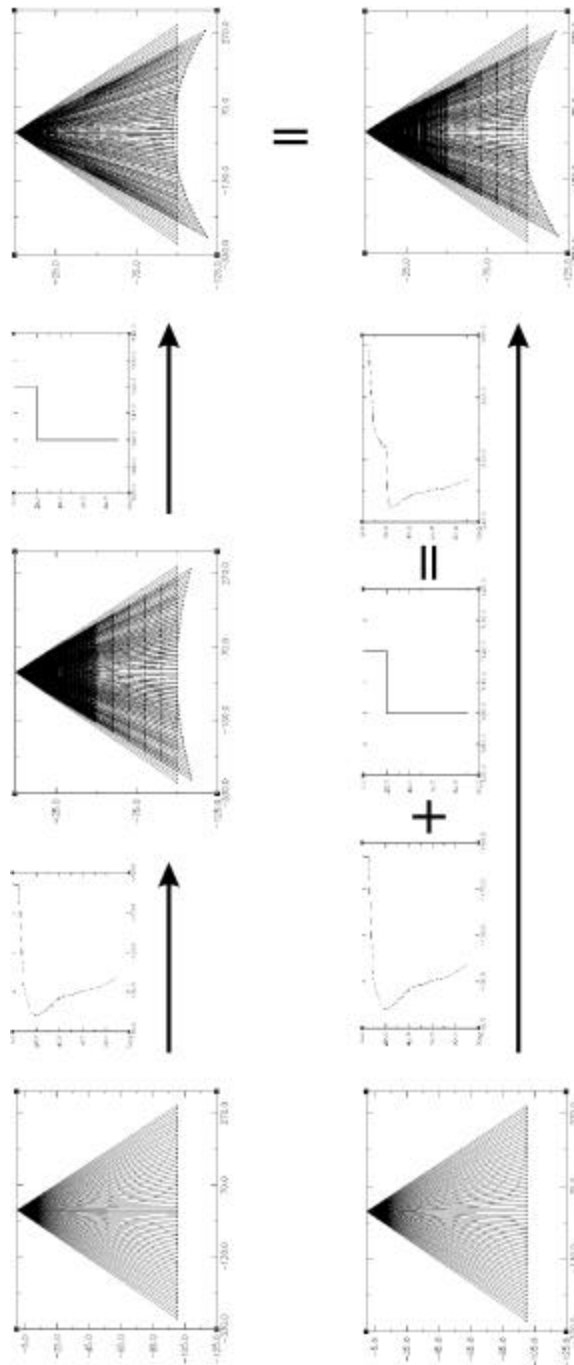


Figure 51: This schema compares the successive applications of a real SSP and of a synthetic one layer SSP to the application of the sum of these two SSPs on a 100 metres deep synthetic flat seafloor.

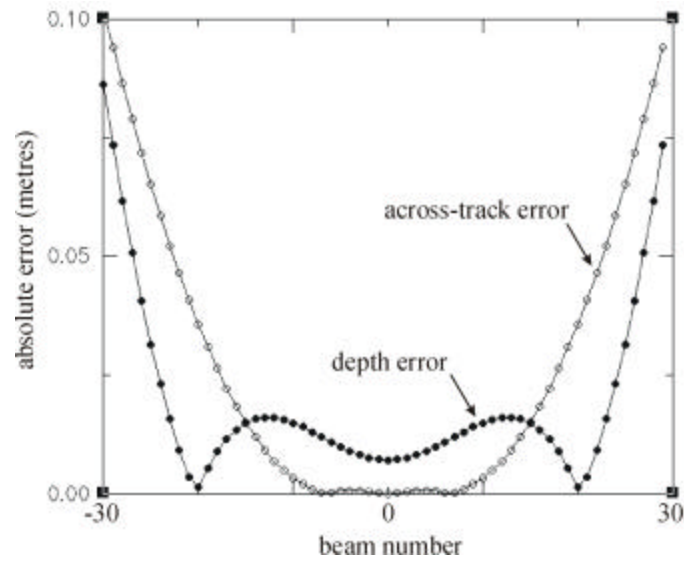
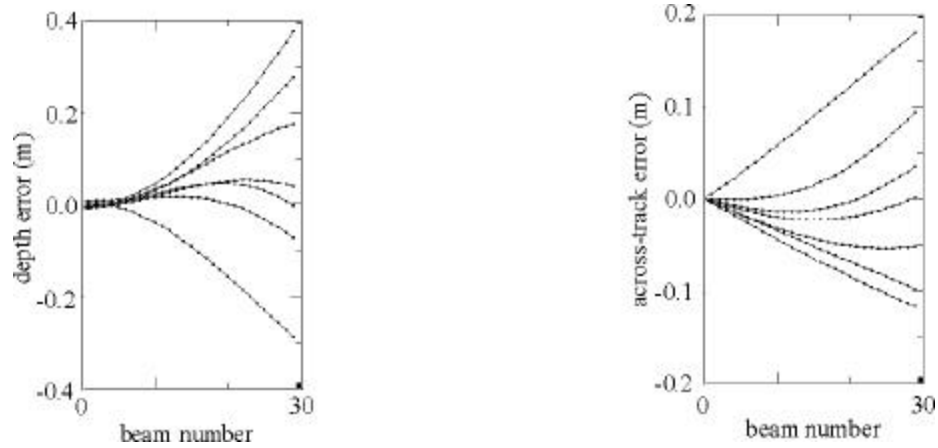


Figure 52: Absolute value of the differences between the graphs resulting from the two methods used above. The filled circles correspond to the difference in depth, the empty circles correspond to the across track difference.



*Figure 53: Differences for the 60 beams in depth (on the left) and across track (on the right) values of the graphs coming from the two methods compared in §6.4.2 for seven real SSPs.*

The method has been repeated with seven real SSPs from seven different hydrographic surveys in different geographic locations. The ranges between the graphs in depth and across track values have been computed and plotted in Figure 53.

The errors in depth which appear in Figure 53 are in amplitude less than 0.4% of the water depth for the total swath and less than 0.1% for the 30 central beams. The error in across track are even smaller: less than 0.2% of the water depth for the total swath and less than 0.1% for the 30 central beams. The average value in depth error is of 7 cm (0.0695 m). The average value in across track error is 4 cm (0.0385 m).

These results justify the appliance of synthetic two-layer SSP correction onto multibeam data on which a real SSP has been applied. This is especially true given that the correction is only an approximation of the likely change in  $c(z)$  anyway.

## 6.5. CONCLUSIONS

At the end of this chapter, three conclusions can be outlined. We were looking for the best SSP model that could be used as a correction to be added to a real SSP or to be equivalent to a real SSP. A real SSP usually has a complex structure. A stable feature that characterizes a SSP is the presence of a strong speed gradient (thermocline/halocline) at a certain depth below the surface waters. Our model contains this feature.

1- In the first section §6.2 we compared two different ways to model the strong speed gradient: a step function and a gradient function. The differences between these two SSPs being really small, we select the SSP that presents the simplest form for computational purposes: the step function SSP (also called two-layer SSP).

2- We have in §6.3 found two links between three of the four variables defining a two-layer SSP model. This leads us to the following conclusions. In order to cover all the different ways of how a flat seafloor can be distorted by a two-layer SSP, we can fix to a constant the depth of the discontinuity and the sound speed of the upper layer. Such a SSP model is defined only



with the deeper layer sound speed and the surface sound speed. The number of variables has been reduced from four to two.

3- In §6.4 we have proved that a synthetic two-layer SSP can be added to multibeam data on which a SSP has been previously applied without having to remove the SSP to add it to the two layer SSP correction before reapplying it.

By compiling the last three points, our SSP model will be a step function (point 1). It is defined by a variable surface sound speed, a sound speed discontinuity at an arbitrary depth, a constant sound speed in the upper layer, and a variable sound speed in the deeper layer (point 2). This correction can be applied to multibeam data having been already reduced by another SSP (point 3).

All these important results are justifications of methods used in the next chapter.

## CHAPTER 7 - METHODOLOGY

This chapter contains the proposed methodology for removing refraction artifact in multibeam soundings. First, the preliminary computations are described, and then the algorithms that compute refraction coefficients in the situation of parallel and crossing survey lines are explained. Finally, the limitations imposed by the roughness of the seafloor and the detrimental effect of the external errors in the soundings are clarified where they influence the application of the Ref\_Clean method.

### 7.1. PRELIMINARY COMPUTATIONS: EXTRACTION\_OMG

We use the multibeam processing tools developed by the Ocean Mapping Group (OMG). This software package SWATHED has its own data format [Hughes Clarke, 1999b]. The multibeam data must have already been processed with these tools when the application of Ref\_Clean can be considered (a step taken only if refraction artifacts are still apparent in the seafloor images). The first step to be done before the application of Ref\_Clean is the extraction of the specific data needed from the OMG processed files.

The program that achieves this is called *extraction\_OMG*. It creates, for each survey line, three ASCII files:

- 1- a bathymetry file (no extension) that contains for each beam latitude, longitude, depth, across track, two way transit time, vertically referenced beam depression angle and status (validity of the beam after data cleaning);
- 2- a navigation file (*nav* extension) that contains for each navigation point (each ping) latitude, longitude, heading and tidal value;
- 3- a boundary file (*bounds* extension) that contains the coordinates in latitude and longitude of the area in which the survey line is located (four values).

## 7.2. FIRST APPROACH: ADJUSTMENT OF THE EXISTING SSP

The purpose of this approach is to determine an additional SSP correction, which when applied on top of the data corrected using the original observed SSP, removes the residual refraction artifact as effectively as possible. As the water masses tend to vary significantly in space, we need to calculate local SSP corrections at different points along each of the survey lines. To achieve this, we apply artificial SSPs by using the preliminary studies realized in Chapter 6.

The beams around nadir of the survey lines are used as a reference to give an indication of the true bathymetric surface (they are much less degraded by refraction than the outer beams see §2.2.3.1). The method uses the information from two parallel lines and from crossing lines to constrain the shape of the swath of the central line. The shape of the swath free of refraction artifact should be the one that best aligns with the nadir depths of other surrounding lines. This approach determines the iterative SSP correction that best aligns the swath of the studied line with the nadir values of the two neighbours or of the crossing line.

### 7.3. SECOND APPROACH: PRELIMINARY COMPUTATIONS

As mentioned earlier (see §5.2.3), in the second approach, instead of using the depth and across-track data computed with the measured sound speed of the area, we use now the original transit time of the acoustic signal and the angle of the received beam. The idea is to generate synthetic two-layer SSPs that are not only corrections but also data with an intrinsic physical meaning.

Bearing in mind the equivalence of many water columns (see §6.2 and §6.3), these SSPs describe the essential character of the water mass (the thermocline/halocline). Using the first

approach, only iterative correctors are used and thus depend on the original SSP already applied.

Since the method needs depth and across-track values in input, we need to convert the time and angle data into depth and across-track. A sound speed value describing a homogeneous neutral water column needs to be chosen to actually perform this computation. The value of 1500 m/s has been chosen, as it is the global average sound speed value throughout the oceans.

Another value could have been chosen; for example, a global average of the velocities measured in the few SSPs taken during the survey. This value is an average of the local water mass for the area and the time of the survey. The amplitude of the coefficients computed would be smaller by using the local average of the water mass than the more global average 1500m/s. The final results would not change. The important point is to have a common reference for all the corrections.

The heave affecting the ship needs to be subtracted from the depth.

The simple computations are done as the two equations below show it:

*Eq. 81* 
$$d = 1500\Delta t \cos(\mathbf{q}) + h$$

Eq. 82 
$$a = 1500\Delta t \sin(\mathbf{q})$$

where  $d$  is the depth,  $a$  the across-track value,  $\Delta t$  the transit travel time,  $\mathbf{q}$  the beam angle and  $h$  the heave value.

The heave  $h$  is the component recorded at the time of transmit. It is not the average of the heave at transmit and at receive as it is done in rigorous ways. It does not really matter for the high ping rate that is used in shallow water areas as it is the case in the example seen later.

After these fast computations, the rest of the methodology is the same as that for the first approach. The difference lies in the actual meaning of the corrections computed. The results of the second approach are the corrections needed if the water masses had previously been a fictitious homogeneous average value of 1500 m/s. Therefore, these corrections have some connections with the actual physical sound speed distribution through out the area. They can be compared with each other because they have been computed on top of a same reference.

The program called *depth\_to\_twttOMG* converts an OMG processed file in which the depth and across-track values have been reduced with the actual SSPs into a similar OMG

data file. In this OMG file the depth and across-track values are computed directly from the transit time and beam angle as described in Eq. 81 and Eq. 82.

#### 7.4. METHODOLOGY: CASE OF PARALLEL LINES.

##### *7.4.1. Overview*

The first step of the method is to decompose the data in small datasets. The second step consists of the adjustment of the average swath of each of these small datasets and the computation of the optimal refraction coefficients defining the SSP to be applied.

##### *7.4.2. First step: decomposition of the survey line in small datasets*

The program called *para1\_find* does this part. When the option *-twttba* is added on the command line, the program uses equivalent depth and across values based on the transit time, beam angle and a 1500 m/s SSP (see §7.3) instead of the depth and across-track data.

*para1\_find* receives in input the three ASCII files created by *extraction\_OMG* (see above §7.1) for each of three parallel survey lines (9 input files in total). The purpose of the decomposition is to break down the three lines in a series of blocks of equal length.

Each block contains three segments of line coming from the three lines considered. For each segment of the middle line, two segments are associated on either side of the two parallel survey lines. These two segments are of equal length and similar heading on both sides of the middle segment being analyzed.

To achieve this, we project the navigation of the three lines on an imaginary straight line aligned along the average of the headings of the three lines, see Figure 54.

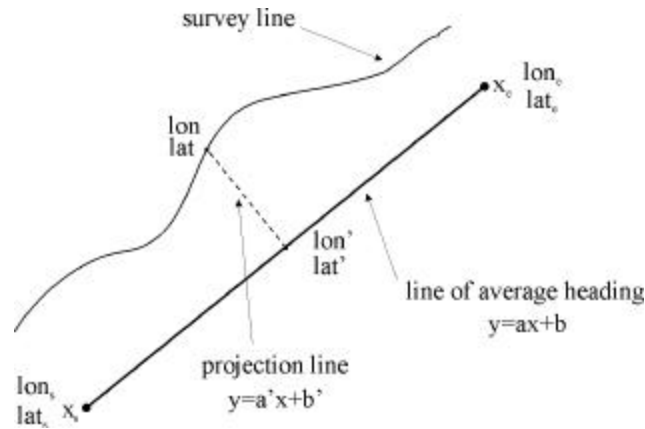


*Figure 54: Schema of the projection of the navigation data points from the three parallel lines onto a reference line oriented along the average of the three headings of the survey lines.*



The coordinates of the navigation point on the reference line are computed as follows. The equation of the reference line is:

$$\text{Eq. 83} \quad y = ax + b \text{ with}$$

$a$  and  $b$  are computed as follows:

$$\text{Eq. 84} \quad a = \frac{lat_e - lat_s}{lon_e - lon_s} \text{ and}$$

$$\text{Eq. 85} \quad b = lat_s - lon_s \left( \frac{lat_e - lat_s}{lon_e - lon_s} \right)$$

The equation of the projection line orthogonal to the reference line is:

$$\text{Eq. 86} \quad y = a'x + b' \text{ with}$$

$$\text{Eq. 87} \quad a' = \tan(\arctan(a) + 90^\circ) \quad (\text{orthogonal to } y = ax + b) \text{ and}$$

$$\text{Eq. 88} \quad b' = lat - a'.lon \quad (\text{the line contains the navigation point } (lon, lat))$$

The solutions of the linear system composed by the two equations (Eq. 83 and Eq. 86) are the coordinates of the projected point  $(lat', lon')$ .

We select an area where this straight line has a neighbour line on both sides. The two black dots in Figure 55 are the ends of the selected area. The line is then cut in a certain number of segments of equal length, which is chosen by the operator depending on how dense he/she wishes the geographic distribution of the corrections to be. These segments are our working areas.

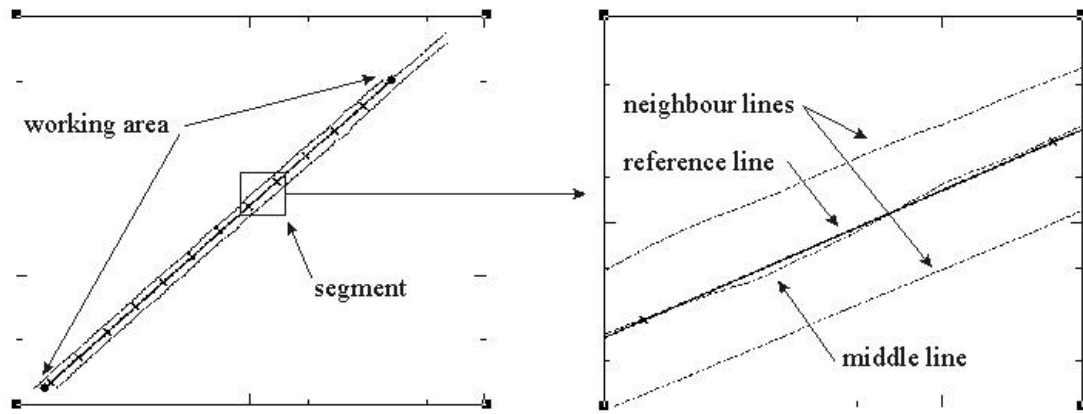


*Figure 55: The figure on the left is the global view of the three survey lines, the common segment and its partition in segments. The right figure is a close-up view on one of these sub segments.*

From the data of each segment are extracted the following values:

- The ping number in the middle of the segment for each line,
- The average nadir depth for each line,  $a_1, a_2, a_3$ ,
- The average tide for each line,  $t_1, t_2, t_3$ ,

- The latitude and longitude of the centre of the segment for the middle line
- The average distance between the navigation of each lines,  $d_{12}$ ,  $d_{23}$ ,
- The 60 average across track and depth values for the middle line,  $acc[0, \dots, 59]$ ,  $dep[0, \dots, 59]$ .

The data listed above is stored in the file *infoswath* used for the second step. Another output file is created, called *infoline*. The number of segments computed, the names of the lines being processed and the total number of pings in each line are stored in *infoline*.

#### 7.4.3. Second step: adjustment of the average swath:

The program called *para2\_adjust* does the adjustment of the average swath. From the data computed in the previous paragraph (§7.4.2), we proceed now to the evaluation of the SSP that brings the average swath as close as possible to the segments of line shown in Figure 56. This is done individually for each subsection of the survey line studied.

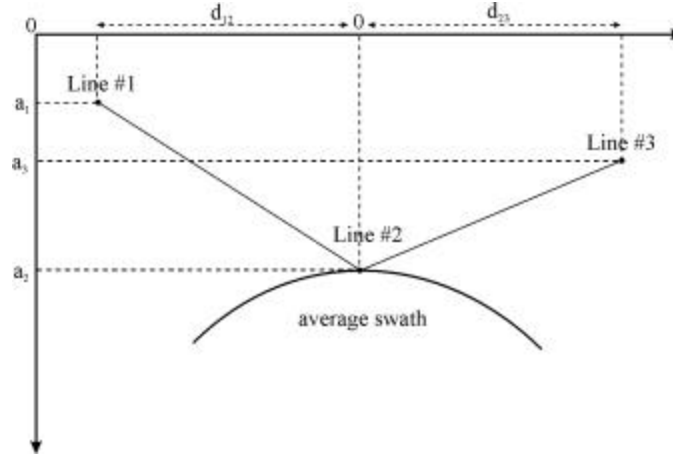


Figure 56: Relative position of the different lines in a cross section of each segment.

First method above: the swath is adjusted to the nadir depth of line #2.

The first step is to reduce the average nadir depths of each line with the tide coefficients computed above:  $a_1' = a_1 + t_1$ ,  $a_2' = a_2 + t_2$ ,  $a_3' = a_3 + t_3$

The sixty beams of the average swath of the middle line are then shifted vertically in order to have at the same depth the average nadir depth and the average of the twenty central beams.

$$Eq. 89 \quad Depth'[i] = Depth[i] + a_2 - \frac{1}{20} \sum_{i=21}^{40} Depth[i]$$

At this point, the optimisation of the refraction coefficients can now be carried out. The function  $f(c_0, c_2)$  (to be minimized) used in the search of coefficients  $c_0$  and  $c_2$  (see §7.7) is the sum of the squares of the vertical differences between the average swath depth of the middle line and the segments joining the nadir of the neighbour lines. We assume here that the seafloor is varying linearly from one average nadir depth to the other. The quality of this approximation

depends on the line spacing used as well as on the width of the swath. When the width of the swath is larger than twice the line spacing it is better to use the second closest parallel lines instead of the first.

Eq. 90 
$$f(c_0, c_2) = \sum_{i=1}^N (a \text{Across}(i) + b - \text{Depth}(i))^2$$

where  $\text{Across}(i)$  and  $\text{Depth}(i)$  are computed with the model SSP defined by  $c_0$  and  $c_2$ ;  $a$  and  $b$  are the coefficients of the line that joins the average nadir depths;  $N$  is the number of beams of a swath.

## 7.5. METHODOLOGY: CASE OF CROSSING CHECK-LINES.

### 7.5.1. Overview

The idea developed in the case of crossing lines is to use the nadir beams of the check-line. It is used as a reference for the true shape of the seafloor in order to estimate the refraction coefficients that best bring the average shape of the swaths of the line being analyzed as close as possible to the reference profile. It is done in three steps: the localization of the intersection

between the two lines, the setup of the two profiles to be compared and finally the actual optimisation of the refraction coefficients.

#### *7.5.2. First step: localization of the crossing point.*

The algorithm *cross1\_find* is designed to determine the geographical coordinates and the ping numbers of the crossing point between the survey line and the crossing check-line. As with *para1\_find* (see §7.4.2) when the option *-twttba* is added on the command line, *cross1\_find* recalculates the depth and across-track distance based on the transit time and beam angle and a 1500 m/s SSP (see §7.3) instead of the original depth and across-track data.

First, by using the boundary files it determines if the two boundary boxes overlap. If they do intersect and if the difference in heading between the two crossing lines is large enough (we are looking for an intersection angle within  $\pm 30^\circ$  from the orthogonal), the program reads the navigation files and looks for an intersection point between them. In order to do this, it looks for the minimum distance between the middle of segments constituted by two navigation points of each line (see Figure 57). If this minimum is lower than a fixed threshold (relative to the ping rate), the lines intersect. The two ping numbers (for the two lines) of this intersection point are given by the navigation points which correspond to the minimum distance below the threshold. The exact location of this intersection is then determined by computing the equations of two

straight lines passing through the four navigation points of the two segments corresponding to the minimum distance (see Figure 57). This latitude and longitude are stored in a file called *crossingfile1file2* with the names of the lines and the ping numbers corresponding to the intersection.

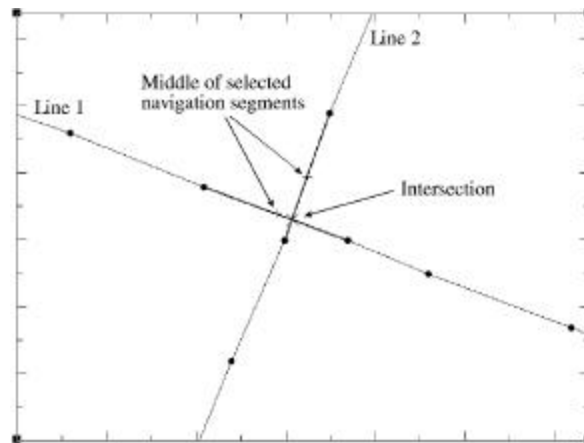


Figure 57: Schema of an intersection between two survey lines.

### 7.5.3. Second step: selection of the data to compare.

This second step is realized by the program *cross2\_grid*.

#### 7.5.3.1. Selection of the data from the survey line

From the survey line we select a certain number of profiles (all the pings that lie within the intersecting swath, 200 for example) on each side of the intersection location determined in the first step. These profiles are averaged in latitude, longitude, across-track, depth and average

azimuth. This average profile is our information about the survey line in the area. The averaging tends to weaken the influence of real features on the seafloor and to keep only the refraction artifact and the natural slope. Figure 58 shows profiles selected from the survey line on both sides of an intersection point.

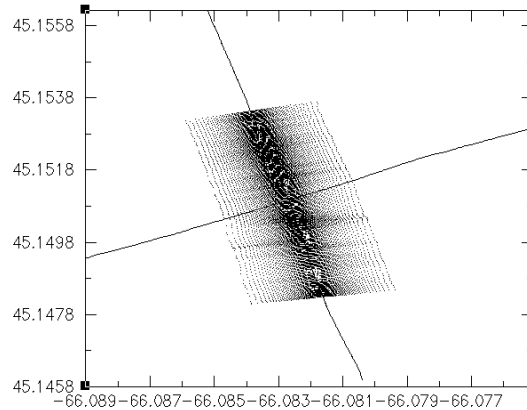


*Figure 58: Selection of 200 profiles from the survey line on both sides of the intersection point with a check-line.*

#### 7.5.3.2. Selection from the check-line

From the check-line we are only interested in the nadir part. In order to avoid the influence of spikes (penetration and amplitude/phase transition area noise, see external errors in §7.9.4) and real features on the sea bottom, the data (latitude, longitude, across-track, depth) from the 10 central beams of a certain number (200) of swaths are averaged out. Figure 59 shows the



average of the 10 beams around nadir selected from the check-line on both side of the intersection point.

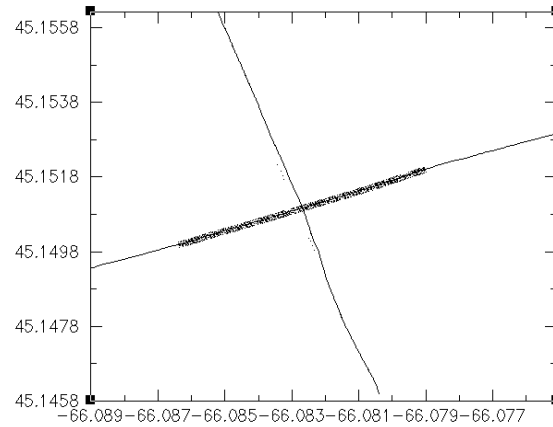


*Figure 59: Selection of the 10 beams around the nadir of the check-line.*

At the end of this first step we have two average profiles, which are geographically located as shown on the Figure 60.

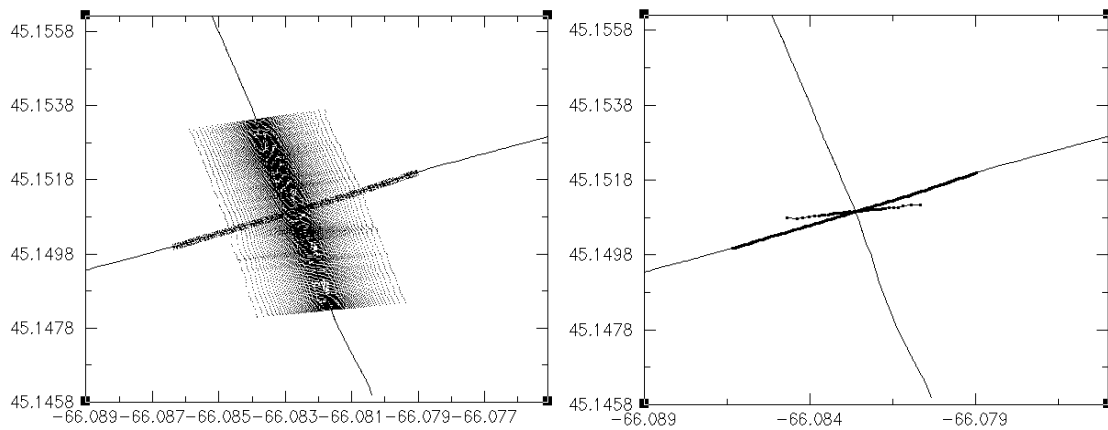
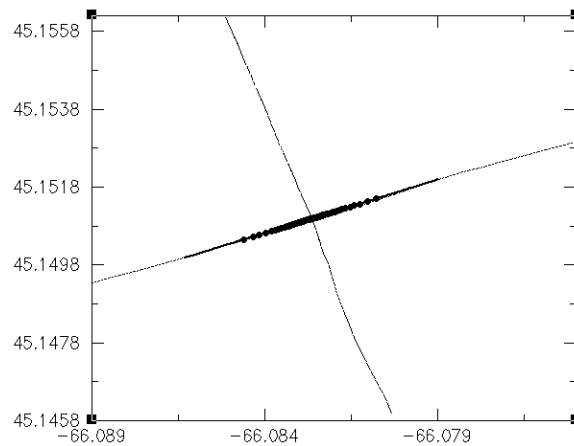


Figure 60: Left: view of the two selections made from the two crossing lines. Right: average profiles of the 200 swaths of the survey line and the 10 central beams of the check-line.

#### 7.5.3.3. Projection of the two selections on a common straight line

In order to be compared, these two profiles are both projected on a reference straight line defined by the average heading of the 200 pings selected out of the check-line and which goes through the intersection point. This is done to preserve as much as possible the shape of the average profile of the survey line from which refraction coefficients will be computed. Figure 61 shows the superposition of the two average profiles on the reference straight line. The results of these projections are stored at the end of the output file (called ***crossinglineNlineM***) of ***cross1\_find***.



*Figure 61: The two average profiles have been projected on the straight line defined by the average heading of the check-line and passing by the intersection point.*

#### *7.5.4. Third step: comparison of the two average profiles.*

This step is realized by the program ***cross3\_adjust***.

##### *7.5.4.1. Resampling of the survey line average profile:*

Having averaged 200 swaths from the survey line, we now have a profile of 60 beams (in the case of a Simrad EM1000). We averaged 10 central beams from 200 swaths of the crossing line, from which we generated another profile but this time of 200 points. In order to compare these two datasets we resample the points from the crossing line (200 points) onto the equivalent positions of the beams of the survey line profile (60 points). The profile of the crossing line obtained is shifted vertically so that the average of its nadir beams is at the depth of the other profile (the amount of this shift corresponds to the average vertical error present in the dataset see §7.9 for external errors). If we plot the profile obtained with the survey line profile we obtain the following graph:

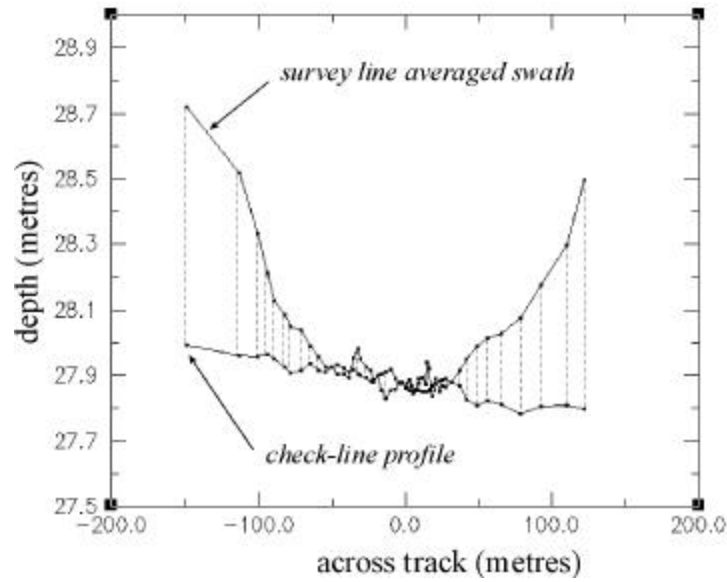


*Figure 62: Superposition of the profile from the survey line (the curved profile) with the gridded profile from the crossing line.*

#### 7.5.4.2. Computation of the trend of the crossing line profile:

The trend of the nadir profile of the crossing line is computed and plotted in the Figure 63.

We are now ready to proceed to the evaluation of the two-layer SSP which brings the average swath onto the trend of the crossing line profile.

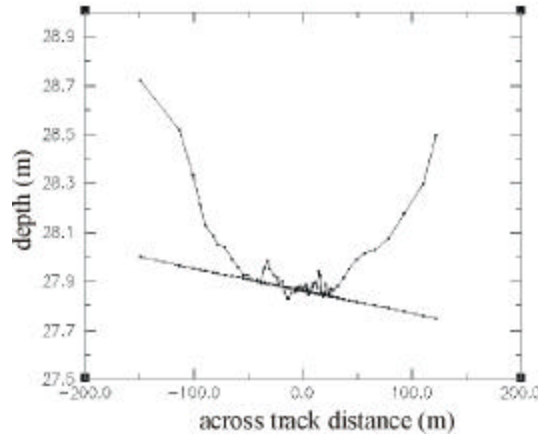


*Figure 63: Comparison between the trend of the crossing line profile and the survey line average swath.*

#### 7.5.4.3. Computation of the refraction coefficients

The search algorithm is described in the following paragraph §7.7. The coefficients of the two-layer SSP (surface sound speed and sound speeds of the second layer) are computed in order to minimize the distance between the two profiles. The criterion used in the search of the refraction coefficients is the sum of the squares of the vertical differences between the survey line average swath and the trend of the crossing line profile (same as Eq. 90).

Eq. 91 
$$f(c_0, c_2) = \sum_{i=1}^N (a \text{Across}(i) + b - \text{Depth}(i))^2$$

$\text{Across}(i)$  and  $\text{Depth}(i)$  are computed with the model SSP defined by  $c_0$  and  $c_2$ .

$a$  and  $b$  are the coefficients of the trend of the nadir profile of the check-line

$N$  is the number of beams of a swath.

This brings the average swath of the survey line as close as possible to the trend of the crossing line profile. The plot in Figure 64 illustrates this. Notice in this picture that there is a slight roll bias between the deformed swath and the trend of the crossing line. As we will see later (see External Errors in §7.9) the refraction tool is made inefficient by a large roll bias.

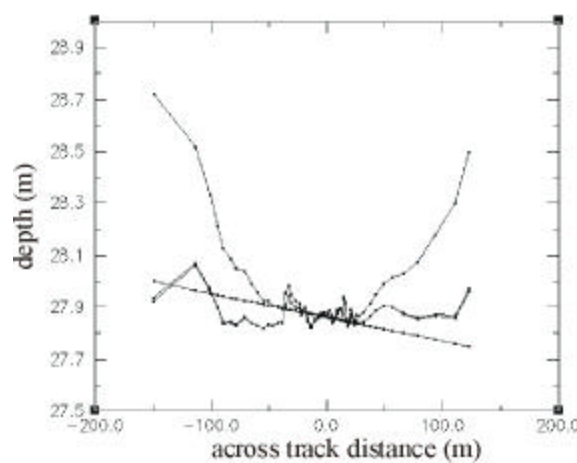


*Figure 64: Plot of the survey line average swath deformed by the two-layer SSP, which brings it as close as possible to the trend of the crossing line.*

## 7.6. ROUGHNESS OF THE SEAFLOOR

Even with the averaging used in the two methods described above, the natural morphology of the seafloor sometimes still appears in the profile used to determine the refraction coefficients. This will happen if there is significant topography of length scales at the dimension of the averaging (200 pings used here). This residual topographic signature will bias the computations and can result in false coefficients. In order to prevent this from happening, we estimate the roughness of the area and weight the refraction coefficients accordingly to this roughness. The stronger the roughness, the less trust we place on to the coefficients and vice-versa. Refraction artifacts are usually highly visible in flat and monotonous terrain and much less visible in rough topography zones.

The roughness is defined in an area by two different components. The first component is called the across-track roughness; it is determined from the variance about the average profile in a segment of the survey line. The second component is the along-track roughness; it is the roughness of the nadir area along the survey line.

#### *7.6.1. Across-track roughness*

The across-track roughness is computed from the average profile in each segment of the survey line (see 7.4.2) and at the crossing points of two lines (see 7.5.2). The coefficients of a parabola that best fits the shape of the average profile are computed. Such a parabola is not

symmetric on the  $y$ -axis because the natural slope is present in the data. It has an equation as follows:

Eq. 92 
$$y = ax^2 + bx + c$$

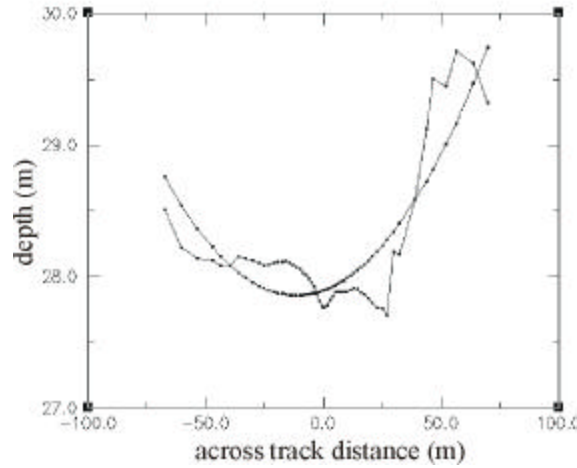


*Figure 65: average profile of a segment of a survey line with the best fitting parabola from which the roughness value is computed.*

The roughness  $r$  of the average profile is defined as the sum of the square of the differences between the best fitting parabola  $d_{parabola}$  and the average depths  $d_{ave}$  computed for the  $N$  beams.  $r$  is then divided by the number of beams  $N$  used. The roughness is then normalized by the average nadir depth  $\bar{z}$  in order to make it independent of the depth of the area where it is computed. What we consider as roughness here is in fact the average of the residuals of a second-degree approximation of the across-track profile. The shape of the refraction artifacts



is very similar to the shape of a parabola. The result of the roughness computation is then independent of the magnitude of refraction artifacts. The outer beams are kept out of from the computation because they are normally soundings of dubious quality and are unlikely to be representative of the true seafloor roughness. The formula used is shown below:

$$Eq. 93 \quad r_{across} = \frac{\sqrt{\sum_0^N (d_{ave} - d_{parabola})^2}}{N\bar{z}}$$

#### 7.6.2. Along-track roughness

The along-track roughness describes the roughness in the nadir part of the stripe of seafloor ensonified in an along track direction. This computation is realized in each segment of the survey line. For each ping in the segment, the depths of the five beams around nadir are averaged together. The position of the resulting depth is computed as the distance from the coordinates of the nadir beam of the considered ping to the coordinates of the first ping of the survey line. We have thus a series of couples (depth, distance). The trend (best fitting linear line) of this depth series is computed, see Figure 66. The roughness is computed as the sum of the squares of the differences between the averaged nadir depth and the value of the trend at this position. The formula for this computation is shown below with  $d_{nadir}$  the average nadir

depth,  $d_{trend}$  the depth of the trend and  $N$  the number of pings in the line segment, as the across-track roughness it is normalized by the average nadir depth  $\bar{z}$  :

$$Eq. 94 \quad r_{along} = \frac{\sqrt{\sum_0^N (d_{nadir} - d_{trend})^2}}{N\bar{z}}$$

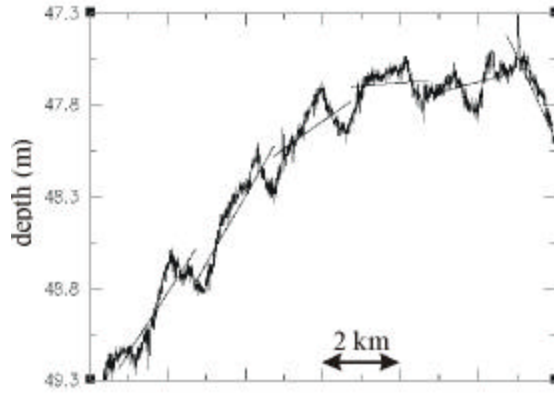


Figure 66: Part of the depth profile of a survey line with the best fitting straight lines for each of the segments from which is computed the roughness value.

### 7.6.3. Weighting of the refraction coefficients

The final roughness  $r$  used is the average of the across-track and along-track roughness.

The two roughness coefficients  $r_{across}$  and  $r_{along}$  have the same amplitude.

$$Eq. 95 \quad r = \frac{r_{across} + r_{along}}{2}$$

The refraction coefficients are then weighted accordingly to the roughness computed. A null roughness will leave the refraction coefficients unchanged. The greater the roughness, the less efficient the method would be, the more the alteration of the swath due to the refraction coefficient should be reduced. The weighting function below fulfills these two requirements:

$$Eq. 96 \quad \Delta c_{new} = \Delta c_{old} \frac{1}{1 + ar}$$

The positive constant  $a$  is determined depending on how strong the weighting is wished to be. The choice of  $a$  is up to the user who chooses it according to the kind of topography present in the area. In the presence of very rough local topography, a high value of  $a$  should be chosen so as soon as the roughness increases the weighting will strongly reduce the amplitude of the coefficients. In the presence of flat and monotonous area with only long wavelength topography (large with respect to the swath width and the 200 pings), a small value of  $a$  should be chosen. This weighting is applied to both the surface sound speed discontinuity  $Dc=c_0-c_1$  and the discontinuity between the two layers at the depth  $z_b$ ,  $Dc=c_2-c_1$  ( $c_1$  is constant), see Figure 67.

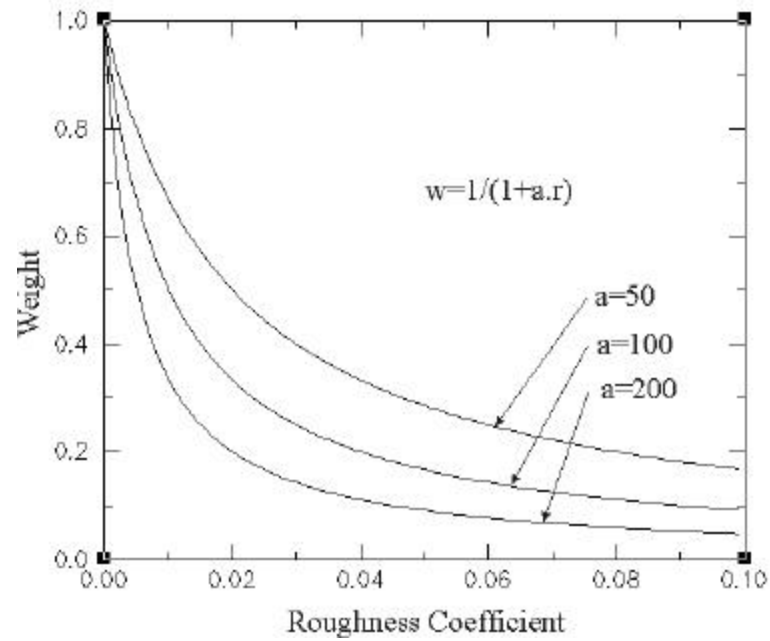


*Figure 67: Graph showing the relation between the roughness and the weighting to be applied to the refraction coefficient correction. The higher the roughness the lower the weight and therefore the more the correction is reduced. No roughness implies no weighting and thus full unattenuated coefficients.*

## 7.7. OPTIMISATION OF REFRACTION COEFFICIENTS

This section is common for the two cases of parallel and crossing lines. It is repeated successively in the different segments along the lines and once at the intersection between two crossing lines.

Once the first computations are done (see §7.4 and §7.5), the search for optimal SSP coefficients starts. The correction sought has the form of a two layer artificial SSP. We have seen in Chapter 6 that the width  $z_s$  of the discontinuity layer, the velocity of the first layer  $c_1$  and the velocity of the second layer  $c_2$  are dependant variables. We have established in the §3.4 the nature of the influence of the surface sound speed  $c_0$  on the shape of a swath. Therefore if we fix the depth of the discontinuity  $z_s$  and the sound speed of the first layer  $c_1$ , the only variables that we look for are  $c_2$  and  $c_0$ .

#### *7.7.1. Parallel lines case*

We are looking for an equivalent 2-layer SSP which brings the swath of line #2 as close as possible to the two segments of line joining on one side the nadir depth of line #1 to the nadir depth of line #2 and on the other side the nadir depth of line #2 to the nadir depth of line #3 (see Figure 53).

The function to minimise on which the search is based is the sum of the square of the differences between the adjusted swath and those two segments of line. A minimum of this function is sought. The SSP coefficients, which best minimize the function, constitute the SSP correction chosen.

### 7.7.2. Crossing lines case

We are looking for a two layer SSP that adjusts the averaged swath of the survey line as close as possible to the nadir profile of the crossing line. The function to minimise used in this case is the sum of the squares of the differences between the trend of the nadir profile of the crossing line and the average swath of the survey line. One is projected onto the other. In order to find these minimums, the Fibonacci search algorithm is used [Cheney, 1980]. This algorithm looks for the minimum of a continuous function  $f$  in an interval  $[a, b]$ . It is described in *Figure 68* and *Figure 69*.

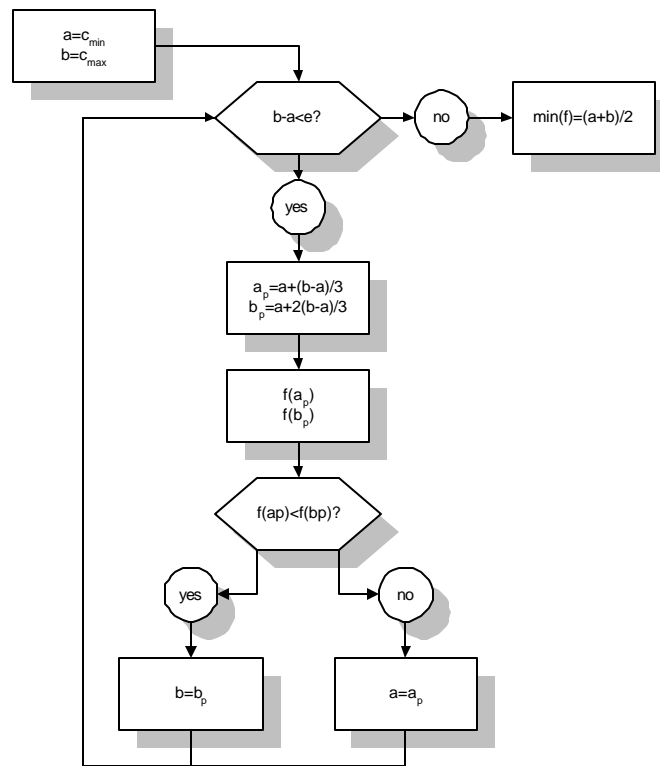


*Figure 68: Diagram showing the Fibonacci search algorithm.*

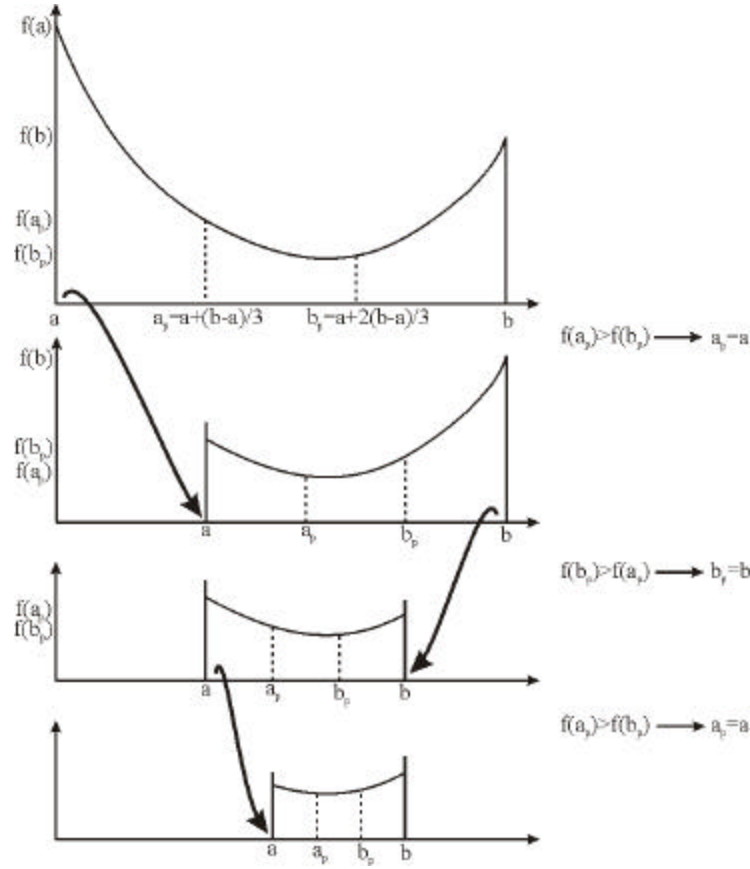


Figure 69: Diagram showing how the Fibonacci algorithm works in order to find the minimum of a function.

In our case,  $a$  and  $b$  are the two values defining an interval in which the optimum sound speeds ( $c_0$  and  $c_2$ ) are looked for. The initial values chosen are 1450 m/s for the lower extremity of the interval and 1550 m/s for the higher. The refraction coefficients are around 1500 m/s, which is the global average of the sound speed in seawater. The function  $f$  is always

positive (sum of squares) and takes large values when the refraction coefficients are at the extremities of the initial interval [1450,1550].

The algorithm compares the values of the function at one third and two third of the interval [a, b]. The interval is reduced by one third of its length on the side where the function is the highest. After a certain number of iterations the length of the interval is considered small enough to give a good accuracy of the minimum which is then taken in the middle of the interval.

A critical condition is that a minimum of the function must exist in the interval arbitrarily chosen [1450, 1550]. If this condition is not fulfilled, the algorithm is unable to find a solution. The length of the interval won't fall below the threshold and after a certain number of iterations the algorithm is stopped arbitrarily.

The algorithm uses an iterative methodology to get to the minimum of the function  $f$ . It looks for a minimum of the function  $f$  alternatively for  $c_0$  and for  $c_2$  until the difference between the last and the new sound speed estimate for the two variables is below a certain threshold  $\epsilon$  ( $\epsilon=0.01$  in order to have the estimates to two decimals places) (see Figure 70). The solution moves on a 2D surface on a path leading towards the sought minimum (see Figure 71). On this graph can be noticed a trend indicating the presence of a correlation between the two variables.



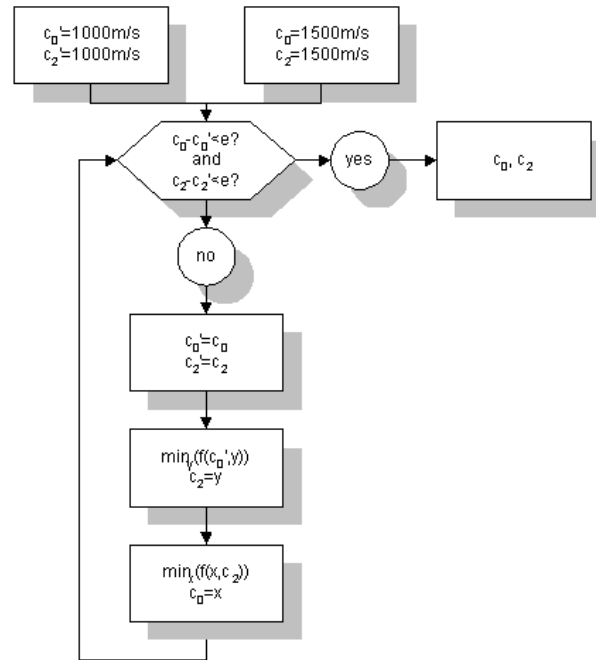
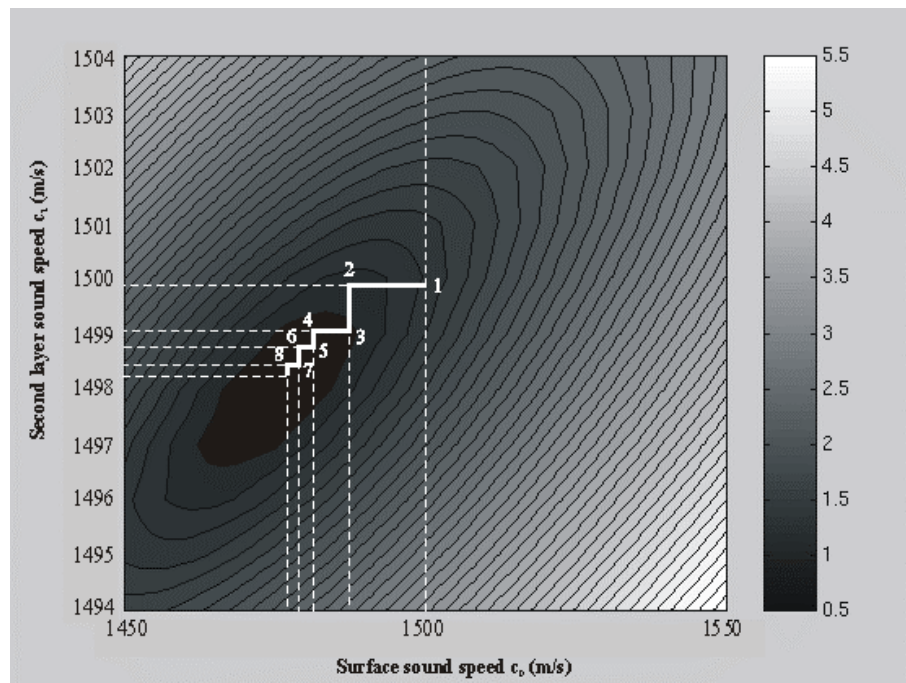


Figure 70: Flowchart describing the iterative method used to minimise  $f(c_0, c_2)$ .



*Figure 71: Graph illustrating the iterative methodology used to minimise of  $f(c_0, c_2)$ .*

## 7.8. FINAL COMPUTATIONS

For each segment of a survey line flanked by two other lines and for each intersection point between two lines the Ref\_Clean package generates a two-layer SSP solution. The four coefficients of the SSPs from a line are stored in a specific file. This file has to be in a growing ping number order. As explained in the description of the OMG Refraction Tool (see §4.5.1), for each ping of the survey line there is an associated correction that is an interpolation of the two closest corrections already listed in the file.

The refraction tool holds the coefficients constant at the two extremities of the line. A flat SSP (coefficients: 2, 0, 5, 0) is put automatically at the first and at the last ping number of the line in order to smooth down the closest corrections at the extremities. This is done because the closest correction generated can be at a certain distance (if the lines do not have the same length) and the correction might be not valid anymore. The end of lines are also subject to motion sensor problems that induces in the data gross roll biases and long period heave errors, which makes any attempt of refraction artifact removal pointless and possibly misleading (see external errors in the §7.9).

Such a refraction coefficient file is generated for every survey line. These files are then used with the OMG software (*weigh\_grid*) that is used to apply these coefficients and to grid the dataset in order to create a DTM of the data.

The flowchart of Figure 72 summarizes the methodology described in this chapter.

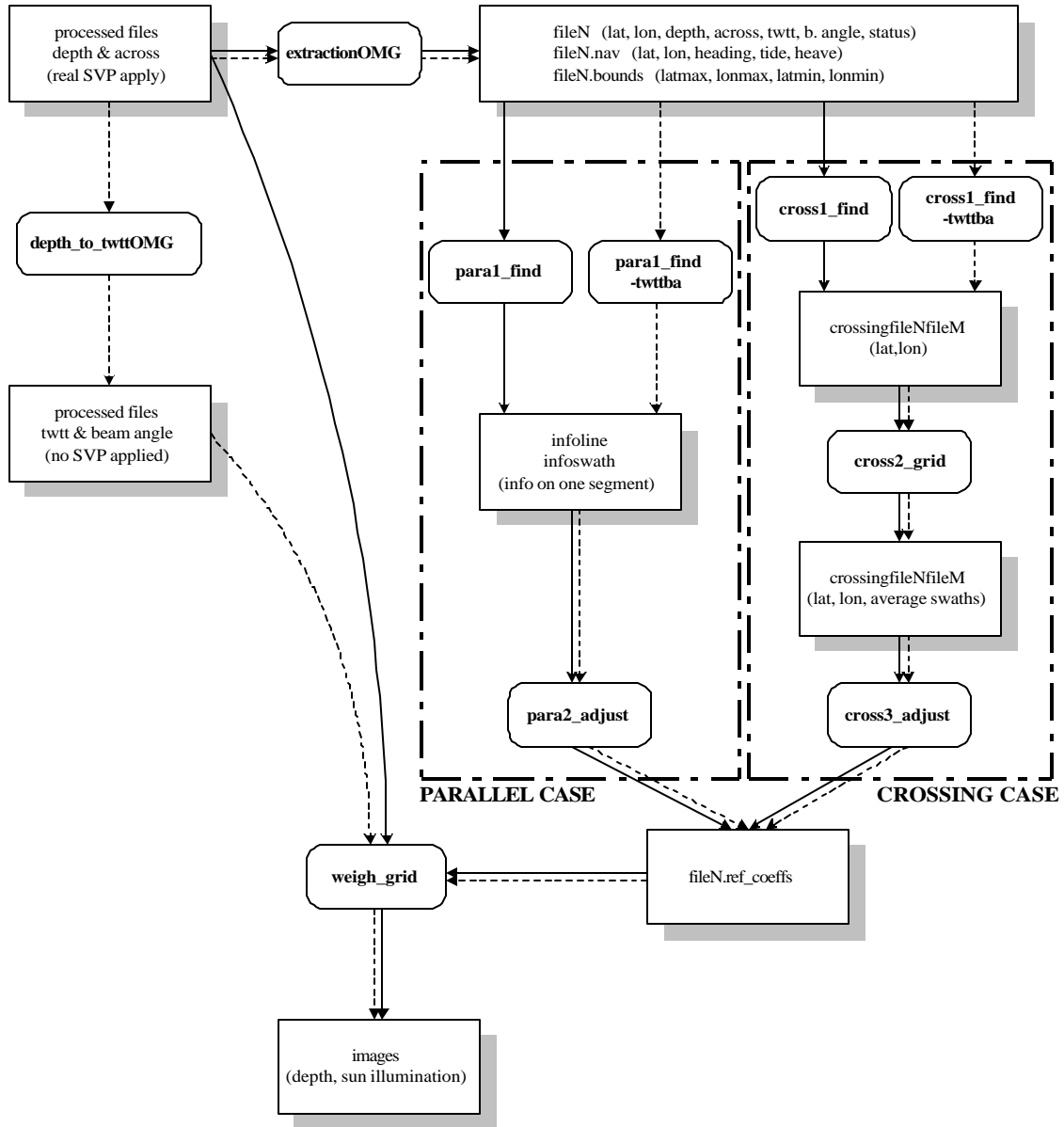


Figure 72: Flowchart of the Ref\_Clean method. The dashed path is the approach using the transit time and beam angle.

## 7.9. EXTERNAL ERROR SOURCES

A series of errors external to refraction problems affect multibeam soundings. In this section we look at the consequences of the presence of such errors on the application of the method proposed here. We distinguish the vertical errors, the rotational errors, the errors induced by an imperfect patch test and the errors in the swath itself (amplitude/phase transition and penetration artifacts).

#### *7.9.1. Vertical Errors*

Different kinds of vertical errors can be present in multibeam soundings. They can be due to an imperfect tidal reduction or problems with long period heave. These errors induce an erroneous vertical displacement of the swath.

It affects the method proposed here in the following way:

- For the parallel lines comparison, the vertical displacement is present in the average nadir depth computed in each segment. These three average nadir depths being taken as references to adjust the swath of the middle line, an error in one of these three values leads the method to output erroneous refraction coefficients. These coefficients adjust the swath of the middle line in order to make it fit as smoothly as possible to the trend between the three nadir average depths. Before application of the method, if there is a tidal problem, there will be a step between the uplifted swath and the others. After processing, this false step is smoothed but is

still present. More importantly this will result in an inappropriate selection of refraction coefficients (see Figure 73).

- For the crossing line comparison, the offset found between the two average profiles gives an estimation of the vertical error present (see §7.5.4). The two profiles are however brought together for the estimation of the refraction coefficient. The vertical error due to tide imperfections therefore does not interfere with the application of the refraction removal method. It resides in the processed data as it was before processing.

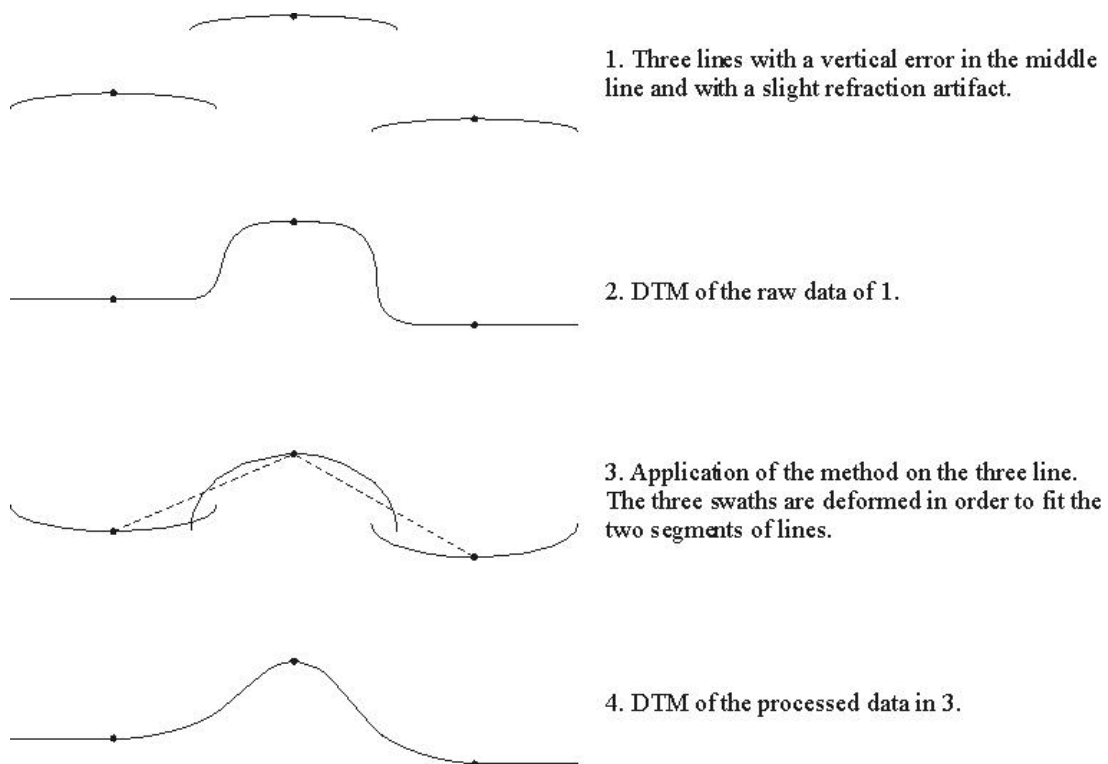


*Figure 73: Effect of the application of the proposed method onto a line affected by a vertical offset in the context of crossing lines. The method smooths the step but does not remove it.*

#### *7.9.2. Rotational Errors*

Roll bias is also sometimes present in multibeam data. It occurs under different circumstances such as after an imperfect patch test or during and after a strong turn of the vessel with a motion sensor that does not account properly for lateral accelerations. It can be observed as a tilt of the swath with respect to the neighbour lines. One end of the swath is higher than the end of the neighbouring swath and the other end lower (see Figure 74). It is a big hindrance towards the success of the method because the roll error is not symmetric with respect to the vertical axes at nadir.

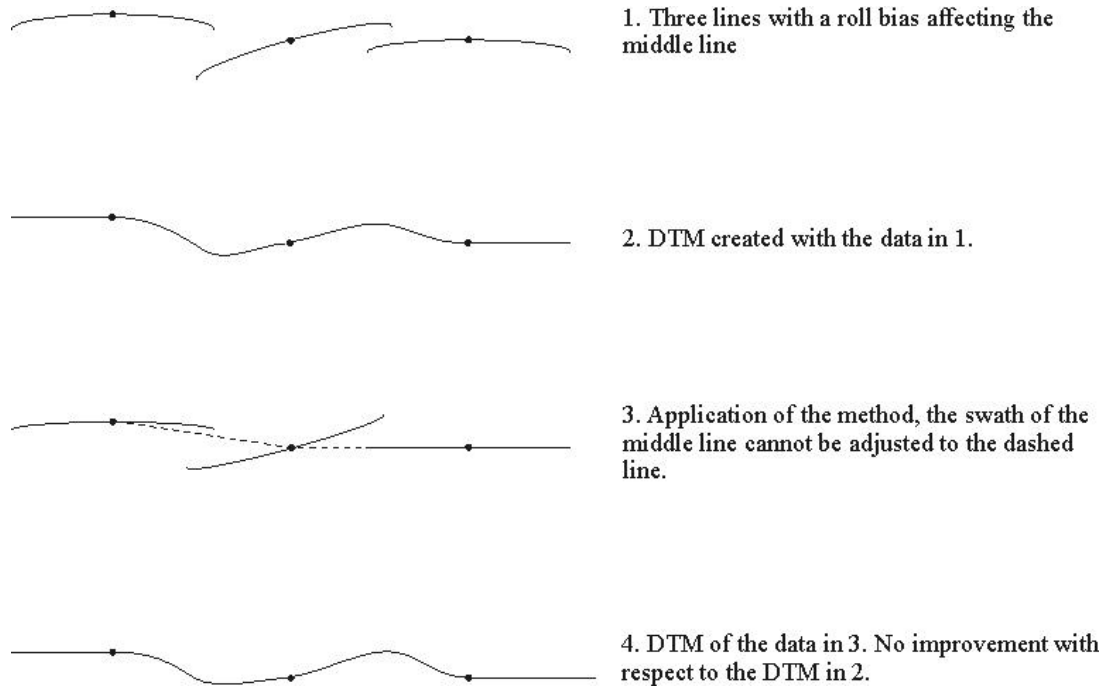


*Figure 74: Effect of the application of the proposed method onto a line affected by a roll offset. The method is inefficient to perform correctly in this case.*

A SSP application symmetrically affects both sides of the swath, and thus no refraction adjustment can make the swath fit better with its neighbours. The presence of roll bias in the data prevents the method from operating correctly. The roll bias stays in the processed data.

### *7.9.3. Imperfect patch test results*



An imperfect calibration of the echosounder generates four kinds of errors in the data: a roll offset, a pitch offset, a gyro offset or/and a time delay.

The case of the roll bias has been examined in the previous paragraph (see §7.9.2). A pitch offset, a gyro offset and a time delay create horizontal shifts of different kinds. The horizontal shift of a pitch offset is depth dependent. The horizontal shift of a gyro grows with across-track distance and is a displacement about the nadir of the swath. The horizontal shift of a time delay is an along-track displacement independent of the depth.

The consequence onto the final data of such horizontal offsets is that the data from different parallel lines do not match with each other. As well for crossing lines: the data that really intersects the other line is not exactly at the location of the intersection. These horizontal offsets interfere in the method when the parallel lines are segmented (the data to be compared do not match perfectly) and when the average profile of the crossing line is computed.

However the horizontal displacements are very small assuming a reasonably flat seafloor compared to the number of swaths averaged in both cases (parallel and crossing lines) and to the width of the swath; it does not have then a noticeable effect on the refraction coefficients computed.

#### *7.9.4. Depth errors in the swath*

- Variable quality from amplitude and phase detection

As the grazing angle increases from nadir to the outer beams, the amplitude of the signal becomes weaker and is stretched over a longer period of time making the bottom detection less accurate. At this time, the bottom detection algorithm is switched from the amplitude detection onto a phase detection algorithm. At the transition, the data is noisy and many spikes are present. The amplitude solutions are at their poorest and thus tend not to match with the first phase detection. This random noise is filtered out by the averaging over the number of pings. It does not affect the method used.

- Penetration artifacts

The acoustic pulses transmitted near vertical incidence often penetrate the seafloor as well as being reflected at its surface. Such effect occurs in very low impedance bottom types. The results of this phenomenon are manifested as dips in the sounding solutions of the nadir area of the swath.

These two artifacts, which do not occur systematically for all the pings, do not interfere noticeably in the application of the method proposed here. This is because the computation of the average nadir depth is made over the 30 middle beams and the average profiles are made over a large number of swaths. Only large anomalies can thus influence the average significantly and these should have been removed in the data-cleaning phase.

- EM1000 ‘Hump’ artifact

This is a Simrad EM1000 specific malfunction. This sonar is used for the example of an application of REF\_CLEAN on a real dataset in the next chapter. For every individual transducer array, each beam-pointing angle deviates from the design angle by a small shift. The manufacturer normally measures these shifts in controlled conditions and a calibration table is used on board the vessel to compensate for these deviations. In the case of the EM1000 on the F. G. Creed the calibration table used for some surveys was not appropriate resulting in a characteristic angular distortion to the across track profile. This results in the near nadir detects come in about 1.25% too shallow with respect to the outer swath detects. It produces a swath parallel artifact observable in a square uplift of the central part of the swath. It can be corrected by a systematic upward angular rotation of all outer swath beams. The angular shift was empirically estimated through averaging of large volumes of data on near flat seafloors.

In our case, this artifact will reduce the efficiency of REF\_CLEAN. These errors are present in the average swath used to generate refraction coefficients.

## 7.10. SOFTWARE DESCRIPTION

### 7.10.1. General Description

The source code is written in C++. The software has been developed on a UNIX workstation Silicon Graphics. The software written by the author relates to the OMG software by the mean of ACSCII files outputs of the program *rationalOMG.c*. The software developed generates as well ASCII files usable by the OMG software.

### 7.10.2. Written Code

The programs developed by the author are the following:

Ref\_Clean main modules:

<i>para1_find.c</i>	540 lines
<i>para2_adjust.c</i>	597 lines
<i>cross1_find.c</i>	255 lines
<i>cross2_grid.c</i>	282 lines
<i>cross3_adjust.c</i>	526 lines

Refraction research programs:

<i>angle.c</i>	210 lines
<i>apply_svp.c</i>	109 lines
<i>gridding.c</i>	158 lines

*real\_ref.c* 176 lines

*refraction.c* 58 lines

Programs adapted from the OMG source code *rationalOMG.c*:

*depth\_to\_twttOMG.c* 101 lines

*extractionOMG.c* 200 lines

### 7.10.3. CPU time

The times given below correspond to the application of Ref\_Clean to the specific case of the multibeam data acquired in Saint John harbour in June 1994.

**Step #1:** Extraction from the merged files: 35 min for 42 lines (50 sec by line).

**Step #2:** Computation of the coefficients (parallel lines case): 1 hour 35 min.

The 42 lines of the dataset have an average of 6000 pings of 60 beams. Each line takes an average of 2 min 30 to process.

**Step #3:** Computation of the coefficients (crossing lines case): 2 hours 27 min.

There are 201 intersections where a SSP is computed. This gives an average of 43 sec by intersection.

**Step #4:** Griding of the data with the coefficients computed: 16 min.

All the methodology described in this chapter is applied to an actual dataset in the next chapter.

## **CHAPTER 8 - RESULTS AND ANALYSIS**

The Ref\_Clean tool is applied in this chapter onto a multibeam survey that was carried out in the Bay of Fundy. First, we present the actual dataset. The focus of the discussion is then applied to extracting information about the oceanography of the area from the different physical measurements taken during the survey. Then the Ref\_Clean method is applied to this dataset; each step is detailed separately. Finally the results of the two approaches are shown, quantified and analyzed. Recommendations conclude this last chapter.

### **8.1. PRESENTATION OF THE DATASET USED**

In this part, the method described above in Chapter 7 is applied on a real multibeam dataset. The survey chosen has been carried out for the Canadian Hydrographic Service in the approaches of the Saint John harbour (New Brunswick) in June 1994, see Figure 75.

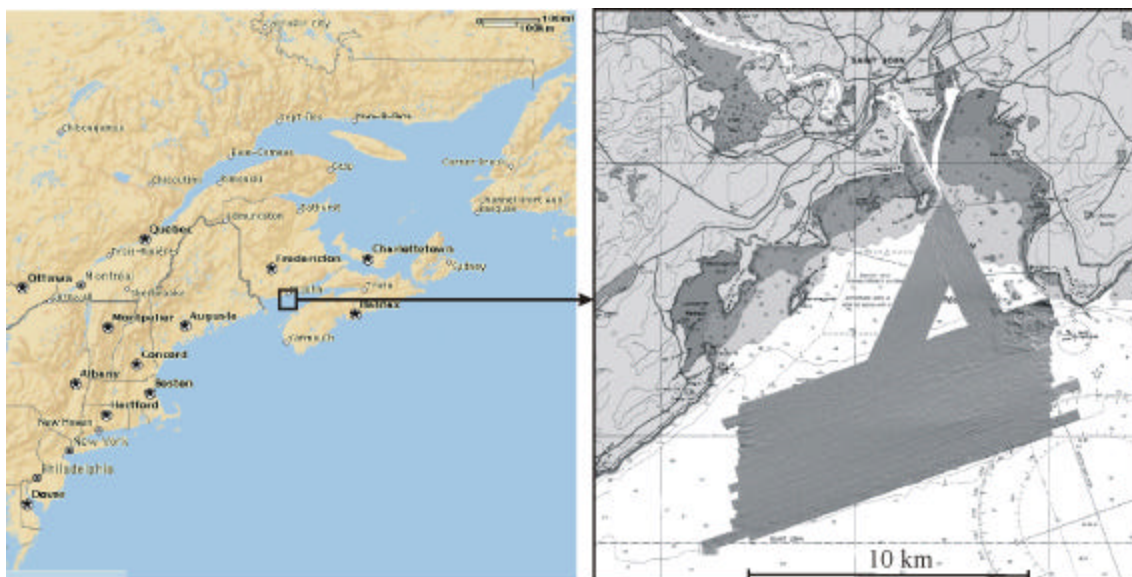


*Figure 75: Location of the dataset used.*

The multibeam echosounder used is a Simrad EM1000 [Simrad, 1992]. It is mounted on the hull of the swath vessel CSS Frederick G. Creed. The area surveyed is 13 km long and 5 km wide. The area is rather shallow; the seafloor lies below 10 to 60 meters of water. A sun illumination of the DTM is presented in Figure 76. The illumination is done from an azimuth orthogonal to the survey lines to outline the refraction artifact. The topography is relatively flat except for three main areas:

- 1- one major rotational slump deposit from a nearby dumpsite (on the upper right hand side North East corner),
- 2- a series of minor scattered rocks (on the lower right-hand side South East corner)
- 4- a series of stripes (going across the navigation NE-SW) in the centre of the survey area.



Because of the flatness of the seafloor, the refraction artifacts that corrupt the dataset appear very clearly as long stripes in the overlapping areas between the survey lines.



*Figure 76: Multibeam survey off Saint John (NB) harbour (CHS - Simrad EM1000 - June 1994). This picture shows the data without any refraction post-processing. Note the refraction artifact (stripes parallel to the survey lines).*

## 8.2. OCEANOGRAPHIC CONSTRAINTS

A study of the local oceanography must be done beforehand in order to constrain the shape of the likely SSP correction. In this survey, six SSPs have been taken at different locations of the area and at different days. The Figure 77 shows the SSPs geographic distribution.

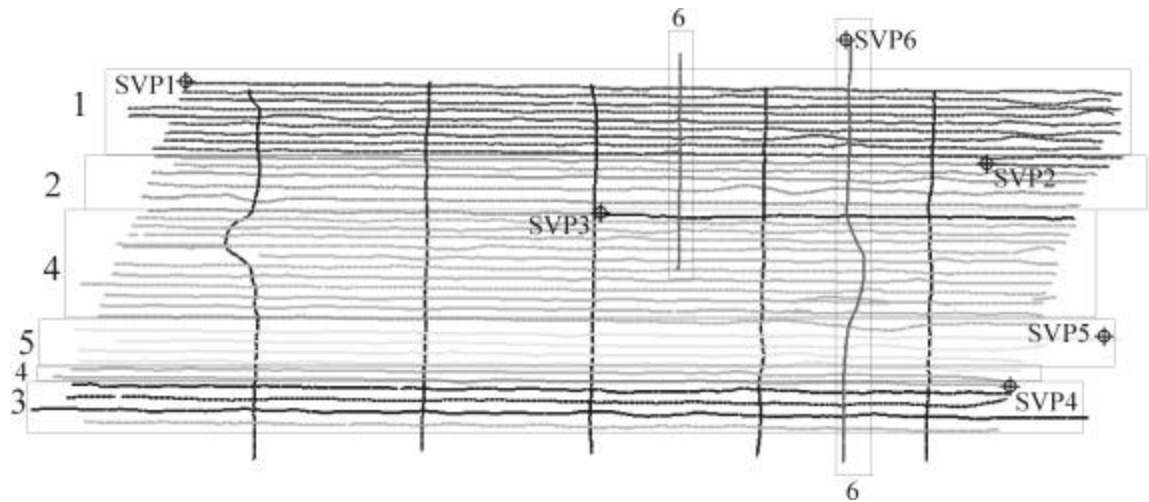


*Figure 77: Location of the actual SSPs in the survey area and the lines on which they have been applied.*

The survey is located in a very complex oceanographic area. The Bay of Fundy has the highest tidal amplitude of the world. The tidal currents are therefore very large. The survey is located off Saint-John harbour where the Saint-John River joins the Bay of Fundy. There is then fresh water running out of the river during a falling tide disturbing the salinity of the area. The survey however was conducted in June, which is not a time of major water flow from the

Saint-John River. A discontinuity front between the two different water masses is present in the area and moves with the tidal currents.

Figure 78 shows the times during the day and within the tidal cycles at which the six SSPs have been recorded. It shows as well the actual shape of these six SSPs. The fluctuations of the sound speed in all these graphs do not exceed 1m/s. They have various shapes and cannot be correlated with any of the following factors:

- Time of the day: there is no obvious difference between the SSPs taken early in the morning (SSP2, SSP4 and SSP5) later in the morning (SSP6) or around midday (SSP1, SSP3).

- Position in the tidal cycle: no difference either between the SSPs taken at the flood (SSP2, SSP4, SSP5 and SSP6) and those taken at the ebb (SSP1, SSP3). All the SSPs have been taken at an intermediate tide level. The amplitudes are between 4.5 metres and 6.35 metres. A SSP taken at the highest or the lowest water level would have probably had characteristic features. Such a watermass may have been present and be the cause of some of the problems. The low SSP frequency prevented us of seeing it though.

There is not much oceanographic information that can be derived from the actual SSP profiles. The sound speed variations of the SSPs are small, they do not exceed 1 m/s. Therefore no constraints can reasonably be put onto the SSP correction model.

The refraction artifacts can be explained then by a great variability of the sound speed in time and space. The samples that we have at different times during the day and during the tidal cycle are not sufficient.

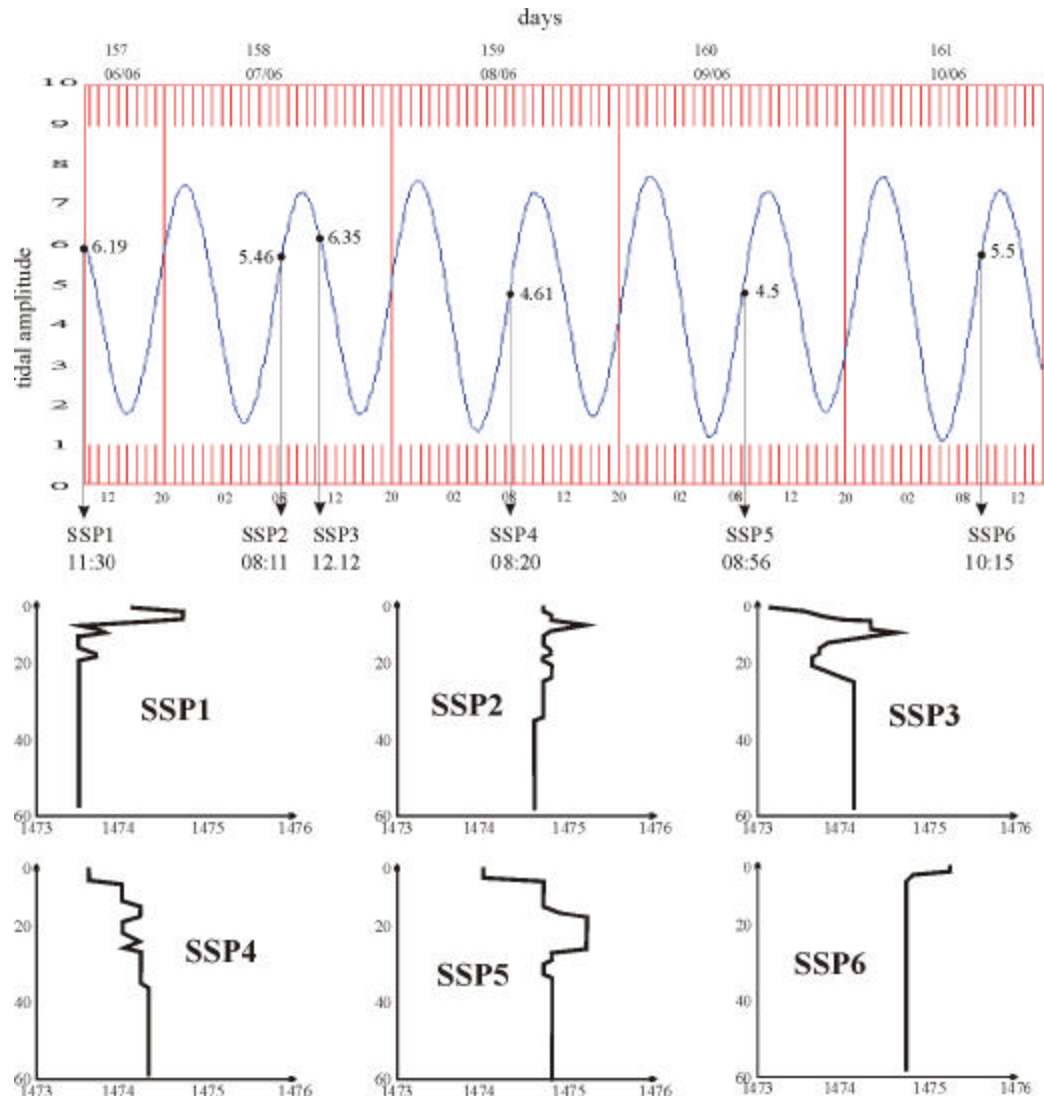


Figure 78: Shape of the six SSPs and their position in the graph of the tide variations during the survey time

### 8.3. APPLICATION OF THE METHOD

### 8.3.1. Data format conversion

First, with *extraction\_OMG* (see §7.1), the data files of the survey lines are converted into the Ref\_Clean format. This operation creates three files for each survey data file: a bathymetric file, a navigation file and a boundary file. From these files, we are now ready to proceed to the estimation of refraction coefficients.

### 8.3.2. Parallel lines case

The first case is the case of parallel lines. As described in the §7.4 each survey line is decomposed in segments having two parallel segments on each side (from the two parallel survey lines). The centers of each of these segments (463 points) can be seen in Figure 79 with the ship navigation. Notice that the outer lines do not have any black dots. The reason is that they have only one neighbour line and the method cannot be applied to them.

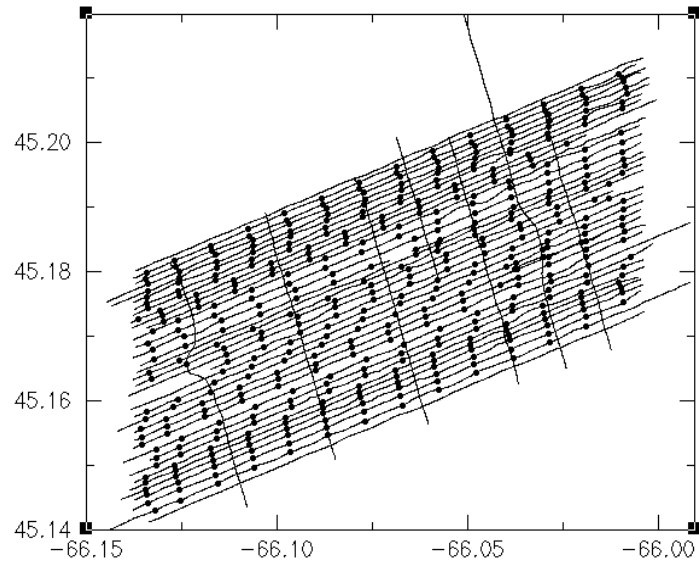


*Figure 79: Navigation of Saint John dataset. The black dots are the centre of segments of the survey lines where the estimation of refraction coefficients is conducted.*

The software is run in two sequences in the syntax written below.

*para1\_find line1 line2 line3*

*para2\_adjust infoline2 infoswath2*

### *8.3.3. Crossing lines case*

The second case is the case of crossing lines. As described in the §7.5 the algorithm looks for every check-line (seven check-lines in this case) the intersection points with all the other survey lines. The intersection points (233 points) found can be seen in Figure 79 with the

navigation tracks. Notice that a few intersections seem not to have been detected; they have been rejected due to the condition of difference in heading (within  $\pm 30^\circ$  from the orthogonal) between the two crossing lines that is not fulfilled.

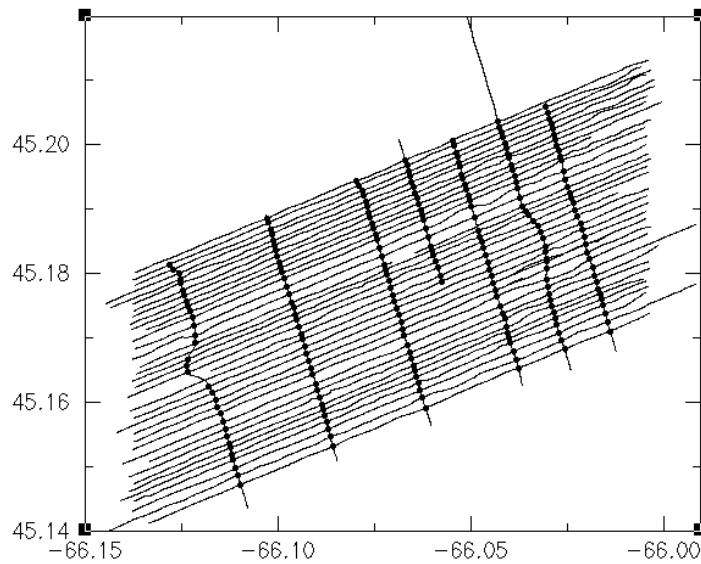


*Figure 80: Navigation of Saint John dataset. The black dots are the intersections between parallel survey lines and crossing check-lines, refraction coefficients are estimated at each of these locations.*

The software runs in three sequences in the syntax written below:

*cross1\_find file1 file2* (*file1* is the check line)

*cross2\_grid crossingfile1file2*

*cross3\_adjust crossingfile1file2*



This sequence generates a file called *line2.ref\_coeffs* or adds the computed coefficients into the existing file if it is the case. The coefficients are sorted by ping number after the application of the method so the crossing lines coefficients are put in the correct place among the parallel lines coefficients.

#### 8.3.4. *Computation of the Roughness*

The method loses its efficiency when the average profile contains noise coming from natural features. This occurs when the seafloor presents a rough topography, which is not removed by the averaging. As explained in the §7.6, the refraction coefficients are weighted with a roughness coefficient. There are two roughness coefficients (along and across-track) for each segment of every survey line. This data is gridded. Figure 81 and Figure 82 show the across-track and along-track roughness grids.

The main characteristic of Figure 81 is the peak of across-track roughness at the North-East corner of the area. It corresponds to the slump deposit that shows up on the DTM in the Figure 76.

The Figure 82 shows the distribution of the along-track roughness computed. The major rock outcrop noticed on the North East corner is also very apparent in this picture. In addition, however, it can be noticed on Figure 82 a high along-track roughness region parallel to the

direction of the survey lines. It covers the area mapped by the survey lines acquired during one particular day of the survey (June 7).

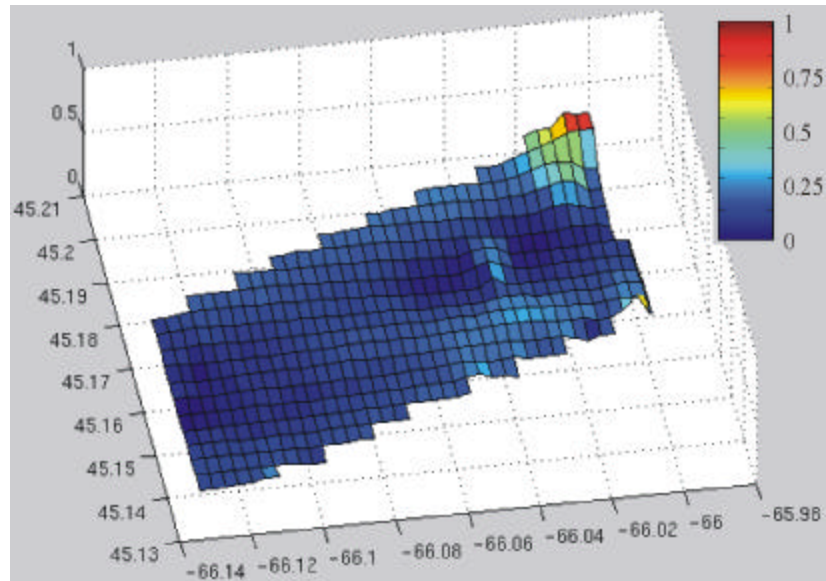


*Figure 81: 3d graph of the gridded geographic distribution of the across-track roughness for each segment of the survey lines.*

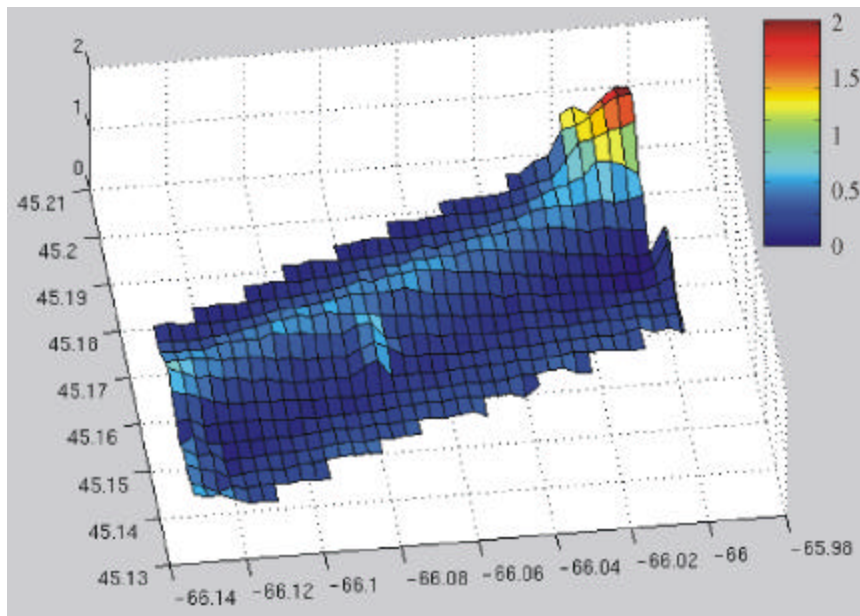


*Figure 82: 3d graph of the gridded geographic distribution of the along-track roughness for each segment of the survey lines.*

In Figure 83 the histograms of the heave of the vessel at each ping of the sonar are plotted for the four days of the survey (from June 6 to June 9). One can easily notice that the heave recorded during June 7 has a histogram with a large amplitude. The standard deviations of these histograms are displayed in Table 1. The heave was stronger this day and probably due to imperfections in the motion sensor, it produced residual heave-related artifacts in the data. We have then less confidence in the data because of the presence of noise from the strong heave and an appropriate weight on the SSP corrections is then justified. However if the heave residuals have a zero mean it does not influence the computation of the roughness and then does not interfere with REF\_CLEAN. These heave residuals can be seen in the data, see Figure 84.

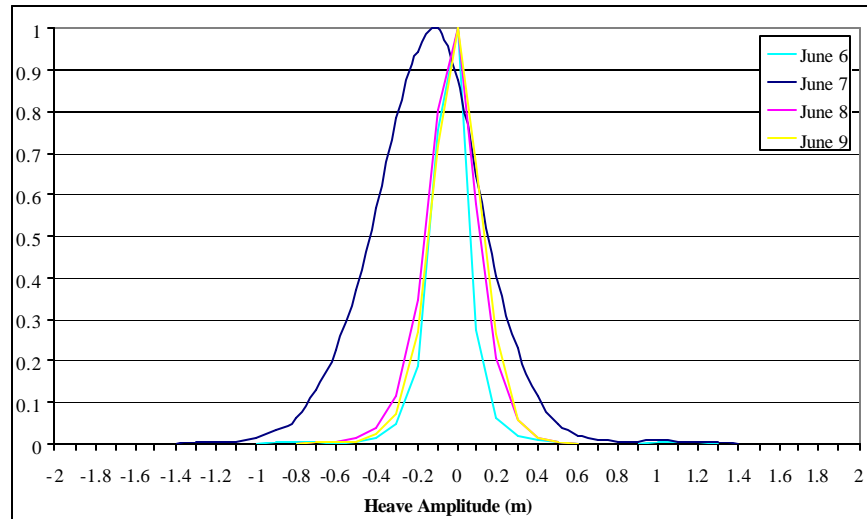


*Figure 83: Histograms of the heave measurements for each of the four days of the survey. Note that the histogram for June 7 is more spread out than the three other days.*

*Table 1: Standard deviations of the four histograms plotted on Figure 83 above. The histogram of the heave measured on June 7 has a much larger standard deviation than the histograms of the three other days.*

	June 6	June 7	June 8	June 9
<b><i>s</i> (m)</b>	1.64	<b>6.58</b>	1.66	1.33

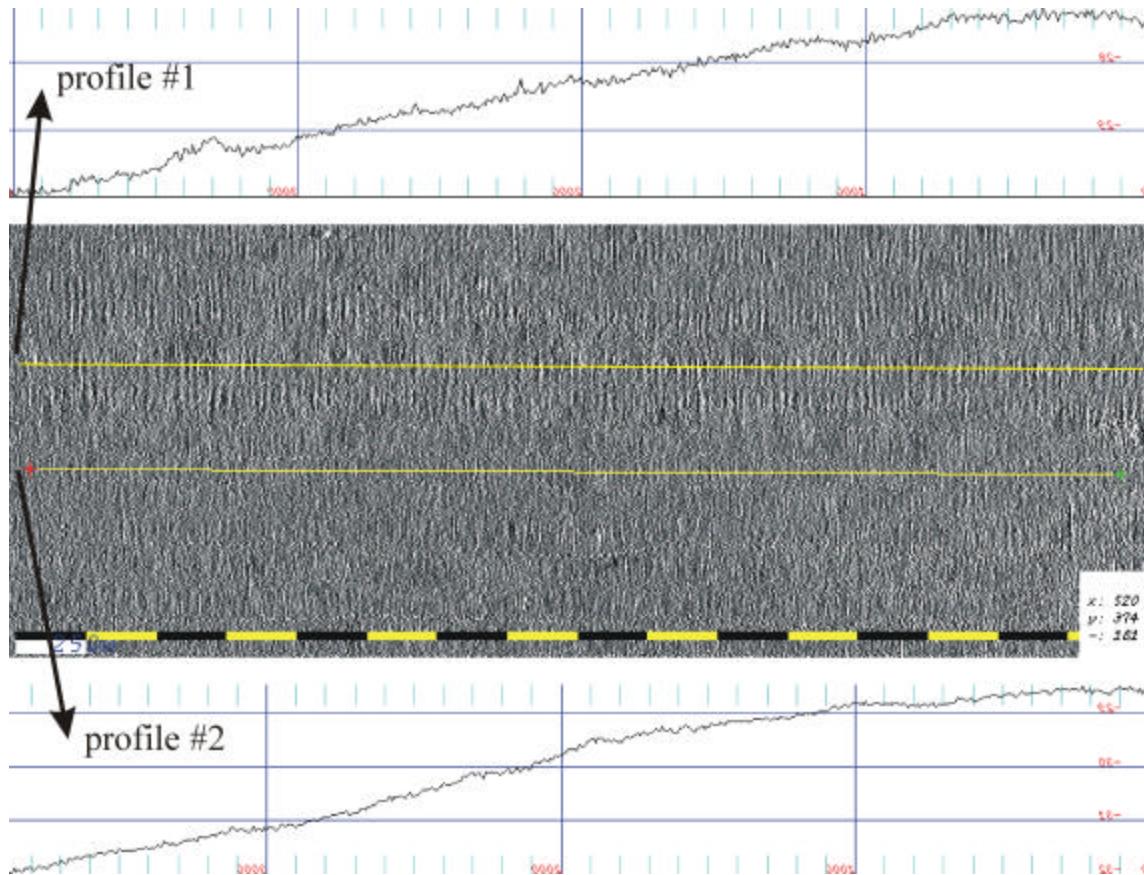
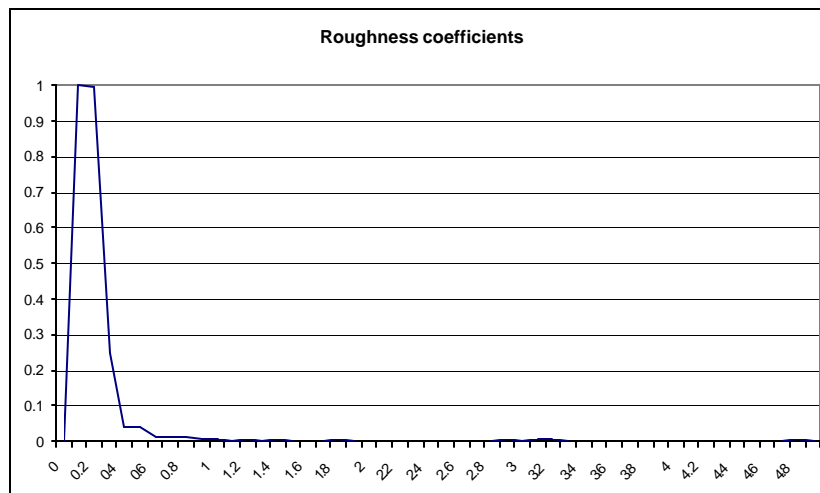


Figure 84: Heave residuals between June 7 and June 8. The upper part of the image corresponds to the data collected on June 7 and the lower part to the data from June 8. The heave residuals are stronger on the profile #1 than on the profile #2.

The two sets of roughness coefficients have been computed. Then, they are averaged together to obtain the final roughness coefficients that are used to weight the application of the SSP correction. A histogram of the roughness coefficients computed for this area is plotted below in Figure 85. Notice on this plot a peak around a roughness value of 0.2. This value

corresponds to the intrinsic noise in the system. A certain number of higher roughness data are scattered from 0.5 to 5.0. These values come from topographic roughness in the data. They are the values where the amplitude of the refraction coefficients applied needs to be reduced because these coefficients have been biased by the presence of this roughness.



*Figure 85: Histogram of the roughness coefficients in the Saint John dataset.*

### 8.3.5. Refraction coefficients

The optimisation algorithm is applied in order to adjust the average swath at each location on the maps above. As explained in §7.8, this operation generates for each survey line a file of refraction coefficients.

A special case occurs when one parallel line is composed of two (or more) survey lines. The survey lines have to be processed separately and the final coefficients written and sorted in the same file. Figure 86 illustrates this case.

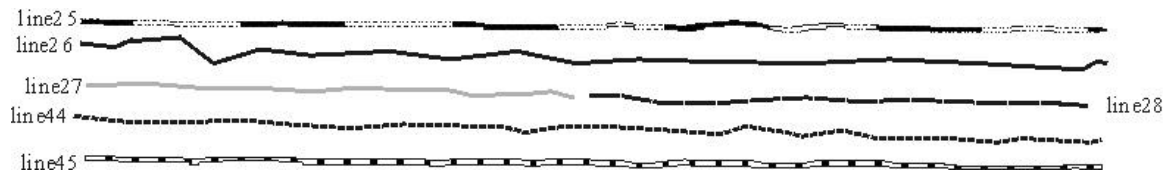


Figure 86: Case of a parallel line broken in two survey lines.

The algorithm runs in this case with the following series of set of three lines:

For line26: *line25 line26 line27*

*line25 line26 line28*

For line27: *line26 line27 line44*

For line27: *line26 line28 line44*

For line44: *line27 line44 line45*

*line28 line44 line45*

An example of a coefficient file is displayed below in the Table 2. Notice the null coefficients for the first and last ping.

*Table 2: Example of a refraction coefficient file for a survey line. Each row of this table defines a synthetic two-layer SSP correction, which will be applied to the data at the location of the ping number.*

Ping number of the line	Transducer depth (m)	Surface speed correction (m/s)	Layer depth (m)	Discontinuity amplitude (m/s)
1	2	0	5	0
164	2	2.572	5	0.200
358	2	0.523	5	2.164
474	2	0.941	5	0.870
724	2	1.069	5	1.505
...	...	...	...	...
771	2	0	5	-1.070
1404	2	-1.014	5	-2.961
1925	2	3.090	5	-1.537
2416	2	0.309	5	-2.228
2759	2	4.179	5	-1.327
3418	2	-0.585	5	-2.128
4325	2	-0.692	5	-2.676
5223	2	0	5	0

These coefficients are now analyzed geographically. At each coefficient corresponds latitude and longitude. The results in surface sound speed  $c_0$  and in the sound speed  $c_2$  of the second layer of the synthetical SSP are displayed for the two different approaches in the four figures below.

#### 8.3.5.1. First approach: SSP correction



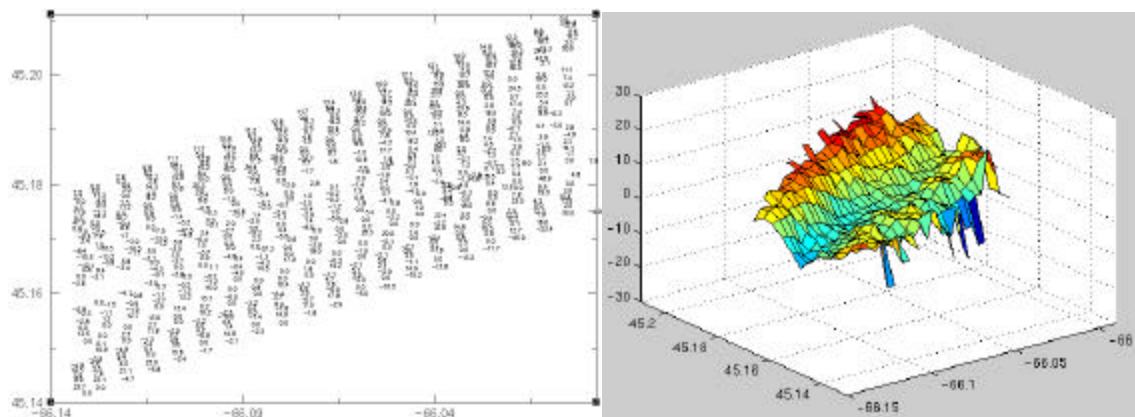


Figure 87: distribution of the surface sound speed  $c_0$ , corrections to the actual SSPs.

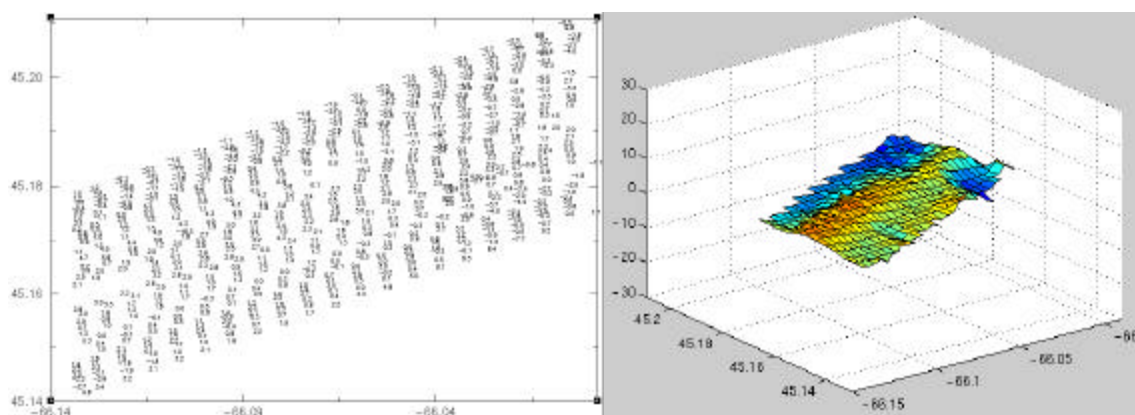


Figure 88: distribution of the sound speed  $c_2$  of the second layer, corrections to the actual SSPs.

### 8.3.5.2. Second method: new SSP

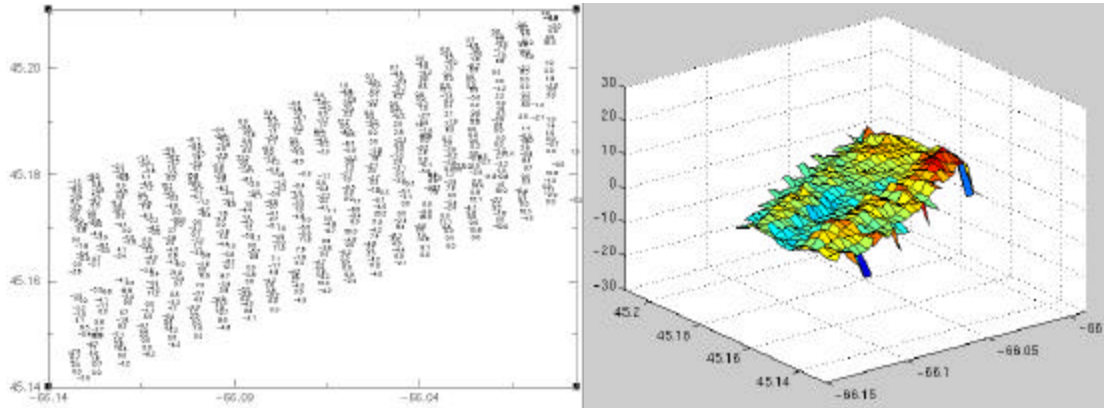


Figure 89: geo-distribution of the surface sound speed  $c_0$ , equivalent SSP.

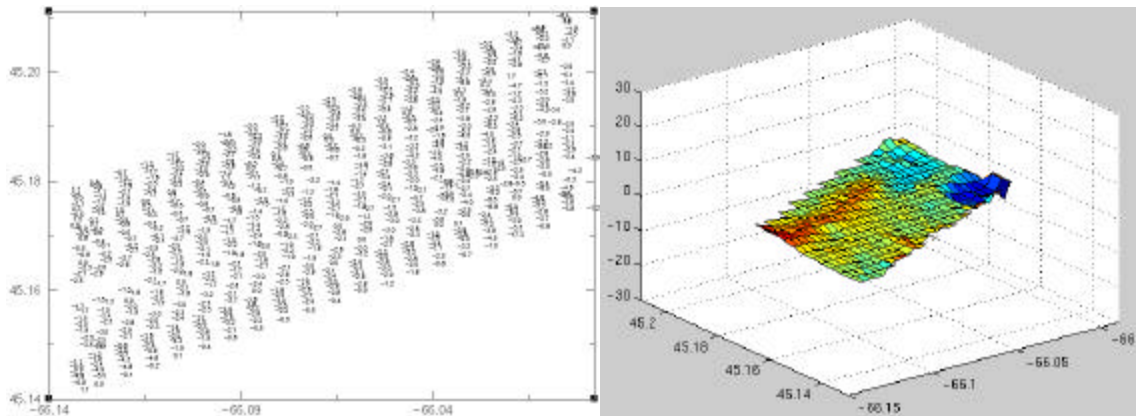


Figure 90: geo-distribution of the sound speed  $c_2$  of the second layer, equivalent SSP.

#### 8.3.5.3. Analysis of the distribution of the refraction coefficients

A few remarks come out from the four figures above (Figure 87, Figure 88, Figure 89 and Figure 90):

The values of surface sound speed  $c_0$  have much larger variations in amplitude than the values of  $c_2$ . The four graphs have the same scale; the 3D graphs of  $c_2$  appear very flat compared to the graphs of  $c_0$ .

In the correction values of  $c_2$ , two different zones can be distinguished in the Figure 88: a zone of negative  $c_2$  for the 7 most northern lines. All these lines have been run during the first day of the survey, June 6. The rest of the nodes for the other days have positive values.

The equivalent  $c_2$  values in Figure 90 are all negatives. They vary however depending of the location and the time of acquisition. You have higher values of  $c_2$  in the North West of the area and lower values in the South East. This reveals the presence of different structures of the water column in time and space.

## 8.4. RESULTS

Once we have all the coefficient files, we can proceed now to the creation of DTMs. The first DTM is created with the initial survey SSPs. The second DTM is made with the same data but with the refraction correction coefficients computed with the first approach of the Ref\_Clean tool. The third DTM is realized from the files created by the *depth\_to\_twttOMG* program with the refraction coefficients computed with the second approach of Ref\_Clean (see Figure 72). To have a better understanding of the impact of the method on the data, three cross-sections are also taken and looked at. In this section, we compare these three DTMs and the three cross-sections for the different approaches.

### 8.4.1. DTM comparison

The DTMs are decomposed in three parts in order to have a closer look to the results of the Ref\_Clean tool. These three parts are shown below in the three next pages (Figure 91, Figure 92, and Figure 93). These pictures are in fact a sun illumination of the DTMs. The azimuth in which the sun illuminates the data has been chosen orthogonal to the direction of the parallel lines in order to emphasize the relief parallel to the survey lines (such as refraction artifacts).

On the three pictures, it can be noticed that the Ref\_Clean tool operates correctly and reduces the amplitude of the long stripes that appear in the overlapping areas of the survey lines in the top parts of the three figures.

However a few remarks need to be made about these pictures:

1- Notice that some artifacts still appear at the extremities of the survey lines. These artifacts are not refraction artifacts but cornering effects (roll or depth biases) due to an imperfect motion sensor, which needs a certain delay of time to settle down after the strong motions involved during the turn just achieved (see §7.9.2).

2- As well some local artifacts seem to stay after applying the method at different places in the area. These artifacts are again due to imperfections of the motion sensor. It is sensitive to turns made by the helmsman to correct an offset of the ship from the straight planned survey line.

3- New very thin stripes appeared on the results of the second approach with the whole new SSPs. An eventual explanation could be that by using the second method we apply quite strong refraction coefficients to bring the data computed with a sound speed of 1500 m/s to a reasonable sound speed value. This value can be quite different from 1500 m/s. The computations may introduce distortions in the outer most beams, which are the most sensitive beams and generate these thin stripes.

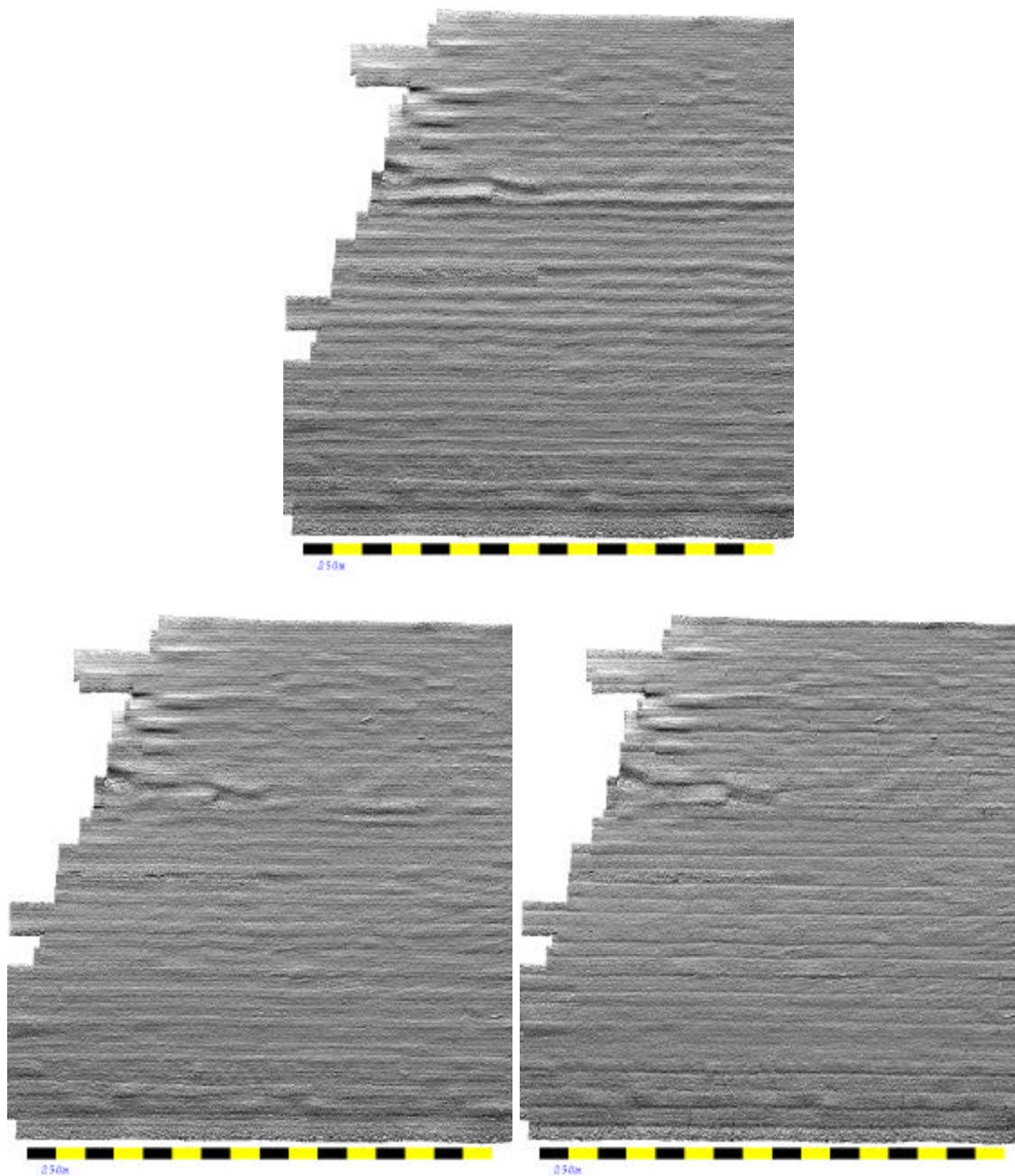


*Figure 91: Results for the western part of the survey area. Top image: initial data with the actual SSPs taken during the survey. Bottom left: results of the first*

*approach (corrected SSPs) Bottom right: results of the second approach (new SSPs).*

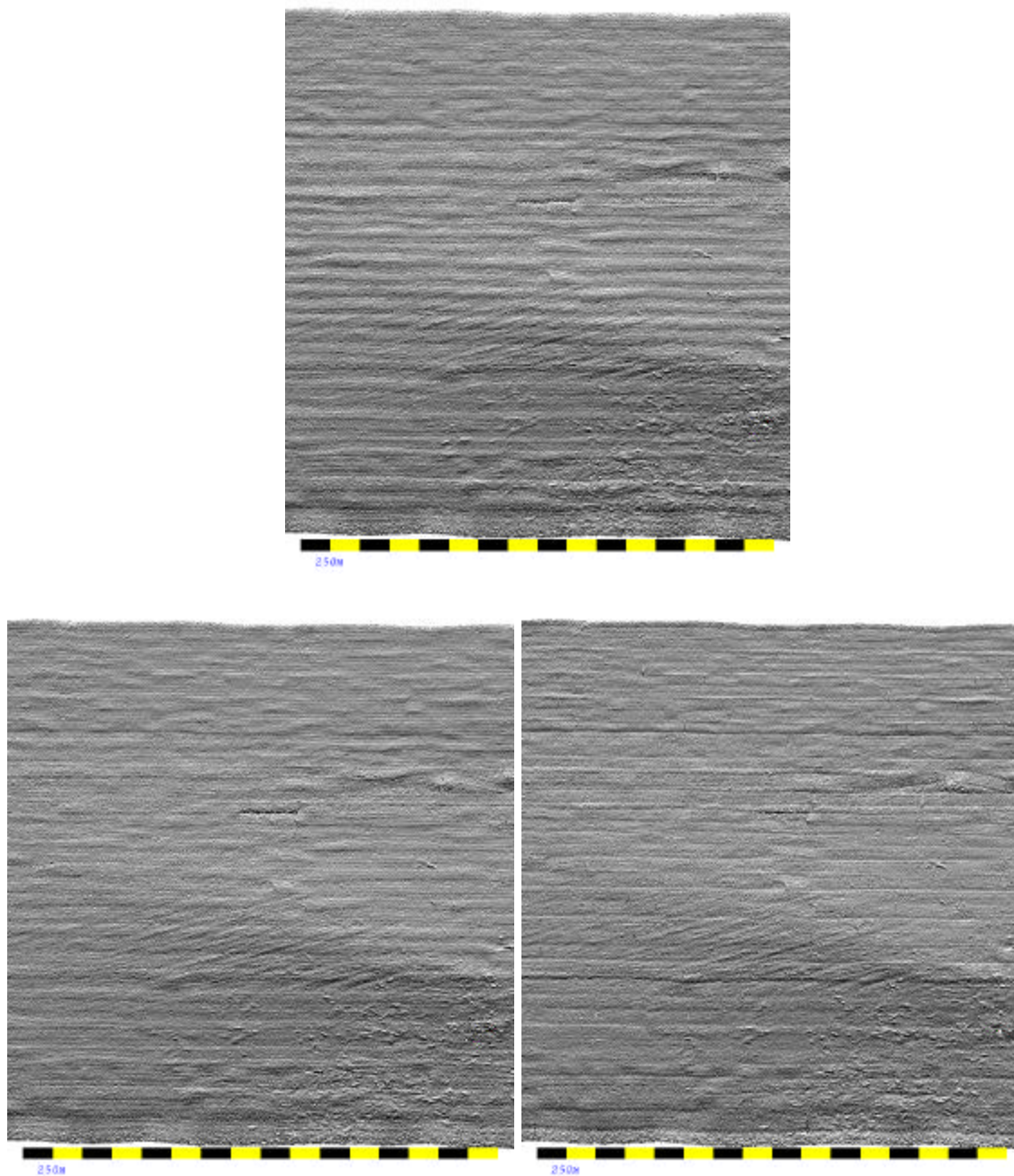


*Figure 92: Results for the central part of the survey area. Top image: initial data with the actual SSPs taken during the survey. Bottom left: results of the first*



*approach (corrected SSPs) Bottom right: results of the second approach (new SSPs).*

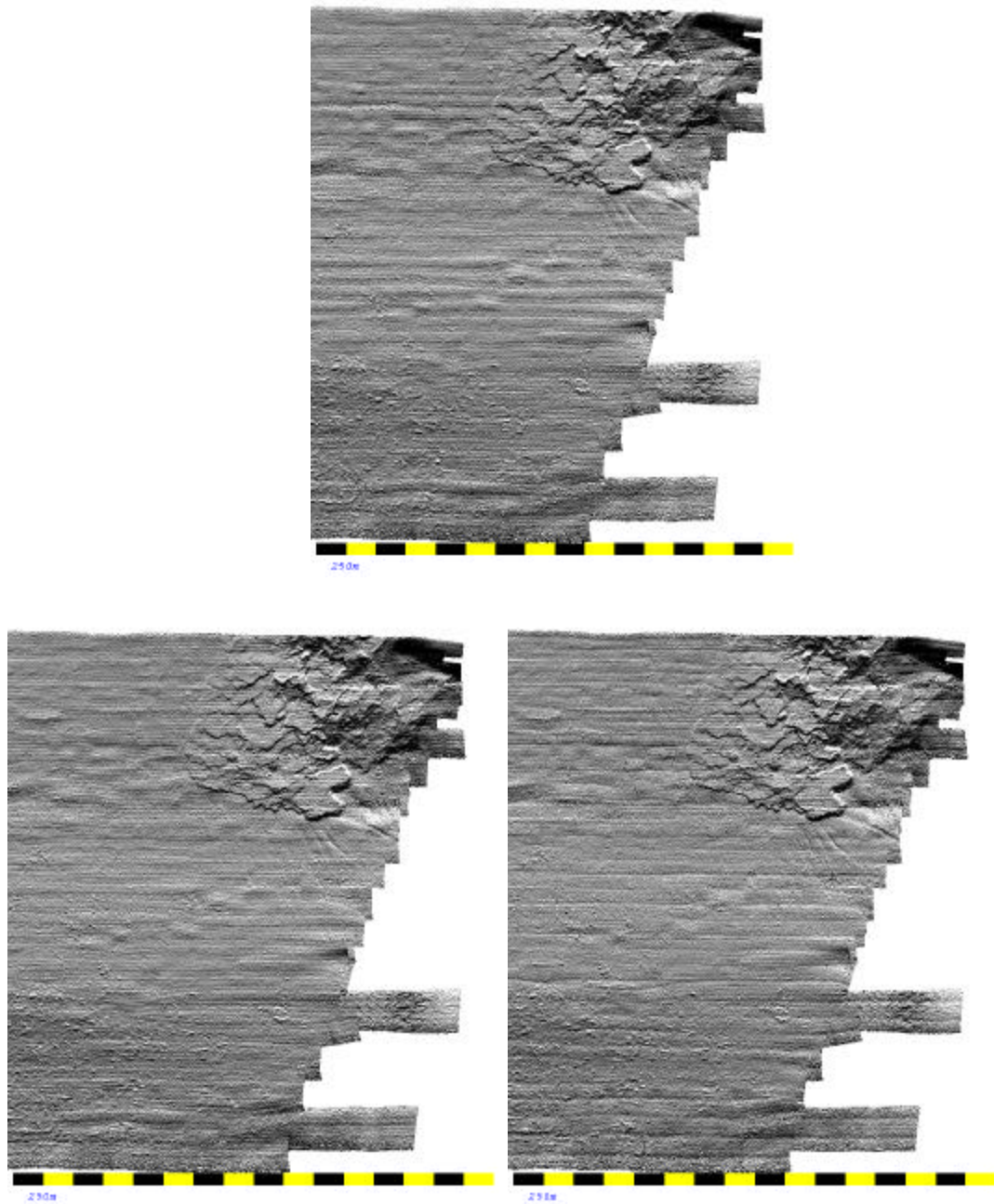


*Figure 93: Results for the Eastern part of the survey area. Top image: initial data with the actual SSPs taken during the survey. Bottom left: results of the first*

*approach (corrected SSPs) Bottom right: results of the second approach (new SSPs).*

#### 8.4.2. *Profile comparisons*

Three different cross-sections of the source soundings are taken orthogonally to the parallel lines at different depths. These profiles show, in a clearer way than with the DTMs, the effects of the Ref\_Clean tool onto the shape of the swaths (see Figure 94, Figure 95 and Figure 96).

One can notice from these three figures that the Ref\_Clean tool flattens the across-track profiles of the survey lines to make them aligned with each other resolving in this manner the refraction problems.

The shallowest profile (Figure 94) presents upward refraction artifacts when the two other profiles (Figure 95 and Figure 96) have downward refraction artifacts.

It can be seen on these figures that when a roll bias or a depth error affects the survey line the application of Ref\_Clean does not improve the situation (see External Errors §7.9).

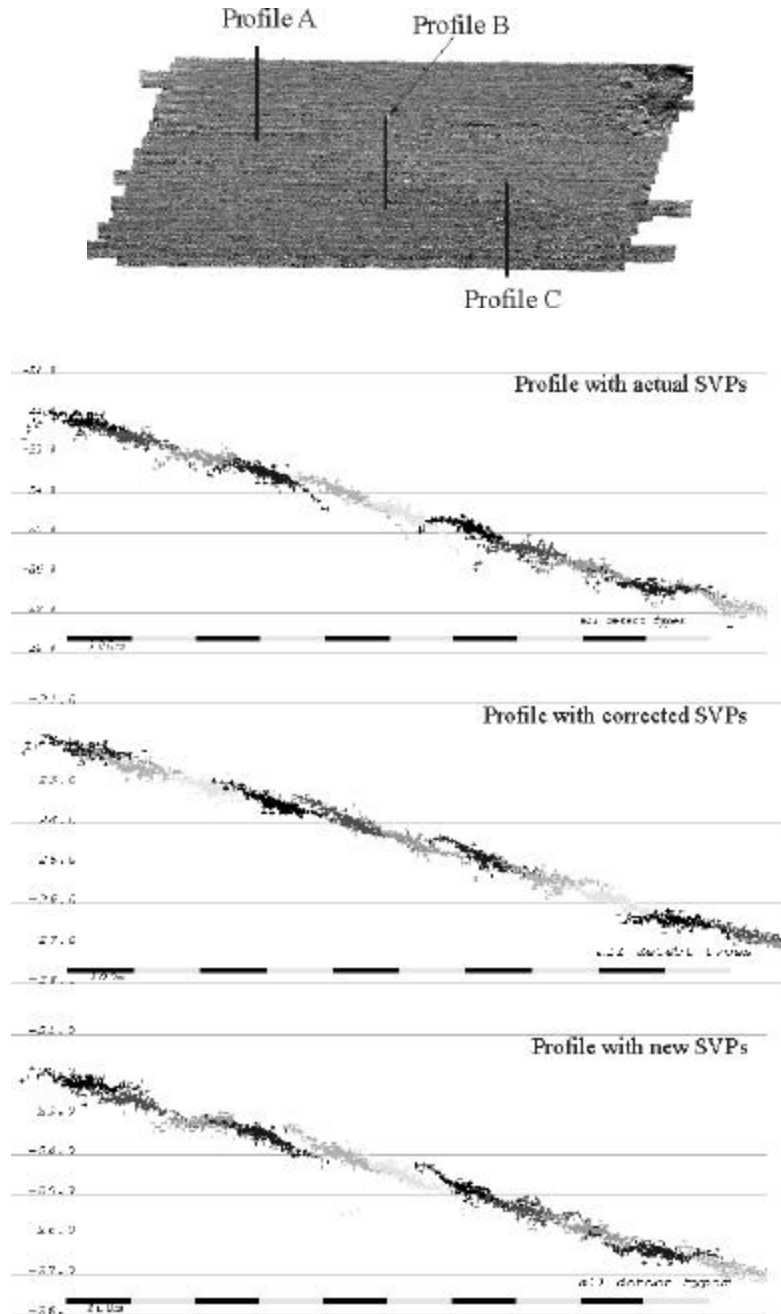


Figure 94: Profile A (shallowest area see its location in the map at the top of the page).

The three profiles below show how the Ref\_Clean tool changes the shape of the swaths with the two approaches considered.

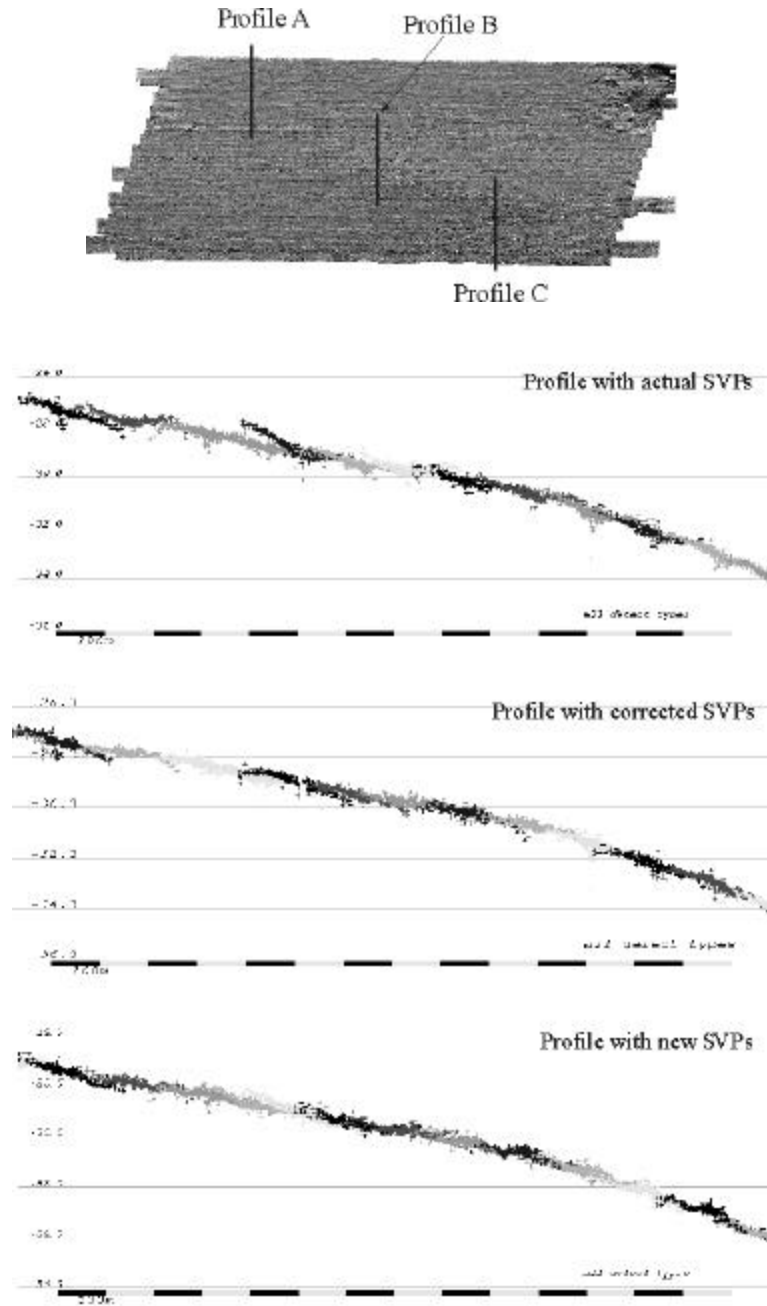


Figure 95: Profile B (intermediate area, see its location in the map at the top of the page). The three profiles below show how the Ref\_Clean tool changes the shape of the swaths with the two approaches considered.



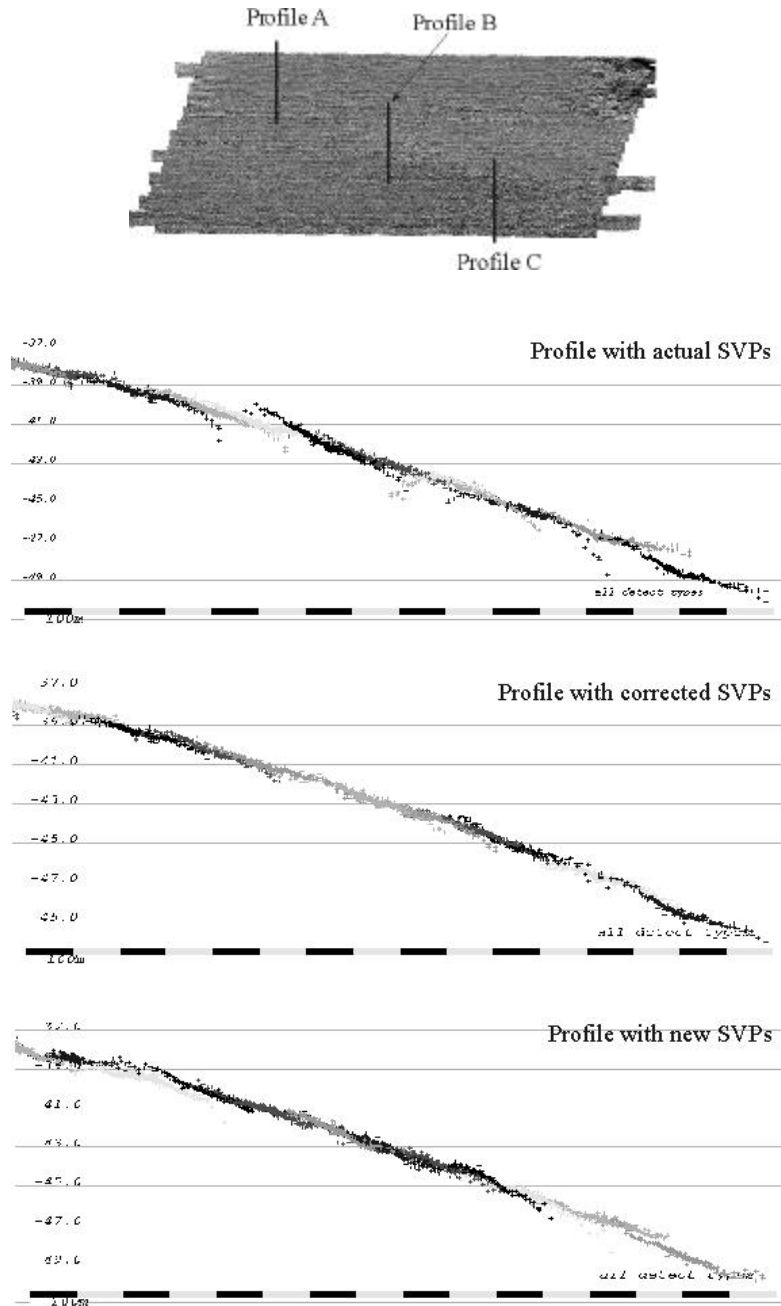


Figure 96: Profile C (deepest area, see its location in the map at the top of the page).

The three profiles below shows how the Ref\_Clean tool changes the shape of the swaths with the two approaches considered.



## 8.5. ANALYSIS

### *8.5.1. Cornering effects*

The echosounder EM1000 used for this survey was interfaced with a TSS 335B motion sensor. This instrument provides to the echosounder the motion attitude of the vessel (i.e. roll, pitch, heave and gyro). An investigation of the roll and heave errors present in the Frederick G. Creed – EM1000 when using a TSS-335B motion sensor [Hughes Clarke, 1993] reveals that at the surveying speed of 16 knots:

1/ the vessel after completion of a turn needs 3 minutes prior to start of line to be steady on course and

2/ it requires an extremely gentle line keeping.

In the dataset of Saint John harbour, such roll and heave biases can be observed at the start of the survey lines. Figure 97 shows two profiles taken across a few survey lines at each extremity of the surveyed area. In the profile #1 on the left, a few lines are alternatively one metre above and one metre below the previous one. It shows that the starts of these lines are affected by a heave bias of approximately one metre. In profile #2 a few lines show a rather pronounced roll bias.

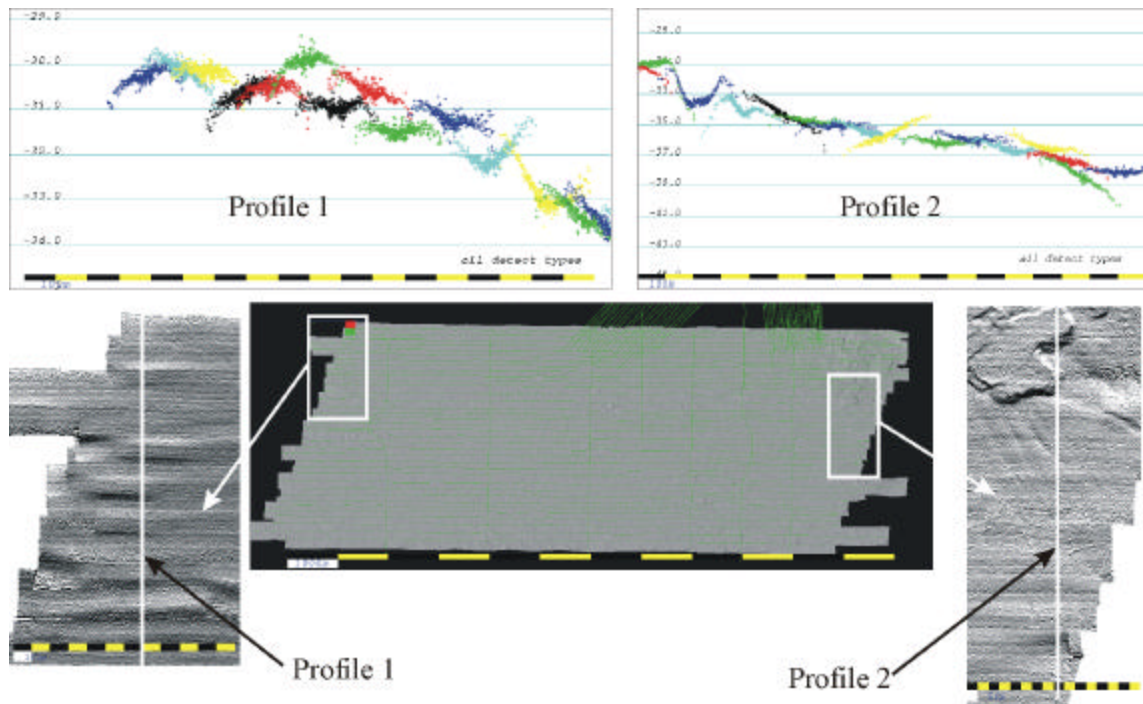
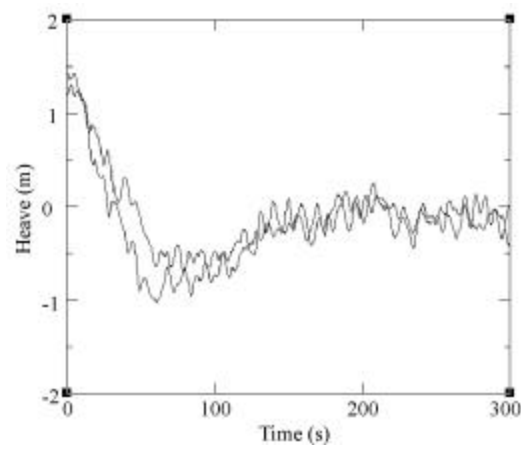


Figure 97: Roll and heave biases occurring at the extremities of the survey lines. Two profiles taken on each sides of the surveyed area show these artifacts.



*Figure 98: Graph of the heave versus time at the beginning ( $t=0$ ) of two survey lines.*

*There is a positive bias followed by a negative bias before a stabilisation around a zero mean.*

The heave for the start of two of these lines is plotted with respect to time on Figure 98. The heave bias is positive then negative before coming back to a zero mean value.

#### *8.5.2. Local roll artifacts*

The second recommendation from [Hughes Clarke, 1993] about an extremely gentle line keeping is also justified. A roll bias is induced in the data when the vessel goes away from a straight navigation and executes long period maneuvers. In the St John dataset, this event occurred on several occasions. A closer look into the data shows the roll bias that has been induced. On Figure 99 we see the example where the vessel has realized a perturbation around a straight line. Three profiles show that a roll bias follows the oscillation of the ship.

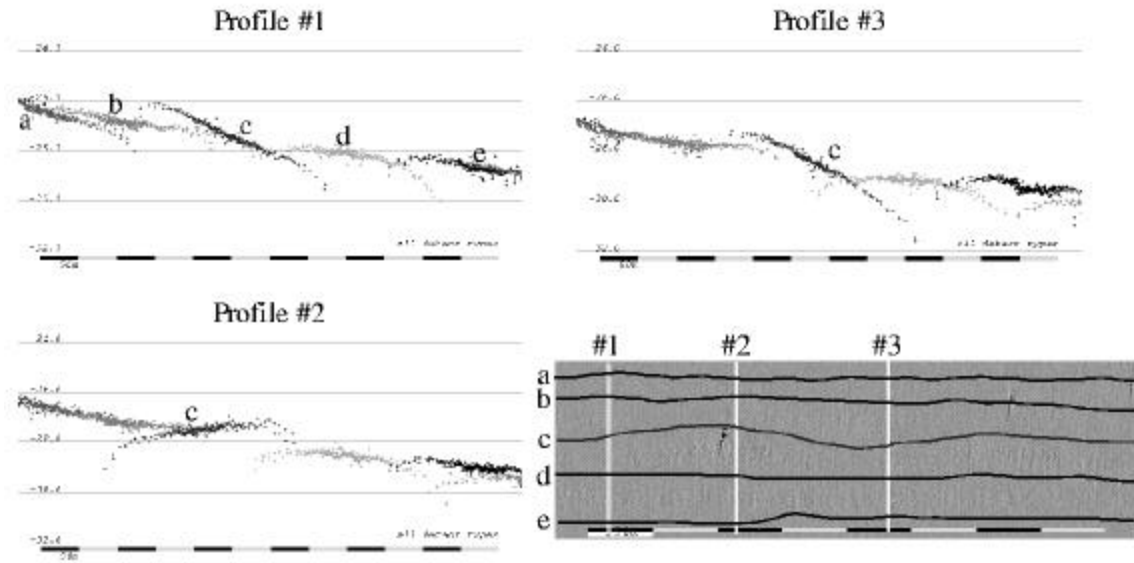
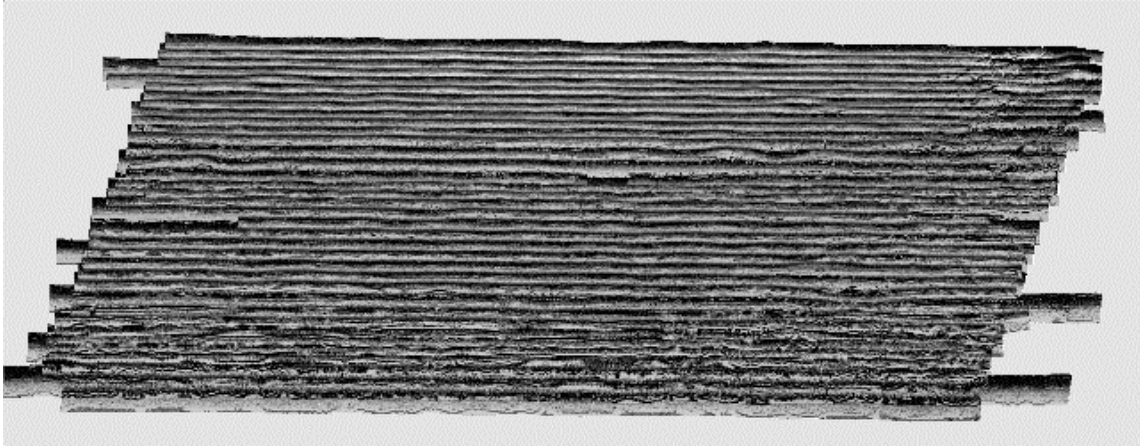


Figure 99: Roll bias in a survey line. The vessel slides away from a straight navigation.

These artifacts cannot be reduced by the refraction artifact minimisation method that has been described. They are expected therefore to remain after the application of this method.

### 8.5.3. Correction of artificial errors

An experiment has been run on the same dataset to test the performance of REF\_CLEAN. An SSP model has been applied uniformly over the whole dataset. This SSP is constituted by a sound speed discontinuity of 10 metres at the depth of 5 metres. This creates strong refraction artifacts in the data that can be seen in the Figure 100.



*Figure 100: Sun-illumination of the original DTM (Figure 76) on which an additional sound speed discontinuity of 10m/s at 5m has been added.*

REF\_CLEAN is applied in the same way as described above for the original dataset.

The resulting DTM is displayed on the Figure 101:

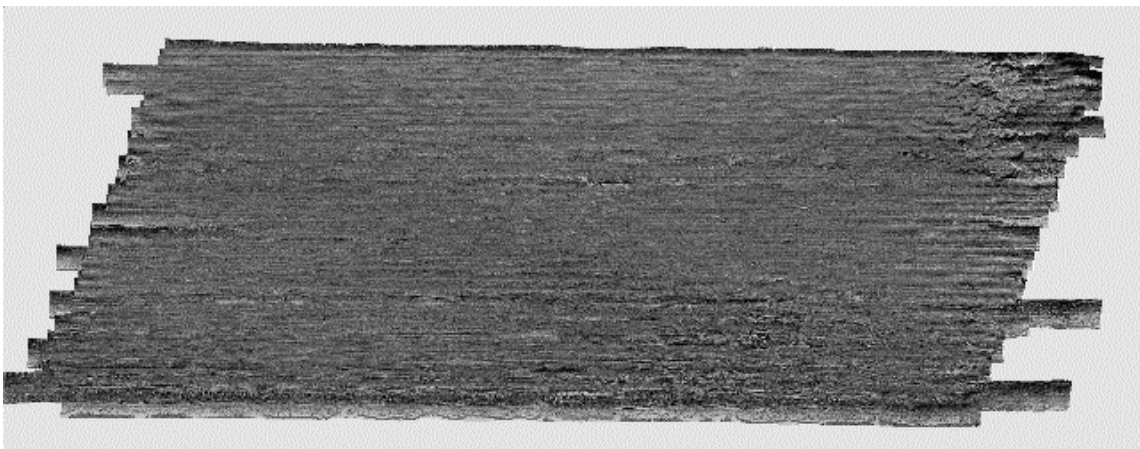


*Figure 101: Sun-illumination of the DTM generated with the refraction coefficients output from the application of REF\_CLEAN on the DTM on Figure 100 above.*

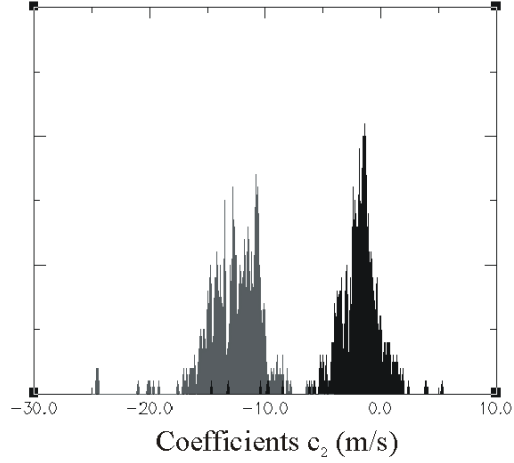


*Figure 102: Histograms of the coefficient  $c_2$  generated by the application of REF\_CLEAN on the original dataset (in black) and on the dataset degraded with a 10 m/s additional discontinuity (in gray).*

The strong refraction artifacts have been removed. The Figure 102 compares the histograms of the coefficient  $c_2$  generated by the first application of REF\_CLEAN on the original data and on the DTM artificially degraded. The two histograms are 10 m/s apart. This is a experimental evidence of the good performance of REF\_CLEAN.

## 8.6. QUANTITATIVE EVALUATION OF THE PERFORMANCE OF THE METHOD

### 8.6.1. *Parallel lines*

In this section, our goal is to evaluate the good performance of the method in a quantitative manner. In order to do this, we compare how the parallel lines match with their neighbouring lines in the area where the swaths overlap. This is done for the original data and the results of the 1<sup>st</sup> and 2<sup>nd</sup> approaches. These three cases are compared with each other. The methodology follows the different steps listed below:

**Step #1:** Generation of two DTMs, in which has been gridded every second parallel line.

**Step #2:** Similar generation of two DTMs with the data corrected by the first approach (correction of the survey SSPs).

**Step #3:** Similar generation of two DTMs with the data corrected by the second approach (generation of SSPs on top of a similar reference flat SSP).

**Step #4:** In each of these three couples of DTMs, the two DTMs are subtracted from each other. The DTMs resulting from these differences represent how well the lines are fitting with each other.

The methodology is illustrated in Figure 103.

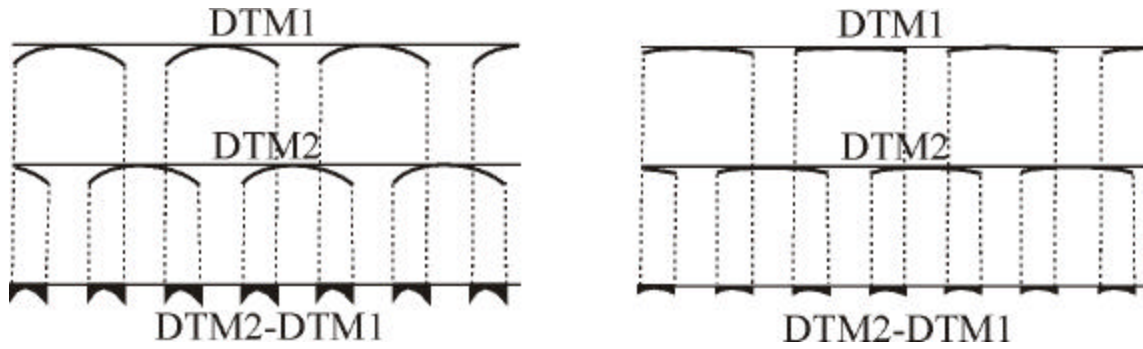


*Figure 103: Illustration of the methodology to quantify how well the parallel lines fit with their neighbours. The lines are gridded every second parallel lines and the two DTMs obtained subtracted from each other.*

**Step #5:** The histograms of the difference DTMs are then plotted (see Figure 104). The mean and standard deviations are computed (listed in Table 3).



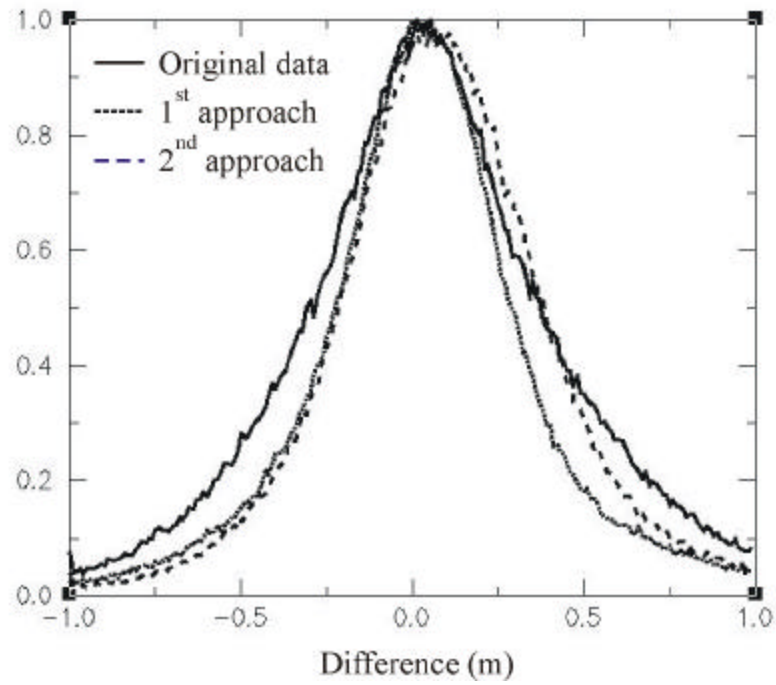


Figure 104: Normalized histograms of the difference DTMs computed to quantify the performance of the method in the parallel line case.

Table 3: List of means and standard deviations of the difference DTMs in the case of parallel lines.

	Original Data	1 <sup>st</sup> approach	2 <sup>nd</sup> approach
Mean	0.0679	0.0489	0.0978
Standard Deviation	0.4888	0.4206	0.3900

From these results, we can see that the standard deviations of the difference DTMs generated from the processed data are smaller than the standard deviation of the difference

DTM of the original data. The outer parts of the swaths in the overlapping zones then fit better together after application of Ref\_Clean. It is an evidence of the good performance of the method.

It can be seen as well that the standard deviation of the second approach is smaller than for the first approach. This indicates that the second approach is more efficient than the first to reduce refraction artifacts.

#### 8.6.2. Crossing lines

In the crossing line case, we want to compare how well the nadir beams of the crossing lines fit with the rest of the survey. In order to do that, we grid the nadir beams of the crossing lines and we subtract the DTM obtained to the DTMs of the original and the processed data for the two approaches (see Figure 105).

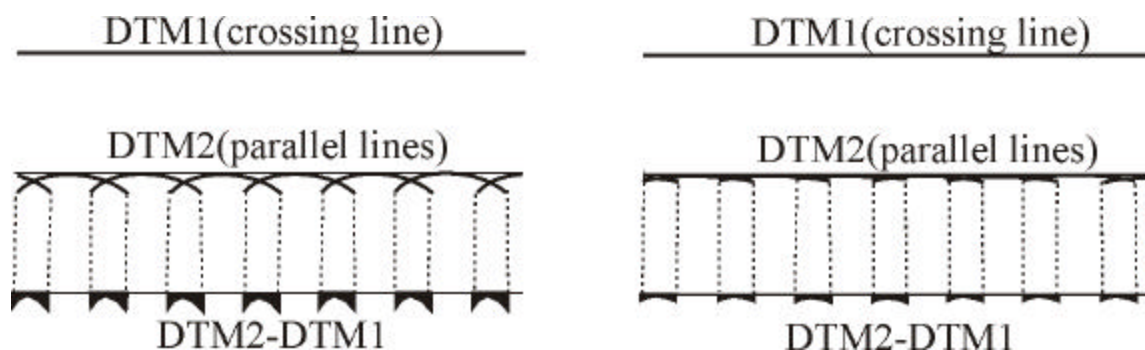


*Figure 105: Illustration of the methodology to quantify how well the crossing lines fit with the other survey lines. The DTM containing the nadir of the cross-lines is subtracted to the original data and the processed data.*

The results of the application of this methodology on the data from Saint John harbor are plotted in Figure 106. The means and standard deviations of the three difference DTMs are listed in Table 4. The results are similar to those from the case of the parallel lines, the highest standard deviation comes from the original data. The second approach seems to be giving better results than the first one. This is again an evidence of the good performance of the Ref\_Clean tool. However, it seems that there is less difference between the standard deviations of the original data and of the processed data than in the parallel line case. This would indicate that the processing of parallel lines gives better results than the processing of crossing lines.

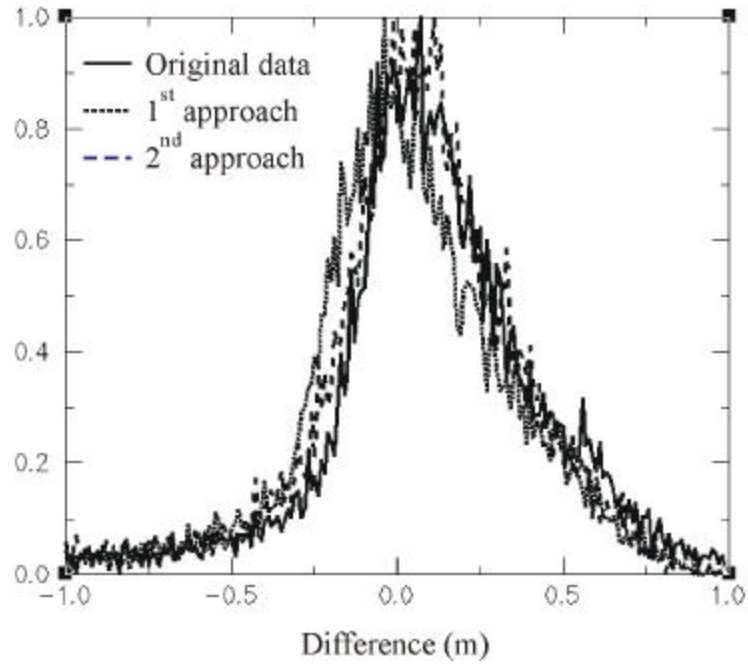


Figure 106: Normalized histograms of the difference DTMs computed to quantify the performance of the method in the parallel line case.

Table 4: List of means and standard deviations of the difference DTMs in the case of parallel lines.

	Original Data	1 <sup>st</sup> approach	2 <sup>nd</sup> approach
Mean	0.0901	0.0070	0.0397
Standard Deviation	0.3881	0.3776	0.3590

## 8.7. RECOMMENDATIONS FOR FUTURE SURVEYS

The proposed methodology is constrained by the acquired survey line geometry. In this section recommendations for future surveys that will make this method as efficient as possible are presented. Recommendations are made for parallel lines, crossing check-lines, line spacing data overlap and finally the SSP distribution.

### *8.7.1. Parallel lines*

A line can be processed only when there are two parallel lines on both sides of it. The best configuration is a continuous network of parallel lines; only the two lines on the two extremities cannot be processed.

The section of the line that is workable is the section where there is data on both sides. The optimal situation then is to have three lines of approximately the same length.

### *8.7.2. Density of check-lines*

The crossing check lines bring extra information. They are not necessary to have a full coverage of correction coefficients over the survey area. However, the generation of refraction

coefficients at a line intersection location is not affected by vertical offsets that could be present (see §7.9.1). Therefore, a regular distribution of crossing lines over the area brings extra information that is good to be taken into account with the results coming from the parallel lines analysis. A comparison of crossing lines to parallel line is a useful indicator that the method is working properly.

#### *8.7.3. Line spacing and data overlap*

Another important parameter is the distance between the parallel lines. The optimal overlap that can be achieved is 200% coverage; when the outermost beams of the current line go over the nadir beams of the previous line. The closer the lines are from each other, the closer the segment of line joining the average nadir depth of the parallel lines is from the real slope of the seafloor.

However, if the overlap becomes larger than 200%, the lines are too close to each other. In this case, the way to use Ref\_Clean consists of using the nadir data of the second parallel lines instead of the first parallel lines.

#### *8.7.4. SSP distribution*

A dense distribution of SSPs allows a better addition of the refraction artifacts in real time. If it does not reduce it enough, it gives useful information about the oceanography of the area, which helps to constrain the shape of the SSP correction that we are looking for in post processing.

## CHAPTER 9 - CONCLUSION

Refraction artifacts, like other artifacts, degrade the results of hydrographic surveys. The removal of such artifacts increases the usable information provided by the multibeam data. The objective of this research is to provide a good tool capable of reducing the impact of refraction artifacts on multibeam data.

In the first section, numerical models have been developed to study the shape of refraction artifacts generated in the water column by a sound speed discontinuity as well as by a surface sound speed inappropriately monitored at the face of the sonar transducer. The refraction artifacts caused by a surface sound speed discontinuity are analyzed for different transducer configurations (a curved array, a flat array, a roll-stabilised flat array, a dual flat array and a dual flat array roll-stabilised) as well as for single and varying roll angles. With the knowledge of the time series of the roll and the surface sound speed errors of a multibeam dataset, the numerical models can replicate the shape of the corresponding refraction artifacts and it can be subtracted from the multibeam data.

Before building the refraction tool itself, a few preliminary studies had to be carried out. The results of these preliminary studies are listed below. (a) The comparison between a synthetic SSP model with a step function and another with a linear gradient indicated that the two SSPs provide equivalent results. The step SSP is lighter computationally, it is thus adopted as the correction model. (b) It has been proved that from the four variables that define a step SSP,



only two are needed to define a unique shape of refraction artifact. (c) It has been proved that the successive application of SSPs is equivalent to the application of the sum of these SSPs and is lighter computationally.

The refraction tool Ref\_Clean uses the nadir part of the survey lines as references for a refraction-free depth. Step SSP corrections, defined by only two variables, are computed by comparing the swath of survey lines with the nadir part of the surrounding lines. Two situations are investigated. In the situation of three parallel lines, local corrections are generated at different intervals along the navigation. The swath of the middle line is compared with the nadir depth of the two parallel lines. In the situation of crossing lines, one correction is generated at each intersection. The swath of the line crossed is compared to the nadir profile of the crossing line.

These computations are realized not only on the data already processed with the measured SSPs but also with the data free of any SSP application (transit time and beam angle in an average homogeneous water column 1500 m/s).

In the absence of a better method for measuring the SSP under way, this tool provides a better imagery of the seafloor for geoscientists and cost effective means of handling non-critical survey projects (pipe-lines, cable route, fisheries habitats). Perhaps with appropriate caveats (200% coverage and a large enough number of check lines) this tool can be accepted for rigorous hydrographic surveys. It also makes the results of successive survey comparisons much more useful.

## References and Bibliography

- Albers, V.M., (1972). *Underwater Sound*. Dowden, Hutchinson & Ross, Inc.
- Bobber, R.J., (1988). *Underwater Electro-Acoustic Measurements*. Peninsula Publishing.
- Brown, J. et al (1989). *Seawater: its composition properties and behaviour*. The Open University.
- Burdic, W.S. (1991). *Underwater acoustic system analysis*. Prentice Hall Signal Processing Series.
- Cheney, W., D. Kincaid (1980). *Numerical Mathematics and Computing*. second ed., Brooks/Coles Publishing Company.
- Capell, W.J. (1999). *Determination of Sound Velocity Profile Errors Using Multibeam Data*. Proceedings of Oceans99, September 1999, Seattle, WA, US.
- Coté, P., Maurice, F., Kammerer, E., Hill, P., Locat, P., Simpkin, P., Long, B., Leroueil, S. (1999). *Intégration des methodes géotechniques et géophysiques pour le calcul du volume des sédiments de la couche de 1996 dans la baie des Ha!Ha!*. Comptes Rendus du congrès à Montréal de la Société Canadienne de Météorologie et d'Océanographie (SCMO). p.138.
- Cox, A.W. (1974). *Sonar and underwater sound*. Lexington Books.
- Davids, N., E.G. Thurston, R.E. Munser (1951). *The Design of Optimum Directionnal Acoustic Arrays*. The Journal of the Acoustical Society of America; vol. 24 n°1 pp.50-56.
- Del Grosso, V.A. (1952). *Velocity of Sound at Zero Depth*. NRL Report 4002.
- Dijkstra, S. (1999). *Software Tools Developed for Seafloor Classification*. Ph.D thesis, Department of Geodesy and Geomatics Engineering, University of New Brunswick, Fredericton, N.B., Canada.
- Dinn, D.F., B.D. Loncarevic and G. Costello (1995); *The Effect of Sound Velocity Errors On Multi-beam Sonar Depth Accuracy*; Proceedings of the IEEE Oceans'95 Conference, pp.1001-1010, IEEE, New York, Oct. 1995.

- Follet, R.F., J.P. Donohoe (1994). *A Wideband High Resolution Low Probability of Detection FFT Beamformer*. IEEE Journal of Oceanic Engineering; Vol.19 n°2 April 1994 pp.175-182.
- Geng, X., A. Zielinski (1998). *New Methods for Precise Acoustic Bathymetry*, Proceedings of the Canadian Hydrographic Conference, March 1998, Victoria, B.C., Canada, pp. 187-198.
- Geng, X., A. Zielinski (1999). *Precise Multibeam Acoustic Bathymetry*, Marine Geodesy, vol. 22, p. 157-167.
- Hammerstad, E. (1998); *Multibeam Echo Sounding for EEZ Mapping*. EEZ Technology, Second Edition, ICG Publishing Ltd. pp. 87 – 91.
- Hughes Clarke, J.E. and Godin, A., (1993). Investigation of the roll and heave errors present in Frederick G.Creed - EM1000 data when using a TSS-335B motion sensor, DFO Contract Report FP707-3-5731.
- Hughes Clarke, J. E., Mayer, L.A. and Wells, D.E., (1996a). Shallow-water imaging multibeam sonars : A new tool for investigating seafloor processes in the coastal zone and on the continental shelf : Marine Geophysical Research, v.18, p607-629.
- Hughes Clarke, J.E. (1996b). *Lecture Notes*. Multibeam Training Short Course, Ocean Mapping Group, Department of Geodesy and Geomatics Engineering University of New Brunswick.
- Hughes Clarke, J.E. (1999a). *Lecture Notes*. Coastal Multibeam Training Course, Ocean Mapping Group, Department of Geodesy and Geomatics Engineering University of New Brunswick.
- Hughes Clarke, J.E (1999b). "SwathEd". <http://www.omg.unb.ca/~jhc/SwathEd.html>
- International Hydrographic Organization (1987). Special Publication 44 (S44) 3<sup>rd</sup> edition.
- Kammerer, E., Hughes Clarke, J.E. (1998). *Monitoring temporal changes in seabed morphology and composition using multibeam sonars: a case study of the 1996 Saguenay River floods*. Proceedings of the Canadian Hydrographic Conference 1998, Victoria, B.C., Canada, pp. 450-461.
- Kinsler, L.E. (1982). *Fundamentals of Acoustics*. Third Edition, John Wiley & Sons.

- Kuwahara, S. (1939) *Velocity of Sound in Sea Water and Calculation of the Velocity for Use in Sonic Sounding*. Hydrographic Review 16, No. 2, 123.
- Leroy, C.C. (1969) *Development of Simple Equations for Accurate and More Realistic Calculation of the Speed of Sound in Sea Water*: J. Acoust. Soc. Am., 46:216.
- Locat, J., Mayer, L., Gardner, J., Lee, H., Kammerer, E., and Doucet, N., (1999). *The use of multibeam surveys for submarine landslide investigations*. Invited paper at the International Symposium on: Slope Stability Engineering: Geotechnical and Geoenvironmental Aspects, 1999, Shikoku, Japan.
- Locat, J., Kammerer, E., Doucet, N., Hughes Clarke, J., Mayer, L. et al. (1998). Comparaison des sondages multifaisceaux réalisés en 193 et 1997 dans la partie amont du fjord du Saguenay : analyse préliminaire de la couche de 1996 et d'éléments géomorphologiques. Comptes rendus du Congrès de l'Association Géologique Canadienne à Québec.
- Mackenzie, K.V. (1971). *A Decade of Experience with Velocimeters*. The Journal of the Acoustical Society of America; 13,3 pp 1321-1333.
- Mackenzie, K.V. (1981). *Nine-term Equation for Sound Speed in the Ocean*, J. Acoust. Soc. Am. 70:807.
- Medwin, H. (1975) *Speed of Sound in Water For Realistic Parameters*, J. Acoust. Soc. Am. 58:1318.
- Menke, W. (1984). *Geophysical Data analysis: Discrete Inverse Theory*; Academic Press Inc.
- de Moustier, C. (1988). *State of the art in swath bathymetry survey systems*. International Hydrographic Review, Volume 65 (2), pp 25-54.
- de Moustier, C. (1999). *Lecture Notes*. Coastal Multibeam Training Course, Ocean Mapping Group, Department of Geodesy and Geomatics Engineering University of New Brunswick.
- Okino, M.; Higashi, Y. (1986). *Measurement of seabed topography by multibeam sonar using CFFT*. IEEE Journal of Oceanic Engineering, vol. 11, no.2, pp. 474-479.
- Pickard, G.L., Emery, W.J. (1990). *Descriptive Oceanography, An Introduction*. Pergamon Press, 5<sup>th</sup> enlarged edition.

- Pohner, F., Hammerstad E. (1991). *Combining Bathymetric Mapping, Seabed Imaging*. Sea Technology, p.17.
- Simrad, (1992). *SIMRAD EM1000 Hydrographic echo sounder, Product Description*. Simrad Subsea A/S, Horten, Norway, #P2415E.
- Tolstoy, I., Clay, C.S. (1966). *Ocean Acoustics: Theory and Experiment in Under-Water Sound*. McGraw-Hill.
- Urick, R.J. (1983). *Principles of Underwater Sound for Engineers*. 3<sup>rd</sup> edition, McGraw-Hill.
- Urick, R.J. (1982) *Sound Propagation in the Sea*. Peninsula Publishing.
- Wells, D. (1999a). *Horizontal Positioning Requirements and Methods*. Coastal Multibeam Training Course, Ocean Mapping Group, Department of Geodesy and Geomatics Engineering University of New Brunswick, 32 pp.
- Wells, D. (1999b). *Vertical Positioning Requirements and Methods*. Coastal Multibeam Training Course, Ocean Mapping Group, Department of Geodesy and Geomatics Engineering University of New Brunswick, 35 pp.
- Wilson, O.B., (1988). *Introduction to Theory and Design of Sonar Transducers*; Peninsula Publishing.
- Wilson, W.D. (1960). *Speed of Sound in Sea Water as a Function of Temperature, Pressure and Salinity*. JASA 32, 641.

## **Vita**

Name: Édouard Louis Laurent Marie KAMMERER

Date/Place of Birth: 13<sup>th</sup> of April 1973  
Paris, FRANCE

Permanent Address: 13, rue de Douai  
75009 Paris  
FRANCE

University/Degree:  
1991-1995 Maîtrise de Mécanique et Calcul Scientifique  
Université Pierre et Marie Curie (Paris, France)  
1995-1996 Diplome d'Études Approfondies en Géosciences Marines  
Université de Bretagne Occidentale (Brest, France)

Publications:

- Kammerer, E., Hughes Clarke J.E. (2000) New Method for the Removal of Refraction Artifacts in Multibeam Echosounders Systems: Proceedings of the Canadian Hydrographic Conference, May 2000, Montreal, P.Q., Canada.
- Hughes Clarke J.E., Lamplugh M., Kammerer E. (2000) Integration of Near-Continuous Sound Speed Profile Information: Proceedings of the Canadian Hydrographic Conference, May 2000, Montreal, P.Q., Canada.
- Schmitt T., Locat J., Kammerer, E., Hill P., Long B., Hughes Clarke J.E., Urgeles R. (2000) Analysis of the Evolution of the Reflectivity of Sediments Settled During the 1996 Flood in the Saguenay Fjord, Using the SIMRAD EM1000 Multibeam Sonar: Proceedings of the Canadian Hydrographic Conference, May 2000, Montreal, P.Q., Canada
- Coté, P., Maurice, F., Kammerer, E., Hill, P., Locat, P., Simpkin, P., Long, B., Leroueil, S. (1999), Intégration des méthodes géotechniques et géophysiques pour le calcul du volume des sédiments de la couche de 1996 dans la baie des Ha!Ha!. Proceedings of the Canadian Meteorological and Oceanographic Society (CMOS) congress in Montreal. p.138.
- Locat, J., Mayer, L., Gardner, J., Lee, H., Kammerer, E., and Doucet, N., (1999). The use of multibeam surveys for submarine landslide investigations. Invited paper. International Symposium on: *Slope Stability Engineering: Geotechnical and Geoenvironmental Aspects*, Shikoku, p. 127-134.
- Parrot, R., Hughes Clarke, J.E., Fader, G., Shaw, J., Kammerer, E., (1999). Integration of multibeam bathymetry and sidescan sonar data for geological surveys: OCEANS 99, in press.
- Locat, J., Kammerer, E., Doucet, N., Hughes Clarke, J., Mayer, L. et al. (1998), Comparaison des sondages multifaisceaux réalisés en 193 et 1997 dans la partie amont du fjord du Saguenay: analyse préliminaire de la couche de 1996 et d'éléments géomorphologiques: Proceedings of the Canadian Geological Association Conference in Québec.
- Kammerer, E., Hughes Clarke, J. E., Locat, J., Doucet, N., Godin, A. et al. (1998), Monitoring temporal changes in seabed morphology and composition using multibeam sonars: a case study of the 1996 Saguenay River floods: Proceedings of the Canadian Hydrographic Conference in Victoria, p. 450-461.

Kammerer, E., (1996), Mise en évidence du rebond post-glaciaire en Europe du Nord à partir de données marégraphiques: DEA dissertation non published, Université de Bretagne Occidentale, Brest.